JETP Letters, Vol. 77, No. 5, 2003, pp. 201–206. From Pis'ma v Zhurnal Éksperimental'noĭ i Teoreticheskoĭ Fiziki, Vol. 77, No. 5, 2003, pp. 243–248.

Statefinder—A New Geometrical Diagnostic of Dark Energy¶

V. Sahni[1], T. D. Saini[1], A. A. Starobinsky[2], and U. Alam[1]

[1] *Inter-University Centre for Astronomy and Astrophysics, Puné 411007, India*

[2] *Landau Institute for Theoretical Physics, Russian Academy of Sciences, Moscow, 119334 Russia*

Received February 3, 2003

We introduce a new cosmological diagnostic pair $\{r, s\}$ called the Statefinder. The Statefinder is a geometrical diagnostic and allows us to characterize the properties of dark energy in a model-independent manner. The Statefinder is dimensionless and is constructed from the scale factor of the Universe and its time derivatives only. The parameter r forms the next step in the hierarchy of geometrical cosmological parameters after the Hubble parameter H and the deceleration parameter q, while a is a linear combination of q and r chosen in such a way that it does not depend upon the dark energy density. The Statefinder pair $\{r, s\}$ is algebraically related to the equation of state of dark energy and its first time derivative. The Statefinder pair is calculated for a number of existing models of dark energy having both constant and variable w. For the case of a cosmological constant, the Statefinder acquires a particularly simple form. We demonstrate that the Statefinder diagnostic can effectively differentiate between different forms of dark energy. We also show that the mean Statefinder pair can be determined to very high accuracy from a SNAP-type experiment. © *2003 MAIK "Nauka/Interperiodica".*

PACS numbers: 98.80.Es; 95.35.+d

Recent observations of type Ia supernovae indicate that the expansion of the Universe is accelerating rather than slowing down [1]. These results, when combined with cosmic microwave background (CMB) observations of a peak in the angular power spectrum on degree scales [2, 3], strongly suggest that the Universe is spatially flat with ~1/3 of the critical energy density being in nonrelativistic matter and ~2/3 in a smooth component with large negative pressure ("dark energy"). Indirect support for dark energy (known long ago) comes from the examination of gravitational clustering within the framework of the standard gravitational instability scenario (see the reviews [4, 5]). Finally, with recent data on the galaxy power spectrum from the 2dF Galaxy Survey, combined with CMB data, the existence of dark energy can be proved without using the supernovae data at all [6]. A large body of recent work has focussed on understanding the nature of dark energy and its possible relation to a fundamental theory of matter such as M-theory or supergravity. Despite the considerable effort in this direction, both the nature of dark energy as well as its cosmological origin remain enigmatic at present.

The simplest model for dark energy is a cosmological constant Λ, whose energy density remains constant with time, $\varepsilon = \Lambda/8\pi G$, and whose effective equation of state remains fixed, $w \equiv P/\varepsilon = -1$ (P is the pressure) as the Universe evolves. The cold dark matter (CDM) model with the cosmological constant having the corresponding mass density

$$\rho_\Lambda = \frac{\varepsilon_\Lambda}{c^2} = 6.44 \times 10^{-30} \left(\frac{\Omega_\Lambda}{0.7}\right)\left(\frac{h}{0.7}\right)^2 \text{ g cm}^{-3}, \quad (1)$$

where h is the Hubble constant H_0 in terms of 100 km s^{-1} Mpc^{-1} and $\Omega_\Lambda = 0.7 \pm 0.1$, $h = 0.7 \pm 0.1$, provides an excellent explanation for the acceleration of the Universe and other existing observational data. However, it remains quite possible that the dark energy density may depend sufficiently weakly upon time. This follows from many proposed models. The possibility that dark energy could be dynamical is also suggested by the remarkable *qualitative* analogy between the observed properties of dark energy and properties of a different type of "dark energy"—namely, the inflaton field—postulated in the inflationary scenario of the early Universe.

Once we allow the dark energy density to be time-dependent, then the next simplest class of models are those with a constant, nonpositive w. We shall call this class "quiessence" (Q) ($w < -1/3$ is a necessary condition to make the Universe accelerate). Examples include a tangled and "frustrated" network of cosmic strings $w = -1/3$ and domain walls $w = -2/3$. More generally, in a Friedmann–Robertson–Walker (FRW) background with the presence of CDM, an arbitrary but constant w for dark energy from the range $(-1, 0)$ can be achieved by using a scalar field with a hyperbolic sine potential (see Eq. (9) below) [4]. It may be noted that in principle the value of w may be even less than -1; the present observational data do not exclude this

¶This article was submitted by the authors in English.

Table 1

Dark Energy	State Parameter	Energy Density Parameter
Cosmological constant	$w(z) = \text{const} = -1$	$\rho(z) = \Lambda/8\pi G = \text{const}$
Quiessence	$w(z) = \text{const} < -1/3$	$\varepsilon(z) = \varepsilon_0(1+z)^{3(1+w)}$
Kinessence	$w(z) \neq \text{const}$	$\varepsilon(z) = \varepsilon_0 \exp\left(3\int_0^z dz' \frac{1+w(z')}{1+z'}\right)$

possibility but limit the constant w to a range of about (–1.6, –0.8) [7].

A more generic alternative to Λ and Q is presented by "kinessence" (K), which refers to dark energy with a *time-dependent w.* Examples of kinessence include "quintessence"—a scalar field ϕ with a self-interaction potential $V(\phi)$ minimally coupled to gravity (see [4] for numerous references), as well as the "Chaplygin gas" model [8] and braneworld models of dark energy [9, 10]. These three alternatives are summarized in the Table 1 (where $z \equiv a(t_0)/a(t) - 1$ is the redshift, $a(t)$ is a FRW scale factor, and the subscript 0 denotes the present moment).

The effective equation of state is clearly an important property of dark energy. This has led to numerous attempts to reconstruct the former from observations of high-redshift supernovae in a mode-independent manner [11–13]. However, for field-theoretical models of dark energy, the equation of state is not a *fundamental* property. Strictly speaking, it has reference only to an exactly isotropic FRW background. For small perturbations superimposed on a FRW background, the pressure tensor is generically nondiagonal (nonbarotropic), and the velocity of signal propagation need not be given by the standard hydrodynamic expression $\sqrt{dP/d\varepsilon}$. Moreover, the very notions of ε and P for dark energy presuppose the *Einstein interpretation* of gravitational field equations (not to be confused with the notion of the Einstein frame, which is used in scalar-tensor and string theories of gravity!). Namely, even if the real equations for a given model are not the 4D Einstein equations at all (examples include dark energy models in scalar-tensor [14] and brane [9, 10] gravity), one can still write them formally in the Einstein form, by placing the Einstein tensor $R_{ij} - \frac{1}{2} g_{ij} R$ on the left-hand side and by grouping all other terms on the right-hand side and calling them (after dividing by $8\pi G$) "the effective energy-momentum tensor of matter." After that, the energy-momentum tensor of dustlike matter (describing CDM and baryons) is subtracted from the latter, and the remaining part is used to define ε and P for "dark energy." All this reveals how ambiguous the notion of "equation of state" can be for a non-Einsteinian model of dark energy.

Fundamental variables (at least, at the field-theoretical level of consideration) are either geometrical (astronomical)—if they are constructed from a spacetime metric directly, or physical—those which depend upon properties of physical fields carrying dark energy. Physical variables are, of course, model-dependent, while geometrical variables are more universal. Additionally, the latter do not depend upon uncertainly measured physical quantities such as the present density of dustlike matter Ω_m. That is why we emphasize the use of geometrical variables when describing the present expansion of the Universe and properties of dark energy.

The oldest and most well-known geometric variables are the Hubble constant H_0 and the current value of the deceleration parameter q_0. At present, accurate measurements of the expansion law of the Universe during the past are also possible (e.g., using the luminosity distance to distant supernovae); therefore, these variables should be generalized to the Hubble parameter $H(t) \equiv \dot{a}/a$ and the deceleration parameter $q(t) \equiv -a\ddot{a}/\dot{a}^2 = -\ddot{a}/aH^2$ ($H_0 = H(t_0)$ and $q_0 = q(t_0)$). However, both the necessity of consideration of more general models of dark energy than a cosmological constant and the remarkable increase in the accuracy of cosmological observational data during the last few years compel us to advance beyond these two important quantities. For this reason, in this letter we propose a new geometrical diagnostic pair for dark energy. This diagnostic is constructed from the $a(t)$ and its derivatives up to the third order. Namely, we introduce the Statefinder pair $\{r, s\}$:

$$r = \frac{\dddot{a}}{a\mathrm{H}^3}, \quad s = \frac{r-1}{3(q-1/2)}, \tag{2}$$

$r(z)$ is a natural next step beyond $H(z)$ and $q(z)$. We will soon see that it has a remarkable property for the basic flat ΛCDM FRW cosmological model; $s(z)$ is a linear combination of $r(z)$ and $q(z)$. In a companion paper, we shall show that a particular combination of two variables from the above three, e.g., q and s, can provide an excellent diagnostic for describing the properties of dark energy [15].

Below, we will assume that the Universe is spatially flat, $k = 0$. This assumption naturally follows from the simplest versions of the inflationary scenario and is

convincingly confirmed by recent CMB experiments [3]. At late times ($z \lesssim 10^4$), the Universe is well described by a two-component fluid consisting of nonrelativistic matter (CDM + baryons) Ω_m and dark energy $\Omega_X = 1 - \Omega_m$. In this case, the Statefinder pair acquires the form

$$r = 1 + \frac{9}{2}\Omega_X w(1+w) - \frac{3}{2}\Omega_X \frac{\dot{w}}{H}, \quad (3)$$

$$s = 1 + w - \frac{1}{3}\frac{\dot{w}}{wH}, \quad (4)$$

where $w = P_X/\varepsilon_X$. Thus, if the role of dark energy is played by a cosmological constant ($w = -1$), then the value of r stays pegged at $r = 1$ throughout the *entire matter-dominated epoch and at all future times*; i.e., $r \equiv 1$ for $z \lesssim 10^4$ irrespective of the current value of Ω_m. The extreme simplicity of the parameter $r(z)$ for the basic cosmological model (ΛCDM), which also provides the best fit to existing observational data, may, in fact, prove not to be a mere coincidence![1] Very different behavior is predicted for quiessence and kinessence, for which r is a function of time. In particular, if dark energy is attributed to a minimally coupled scalar field ϕ (quintessence),

$$r = 1 + \frac{12\pi G\dot{\phi}^2}{H^2} + \frac{8\pi G\dot{V}}{H^3}. \quad (5)$$

The properties of the second Statefinder s complement those of the first. For the basic ΛCDM model with any nonzero Λ, $s \equiv 0$. Moreover, s depends neither on time nor on Ω_m for quiessence models, for which $s = 1 + w$. In marked contrast, s generically depends on time for kinessence. E.g., for quintessence,

$$s = \frac{2(\dot{\phi}^2 + 2\dot{V}/3H)}{\dot{\phi}^2 - 2V}. \quad (6)$$

Thus, the properties of the Statefinder pair $\{r, s\}$ enable it to differentiate between the three canonical forms of dark energy described in Table 1.

It is straightforward to invert Eqs. (3), (4) and express w and $\dot{w}$ in terms of the Statefinder pair. However, w is more directly related to the deceleration parameter:

$$w(t) = \frac{2q(t) - 1}{3\Omega_X}. \quad (7)$$

Thus, w a composite quantity, since it is constructed out of physical (Ω_X) as well as geometrical (q) parameters.

[1] Note that the quantity $r(z)$ was also considered in the paper [16] for a nonflat case when it is time-dependent. However, its remarkable property for the flat ΛCDM model was not emphasized. For completeness, let us mention that $r = 2q = \Omega_m(z)$, $s \equiv 2/3$ for a matter-dominated nonflat CDM model with negligible amounts of dark energy and radiation.

Table 2. Relationship between geometrical and physical parameters characterizing the observable Universe

Geometrical parameters	Related physical parameters
$H = \dot{a}/a$	Ω_{total}, Ω_{curv}
$q = -\ddot{a}/aH^2$	Ω_i, w_i
$r = \dddot{a}/aH^3$	Ω_i, w_i, $\dot{w}_i$
$s = (r-1)/3(q-1/2)$	w_i, $\dot{w}_i$

Note that for quintessence, $w > -1$, but $\dot{w}$ may have any sign (for models with $\dot{w} > 0$ and $w < 0$ the epoch of dark energy domination is usually a *transient*). The relationship between geometrical and physical parameters is summarized in Table 2.

Let us now study the Statefinder pair for different models of dark energy in greater detail. As was mentioned already, its value is equal to $\{1, 0\}$ for any ΛCDM model with a nonzero Λ. Quiessence models (QCDM) have a constant w; as a result,

$$r = 1 + \frac{9}{2}\Omega_Q w(1+w), \quad s = 1 + w. \quad (8)$$

Two values of the equation of state are singled out for special attention: $w = -1/3$ (cosmic strings) and $w = -2/3$ (domain walls). In both cases, the first Statefinder has the simple form $r(t) = 1 - \Omega_Q(t) = \Omega_m(t)$. As a result, $r(t) \longrightarrow 1$ for $t \ll t_0$, $r(t) \longrightarrow 0$ for $t \gg t_0$, and $r_0 \simeq 0.3$ at the present time, when $\Omega_Q(t_0) \simeq 0.7$. This leads to a degeneracy in r_0 for the dual value $w = -1/3, -2/3$. Though generic, this degeneracy is easily broken when one adds information from the second Statefinder s. Note that the case of an arbitrary $-1 < w < 0$ in the presence of a nonzero Ω_m can be achieved using quintessence with the potential [4] (see also [17])[2]

$$V(\phi) = \frac{3H_0^2(1-w)(1-\Omega_{m0})^{1/|w|}}{16\pi G\Omega_{m0}^{(1+w)/|w|}} \times \sinh^{-2(1+w)/|w|}\left(|w|\sqrt{\frac{6\pi G}{1+w}}(\phi - \phi_0 + \phi_1)\right), \quad (9)$$

$$\Omega_{m0} = \Omega_m(t_0), \quad \phi_0 = \phi(t_0),$$

$$\phi_1 = \sqrt{\frac{1+w}{6\pi G}}\frac{1}{|w|}\ln\frac{1+\sqrt{1-\Omega_{m0}}}{\sqrt{\Omega_{m0}}}.$$

In this case, $r < 1$, $0 < s < 1$.

Let us now turn to the quintessence case, where r and s are given by Eqs. (5) and (6) correspondingly. To this category belong scalar fields with "tracker" potentials, for which the scalar field ϕ approaches a common

[2] There are some misprints in the numerical coefficients in Eqs. (119)–(121) of [4], which are corrected here.

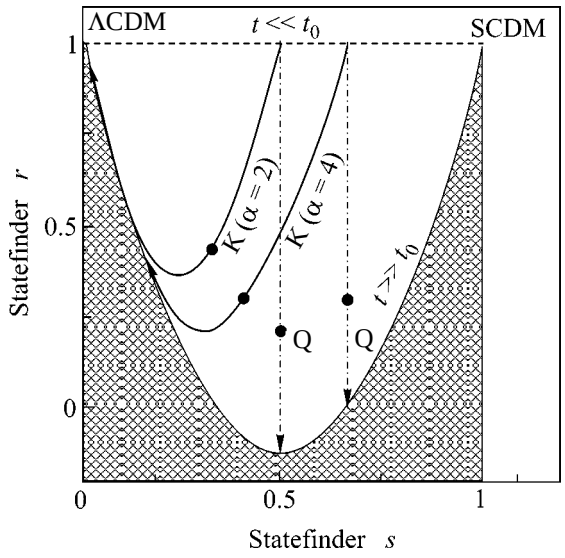

Fig. 1. The Statefinder pair (r, s) is shown for different forms of dark energy. In quiessence (Q) models (w = constant ≠ –1), the value of s remains fixed at $s = 1 + w$, while the value of r asymptotically declines to $r(t \gg t_0) \simeq 1 + \frac{9w}{2}(1 + w)$. Two models of quiessence corresponding to $w_Q = -0.25, -0.5$ are shown. Kinessence (K) models are presented by a scalar field (quintessence) rolling down the potential $V(\phi) \propto \phi^{-\alpha}$ with $\alpha = 2, 4$. These models commence their evolution on a tracker trajectory described by (10) and asymptotically approach ΛCDM at later times. ΛCDM ($r = 1$, $s = 0$) and SCDM in the absence of Λ ($r = 1$, $s = 1$) are the fixed points of the system. The hatched region is disallowed in quiessence models and in the kinessence model under consideration. The filled circles show the *current values* of the Statefinder pair (r, s) for the Q and K models ($\Omega_{m0} = 0.3$).

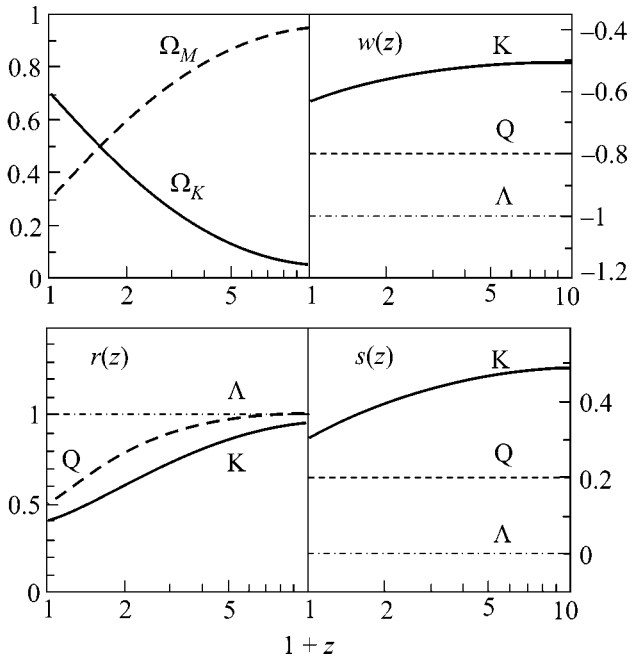

Fig. 2. The Statefinder pair {r, s} is shown for dark energy consisting of a cosmological constant Λ, quiessence Q with an nonevolving equation of state $w = -0.8$, and the inverse power law tracker model $V = V_0/\phi^2$, referred to here as kinessence "K." The lower left panel shows $r(z)$, while the lower right panel shows $s(z)$. Kinessence has a time-dependent equation of state, which is shown in the top right panel. The fractional density in matter and kinessence is shown in the top left panel.

evolutionary path from a wide range of initial conditions [18]. Tracker potentials satisfy $V''V/(V')^2 \geq 1$. We consider the simplest case of an inverse power-law potential $V(\phi) = V_0/\phi^\alpha$, $\alpha > 0$ first studied in [19]. For this potential, the region of initial conditions for ϕ for which the tracker regime has been reached before the end of the matter-dominated stage is $\phi_{\rm in} \ll M_P \equiv \sqrt{G}$, and the present value of quintessence is $\phi(t_0) \sim M_P$. The evolving values of the Statefinder pair for this potential with $\alpha = 2$ and $\alpha = 4$ are shown in Figs. 1 and 2. Also shown are results for the cosmological constant and quiessence. During tracking, $\varepsilon_\phi/\varepsilon_m \propto t^{4/(2+\alpha)}$; as a result, quintessence always becomes dominant at late times. The equation of state of quintessence and the corresponding value of the Statefinder pair is given by

$$w = -\frac{w_B + 2}{\alpha + 2}, \quad r \approx 1, \quad s \approx 1 + w \qquad (10)$$

($w_B = 1/3$, 0 during the radiation- and matter-dominated epochs, respectively).

Constraints from structure formation and the CMB suggest that dark energy must be subdominant at $z \gtrsim 1$. Primordial nucleosynthesis arguments impose the stringent constraint $\Omega_X < 0.05$ at $z \sim 10^9$ [20]. Small values of Ω_X and w substantially decrease the terms $\Omega_X w$ and $\Omega_X \dot{w}/H$ that appear on the right-hand side of (3) and ensure that the Statefinder r remains close to unity at high z. This is exactly what one finds from Fig. 2. The extreme sensitivity of r to an evolving equation of state of the tracker field is reflected by the fact that the value of r declines rapidly as the Universe expands, dropping to ~50% from its starting value by $z \sim 1$, even though dark energy remains subdominant at this epoch.

As is apparent from Fig. 2, the discriminating power of r and s can be significant even at moderate redshifts. Since Ω_Λ and Ω_Q usually decrease faster with redshift than Ω_K, the value of $r(z)$ for both the cosmological constant and quiessence is generally closer to unity at a given large redshift than the corresponding value for a tracker field (kinessence). Thus, whereas the current value of r_0 allows us to differentiate Λ from Q and K, the value of r at moderate redshifts distinguishes K from Λ and Q. This feature is even more pronounced in the second Statefinder s, whose value does not explicitly depend upon Ω_X and whose capacity to distinguish

between Λ and quiessence on the one hand and kinessence on the other actually *increases* with redshift (see Fig. 2). The present CMB, SNe, and galaxy clustering data strongly suggest that $\alpha \lesssim 1$ for quintessence with the inverse power-law potential [7]. However, even then the Statefinder remains a useful diagnostic, as will be shown below.

Let us consider another form of kinessence. Below, we determine the value of the Statefinder pair for the simplest of brane cosmological models—the Dvali–Gabadadze–Porrati (DGP) model [9]. It is important to note that in this model "dark energy" is not the energy associated with a new form of matter; rather, its origin is geometrical in nature and is entirely due to the fact that general relativity is formulated in 5-dimensional space-time. The model has only one adjustable parameter r_c—the scale beyond which gravity becomes five-dimensional. This scale can be related to the current values of H_0 and Ω_{m0} by the relation $H_0 r_c = 1/(1 - \Omega_{m0})$. The FRW equation for this model reads

$$H = \sqrt{\frac{8\pi G\varepsilon_m}{3} + \frac{1}{4r_c^2}} + \frac{1}{2r_c} \tag{11}$$

(the choice of sign in front of the last term on the right-hand side corresponds to the "Brane2" class of models, according to the terminology of [10]).

The solution to (11) can be written in the following parametric form:

$$a = a_1 \sinh^{2/3}\psi, \quad \frac{3t}{2r_c} = \psi + \frac{1 - e^{-2\psi}}{2},$$
$$H = \frac{e^{\psi}}{2r_c \sinh\psi}, \quad \varepsilon_m = \frac{3}{32\pi G r_c^2 \sinh^2\psi}, \tag{12}$$
$$\Omega_m \equiv \frac{8\pi G\varepsilon_m}{3H^2} = e^{-2\psi}.$$

The values of the deceleration parameter and the Statefinder pair read

$$q = \frac{2\Omega_m - 1}{1 + \Omega_m}, \quad r = 1 - \frac{9\Omega_m^2(1 - \Omega_m)}{(1 + \Omega_m)^3},$$
$$s = \frac{2\Omega_m^2}{(1 + \Omega_m)^2}. \tag{13}$$

In particular, $r = 0.74$, $s = 0.11$ for $\Omega_m = 0.3$. At large redshifts, the Universe becomes matter-dominated and $r \longrightarrow 1$, $s \longrightarrow 0.5$.

At the end of the paper, we estimate the accuracy with which the Statefinder pair (averaged over a range of z) can be determined in future SNAP-type satellite missions. The "SuperNovae Acceleration Probe" (SNAP) is expected to observe approximately 2000 type Ia supernovae within a year up to a redshift $z \sim 2$ and to improve luminosity distance statistics by over an order of magnitude [21]. Measurement of the luminosity distance $D_L(z)$ allows us to determine the Hubble parameter, since [11, 4]

$$H(z) = \left[\frac{d}{dz}\left(\frac{D_L(z)}{1 + z}\right)\right]^{-1}. \tag{14}$$

To determine the Statefinder pair, we use the following model-independent parameterization of $H(z)$:

$$H^2(x) = H_0^2[\tilde{\Omega}_{m0}x^3 + A + Bx + Cx^2], \tag{15}$$

where $x = 1 + z$ and $A + B + C = 1 - \tilde{\Omega}_{m0}$. This form is simpler than that used in [12], but it is sufficient for our purposes. It becomes exact in the case of the ΛCDM model (i.e., dark energy being a cosmological constant). Note that the fact that we parameterize $H^2(z)/H_0^2$ by a 3-parameter fit means that the real $H(z)$ curve is *smoothed* over some redshift interval $z \sim z_{\max}/3$. In principle, the value of $\tilde{\Omega}_{m0}$ can be somewhat larger than the current density in CDM + baryons if dark energy has a tracker component having equation of state equal to that of matter at high z. However, the difference between Ω_{m0} and $\tilde{\Omega}_{m0}$ (if it exists at all) is known to be small: $\tilde{\Omega}_{m0} \lesssim 1.1\Omega_{m0}$. Supernovae observations of D_L and relations (14) and (15) can be used to determine A, B, C, and the Statefinder pair $\{r, s\}$, since

$$r = 1 - \frac{(B + Cx)x}{\tilde{\Omega}_{m0}x^3 + A + Bx + Cx^2},$$
$$s = \frac{2(B + Cx)x}{3(3A + 2Bx + Cx^2)}. \tag{16}$$

In Fig. 3, we present the results obtained from 1000 random simulations of a SNAP-type experiment for the "mean Statefinder statistic"

$$\bar{r} = \frac{1}{z_{\max}}\int_0^{z_{\max}} r(z)dz, \tag{17}$$

$$\bar{s} = \frac{1}{z_{\max}}\int_0^{z_{\max}} s(z)dz, \tag{18}$$

with $z_{\max} = 1.7$. The simulated numbers of SNe Ia events for a one-year period of observations are taken to be 50, 1800, 50, and 15 for the redshift intervals (0–0.2), (0.2–1.2), (1.2–1.4), and (1.4–1.7), respectively. The statistical uncertainty in the magnitude of SNe is assumed to be constant over redshift and is given by $\sigma_{\text{mag}} = 0.15$. Details will be presented in a companion paper [15]. Figure 3 shows that a future SNAP-type experiment determining $\{r, s\}$ can easily distinguish a fiducial ΛCDM model from several alternative time-dependent forms of dark energy, including the inverse

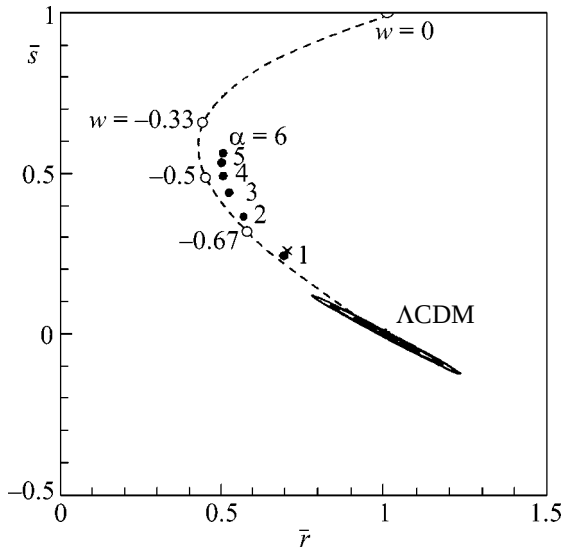

Fig. 3. Confidence levels at 1σ, 2σ, 3σ of $\bar{r}$ and $\bar{s}$ computed from 1000 random realizations of a SNAP-type experiment probing a ΛCDM fiducial model with $\Omega_{m0} = 0.3$, $\Omega_{\Lambda 0} = 0.7$. The dark circles represent the values of $\bar{r}$ and $\bar{s}$ for the quintessence potential $V(\phi) \propto \phi^{-\alpha}$ with $\alpha = 1$, 2, 3, 4, 5, 6 (bottom to top). The open circles represent quiessence with $w = -2/3, -1/2, -1/3, 0$ (bottom to top). The cross shows the mean Statefinder value $\bar{r} = 0.70$, $\bar{s} = 0.27$ for the DGP brane model with $H_0 r_c = 1.43$ ($\Omega_{m0} = 0.3$). Note that all inverse power-law models, as well as the DGP model, lie well outside of the three-sigma contour centered around the ΛCDM model.

power-law quintessence potential $V(\phi) \propto \phi^{-\alpha}$ with $\alpha \sim 1$ and the DGP brane cosmological model.

VS acknowledges support from the ILTP program of cooperation between India and Russia. TDS and UA thank the UGC for providing support for this work. AS was partially supported by the Russian Foundation for Basic Research, grant nos. 02-02-16817 and 00-15-96699, and by the Research Program "Astronomy" of the Russian Academy of Sciences.

REFERENCES

1. S. J. Perlmutter, G. Aldering, G. Goldhaber, *et al.*, Astrophys. J. **517**, 565 (1999); A. Riess, A. V. Filippenko, P. Challis, *et al.*, Astron. J. **116**, 1009 (1998).
2. P. de Bernardis, P. A. R. Ade, J. J. Bock, *et al.*, Nature **404**, 955 (2000); A. E. Lange, P. A. R. Ade, J. J. Bock, *et al.*, Phys. Rev. D **63**, 042001 (2001); A. Balbi, P. A. R. Ade, J. J. Bock, *et al.*, Astrophys. J. **545**, L1 (2000).
3. A. Benoit, P. Ade, A. Amblard, *et al.*, Astron. Astrophys. **399**, L25 (2003); astro-ph/0210306 (2002).
4. V. Sahni and A. A. Starobinsky, Int. J. Mod. Phys. D **9**, 373 (2000); astro-ph/9904398 (1999); V. Sahni, Class. Quantum Grav. **19**, 3435 (2002).
5. J. A. Peacock, S. Cole, P. Norberg, *et al.*, Nature **410**, 169 (2001); P. J. E. Peebles and B. Ratra, astro-ph/0207347 (2002).
6. W. J. Percival, W. Sutherland, J. A. Peacock, *et al.*, astro-ph/0206256 (2002).
7. R. Bean and A. Melchiorri, Phys. Rev. D **65**, 041302 (2002); A. Melchiorri, L. Mersini, C. J. Odman, and M. Trodden, astro-ph/0211522 (2002); D. Pogosyan, J. R. Bond, and C. R. Contaldi, astro-ph/0301310 (2003).
8. A. Kamenshchik, U. Moschella, and V. Pasquier, Phys. Lett. B **511**, 265 (2001).
9. G. Dvali, G. Gabadadze, and M. Porrati, Phys. Lett. B **485**, 208 (2000); C. Deffayet, G. Dvali, and G. Gabadadze, Phys. Rev. D **65**, 044023 (2002).
10. V. Sahni and Yu. V. Shtanov, astro-ph/0202346 (2002); U. Alam and V. Sahni, astro-ph/0209443 (2002).
11. A. A. Starobinsky, Pis'ma Zh. Éksp. Teor. Fiz. **68**, 721 (1998) [JETP Lett. **68**, 757 (1998)]; D. Huterer and M. S. Turner, Phys. Rev. D **60**, 081301 (1999); T. Nakamura and T. Chiba, Mon. Not. R. Astron. Soc. **306**, 696 (1999).
12. T. D. Saini, S. Raychaudhury, V. Sahni, and A. A. Starobinsky, Phys. Rev. Lett. **85**, 1162 (2000).
13. T. Chiba and T. Nakamura, Phys. Rev. D **62**, 121301 (2000); I. Maor, R. Brustein, and P. J. Steinhardt, Phys. Rev. Lett. **86**, 6 (2001); J. Weller and A. Albrecht, Phys. Rev. Lett. **86**, 1939 (2001); J. Wang and P. M. Garnavich, Astrophys. J. **552**, 445 (2001); J. Weller and A. Albrecht, Phys. Rev. D **65**, 103512 (2002); M. Tegmark, Phys. Rev. D **66**, 103507 (2002); B. F. Gerke and G. Efstathiou, Mon. Not. R. Astron. Soc. **335**, 33 (2002); P. S. Corasaniti and E. J. Copeland, astro-ph/0205544 (2002); E. V. Linder, astro-ph/0208512 (2002).
14. B. Boisseau, G. Esposito-Farese, D. Polarski, and A. A. Starobinsky, Phys. Rev. Lett. **85**, 2236 (2000).
15. U. Alam, T. D. Saini, V. Sahni, and A. A. Starobinsky, astro-ph/0303009 (2003).
16. T. Chiba and N. Nakamura, Prog. Theor. Phys. **100**, 1077 (1998).
17. L. A. Urena-Lopez and T. Matos, Phys. Rev. D **62**, 081302 (2000); astro-ph/0003364 (2000).
18. I. Zlatev, L. Wang, and P. J. Steinhardt, Phys. Rev. Lett. **82**, 896 (1999); P. J. Steinhardt, L. Wang, and I. Zlatev, Phys. Rev. D **59**, 123504 (1999).
19. B. Ratra and P. J. E. Peebles, Phys. Rev. D **37**, 3406 (1988).
20. R. Bean and A. Melchiorri, Phys. Rev. D **64**, 103508 (2001).
21. G. Aldering and the SNAP collaboration, astro-ph/0209550 (2002).

JETP Letters, Vol. 77, No. 5, 2003, pp. 207–211. Translated from Pis'ma v Zhurnal Éksperimental'noĭ i Teoreticheskoĭ Fiziki, Vol. 77, No. 5, 2003, pp. 249–253.

Neutron Lifetime and the Background Structure in a Neutron Magnetic Trap

V. V. Vasil'ev

Institute of Theoretical and Experimental Physics, ul. Bol'shaya Cheremushkinskaya 25, Moscow, 117218 Russia
e-mail: basil_v@vitep1.itep.ru

Received November 24, 2002; in final form, February 6, 2003

A new cycle of processing the 1985–1986 experimental data concerning the storage of neutrons in a magnetic gravitational trap was carried out. It was shown that the count rates determined for the background are multiples of the neutron decay constant. This is explained by the fact that the background in the experiment on the storage of ultracold neutrons was caused by the electron count from background neutrons penetrating through trap walls. Numerous measurements for a small and varying number of background neutrons in the trap make it possible to extract and use data for determining the mean neutron lifetime. This lifetime turns out to be $\tau_n = 900.01 \pm 0.15$ s in a nonuniform magnetic field. © *2003 MAIK "Nauka/Interperiodica"*.

PACS numbers: 14.20.Dh

1. INTRODUCTION

In order to demonstrate the possibility of long-term storage of neutrons in a nonuniform magnetic field, experiments on the magnetic storage of ultracold neutrons (UCNs) were carried out at ITEP in 1981–1986. It was demonstrated that there is such a "long-lived" component of neutrons in a trap whose storage time exceeds 700 s [1–3]. Since the verification of the unitarity condition by means of neutron parameters is of current interest [4] and new experiments are in preparation, the whole set of data presented in [2] was recently processed once again in order to exactly separate the background contribution to the UCN count and to determine more precisely the neutrons storage time. It turned out that background data are of their own importance, which was most pronounced in the last measurement run, where "short-lived" neutrons, whose storage time was in the range 200–300 s depending on the storage conditions, were specially suppressed [1, 3]. To give the complete representation, the scheme of the experiment on the storage of UCNs in a magnetic gravitational trap, method of their injection and removal, and UCN detector will be described below. The results concerning the storage of UCNs and storage curve are not considered in this work. Basic attention is focused on the storage of neutrons in a trap, when a neutron detector records the background and neutrons that do not satisfy the storage conditions and leak from the trap to the detector. A more careful analysis of the data revealed a certain background structure, which was such that certain background count rates seemed most probable. The background that was recorded by a neutron detector was attributed to the count of electrons from the decay of neutrons penetrating through the walls and cap of the magnetic trap. When the detector is almost equivalently applicable for the detection of both UCNs and electrons from the decay of neutrons, background neutrons, more exactly electrons from their decay, make the determining contribution in the long storage interval. As will be shown below, available data for the determination of the count rate are sufficient for determining the neutron lifetime in a nonuniform magnetic field.

2. EXPERIMENTAL SETUP

Figure 1 shows the layout of the experimental setup for the magnetic storage of UCNs that was used at ITEP until 1987. Only the storage interval of neutrons in the total measurement cycle "filling–storage–discharge to the detector" is primarily important for estimating the results under consideration. After filling the trap with UCNs, the total current is turned on in the magnetic valve and confines UCNs in the storage region. Simultaneously with the closing of the valve, the tube of the injection–removal device is turned to the removal position, i.e., joins the trap chamber with the detector. The device remains in this position until the opening of the valve and then until the finish of the leakage of neutrons to the detector. This procedure ensures both the detection of neutrons that do not correspond to the storage conditions and the measurement of the background.

A UCN detector designed by A.V. Strelkov (Laboratory of Neutron Physics, JINR) is a proportional double-wire gas counter that is filled with an Ar–CO_2–^{3}He mixture at a pressure of 1.02 atm and has an Al window with a thickness of 10^{-4} m. The entrance-window diameter 9.5×10^{-2} m of the counter corresponds to the diameter of the electropolished copper tube of a turning neutron guide. The thickness and material of the foil

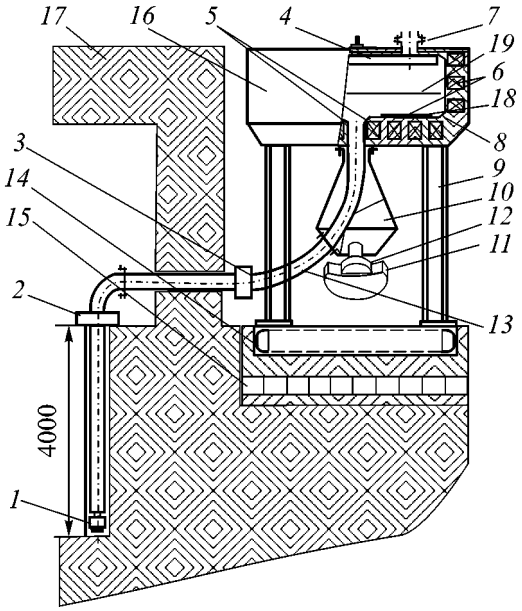

Fig. 1. Layout of the ITEP setup for the removal of neutrons from a reactor and their storage: (*1*) converter block, (*2*) upper chamber, (*3*) UCN gate, (*4*) correcting winding, (*5*) magnetic valve, (*6*) basic-magnet winding, (*7*) pumping tube, (*8*) vacuum chamber, (*9*) accumulator support, (*10*) injection–removal device for neutrons, (*11*) detector protection, (*12*) UCN detector, (*13*) neutron guide tube, (*14*) concrete fundament block, (*15*) iron–lead protection, (*16*) magnetic accumulator, (*17*) reactor protection, (*18*) polyethylene layer, and (*19*) additional absorber. The position of the injection of neutrons is shown. In the confinement position, the neutron guide inside device *10* joins the trap neck with the socket of detector *12*.

were chosen so as to detect UCNs that flow from the open magnetic valve and are accelerated in the gravitational field up to a velocity necessary for penetrating through the foil barrier (v_{gr} = 3.2 m/s for Al). As will be shown below, the detector is universal: it is applicable for detection both UCNs and electrons with energies above 150 keV [5].

A magnetic field on the valve axis was equal to 3.2 and 2.5 kG at the maximum point and at the bottom of the vacuum chamber, respectively. The magnetic guide of the trap was made of Steel 3. The radial width of poles and windings was equal to 6×10^{-2} m and the diameter of the central winding (magnetic valve) was equal to 1.2×10^{-1} m. The drop in the field from the bottom along the vertical and from the wall along horizontal is approximated by an exponential [6].

Special attention in the experiment was focused on the protection of the detector and the injection device. The magnet case, its walls, and the cap of the vacuum chamber were not additionally protected by neutron-moderating and neutron-absorbing materials. More than 1500 filling–storage–discharge measurement cycles were analyzed. The readout interval Δt in the storage mode ranged from 2 to 22 s and was equal to 5 s in some runs. The cycles were realized with various readout intervals in the two different magnetic modes and provided 324 weighted-mean values of the count rate (variant 1). Among these 324 values, 159 values were obtained when the UCN absorber was placed at half the height of the trap (Fig. 1), the current in the lower winding of the wall was equal to 300 A, and two upper windings were turned off (variant 2). The remaining values were obtained without the absorber at a current of 200 A in each of three windings of the wall. The count rates were determined with data reduced to intervals 7, 8, 10, 12, 15, and 22 s; i.e., the set of values was a mix of six independent groups. Each group of data was measured in one to two weeks. Thus, the neutron background (thermal and fast neutrons) in the experiment could vary depending on the reactor mode, surrounding experiments, and protection conditions. As was mentioned above, the integral background ranged from 6×10^{-3} to 10^{-2} s^{-1} for different runs. No attempts to improve the protection of the detector reduced the background below the achieved level.

This work was initiated by my hypothesis that the background described above is attributed to the detection of electrons from the decay of background neutrons penetrating through the cap and walls of the electromagnet and chamber. It turns out that this hypothesis is corroborated by the experimental data.

3. DATA PROCESSING METHOD AND THE DETERMINATION OF THE NEUTRON LIFETIME

The time differentiation of the radioactive-decay law $N = N_0\exp(-t/\tau)$, where N is the number of neutrons in a certain volume at time t and τ is the neutron lifetime, provides the rate G of the production of electrons and protons in this volume:

$$G = dN/dt = \lambda N, \quad (1)$$

where $\lambda = 1/\tau$ is the decay constant. Formula (1) is the decay law in the form convenient for the case of the neutron flux through the volume under consideration. If the change in the neutron flux is stepwise, N_1, N_2, …, N_k, we have $G_1 = \lambda N_1$, $G_2 = \lambda N_2$, …, $G_k = \lambda N_k$; i.e., the change in the count rate is also stepwise. Let us assume that the neutron decay region is monitored by a detector of decay electrons; i.e., electrons from this region arrive at the detector and are recorded with the integral efficiency ε, which is naturally considered as time constant. Multiplying Eq. (1) by ε, we obtain $d(\varepsilon N)/dt = \lambda(\varepsilon N)$ or the electron-detection rate

$$g = dn/dt = \lambda n, \quad (2)$$

where $n = \varepsilon N$. Therefore, the efficiency is the similarity factor transforming Eq. (1) into Eq. (2). Thus, the detector records electrons from the decay of neutrons with the count rate that is proportional to the number of neutrons whose decay is fixed by the detector, and the

proportionality factor is equal to the neutron decay constant. If the detector fixes the decay of one, two, three, etc., neutrons, the count rate of the detector obviously changes stepwise with the step λ. In this case, it is convenient to represent information in the form of the frequency histogram, which is the number of events at each interval (Fig. 2). If the detector records electrons from a variable number of neutrons, the result is the set of the count-rate values $g_k = \lambda n_k$. Multiplying this relationship by τ, we obtain

$$\tau g_k = n_k. \quad (3)$$

This relationship means that the count-rate scale is determined by the neutron lifetime; i.e., if τ is equal to the real neutron lifetime, the tops of the peaks in the frequency diagram of the count rate coincide with the scale divisions. The scale of the count rates g_k will consist of values approximately equal to 0.0011, 0.0022, 0.0033, etc., and the corresponding numbers of neutrons are equal to 1, 2, 3, etc., because $\tau \approx 900$. If an erroneous value is used for the lifetime, the scale divisions are shifted from the physically determined positions of the peaks in the count-rate diagram. Thus, distances between peaks depend on the numbers of neutrons corresponding to respective measurements and on the neutron decay constant. The numbers of neutrons determining the detector count rate can be estimated from this relationship. This estimate is obtained by multiplying the count rates by the assumed neutron lifetime, rounding the resulting numbers to an integer (for variant 2) or to chosen rounding step (0.17 or 0.1 for variant 1 depending on the depth of averaging of the primary measurements), i.e., by finding n_k. Moreover, one can also verify whether the neutron lifetime value used in this case and set of n_k values agree with experimental data. To do this, one must calculate the functional

$$F(\lambda) = \sum_{k=1}^{k=K} \frac{(g_k - n_k\lambda)^2}{\sigma_k^2}, \quad (4)$$

where σ_k is the error of g_k measurement. If the lifetime value is chosen correctly in the count rate scale, i.e., if λ_0 value corresponds to the neutron lifetime, $F(\lambda)$ has a minimum at the point $\lambda = \lambda_0$. Otherwise, $F(\lambda)$ is larger than $F(\lambda_0)$; i.e., the real lifetime value corresponds to the count-rate scale such that the scale divisions maximally approach the physical maxima of the count rate histogram. All other values provide worse agreement according to the above LSM estimate. The λ_0 value and its error can be determined from the condition of the minimum of this functional $dF(\lambda)/d\lambda = 0$. This method of the scale fitting can be verified using the data of the ITEP-1986 experiment. The vacuum chamber of the magnetic trap is obviously a region that is monitored by the detector. Background neutrons penetrating through the magnetized walls of the trap are polarized and decay in the chamber with the corresponding decay constant. This decay is in particular accompanied by the production of electrons. Serving for the storage of neutrons, the nonuniform magnetic field of the bottom and walls of the trap reflects electrons and collects them in the central part of the trap on the sink orifice (see Fig. 1). The magnetic valve orients the electron momentum along the axis of the neutron guide leading electrons to the detector. At a low value of the lower threshold, the UCN detector serves also as a detector of electrons.

4. RESULTS OF DATA PROCESSING AND DISCUSSION

Figure 2 shows the frequency histogram of the count rates, and Figure 3 shows about 300 count rates with

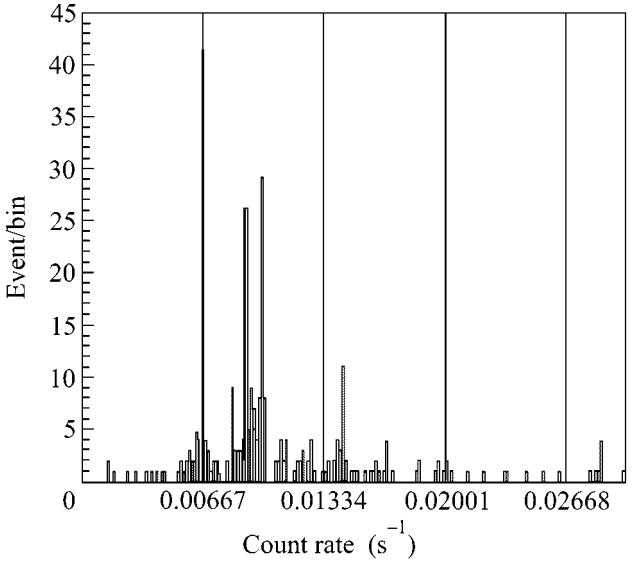

Fig. 2. Frequency histogram of the count rates obtained in the experiment. The scale corresponds to $\tau = 900$ s.

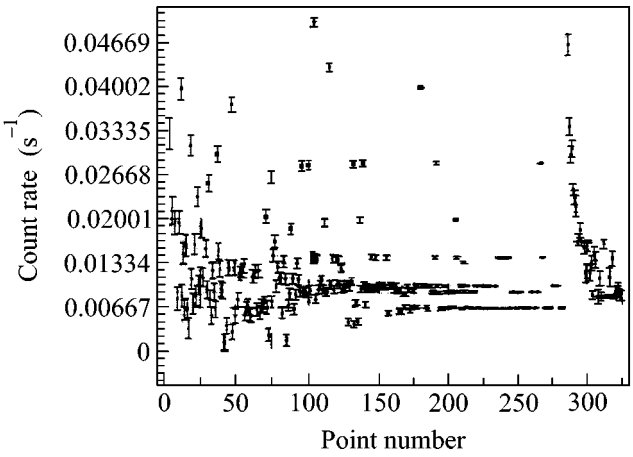

Fig. 3. Detector count rates at UCN confinement and leakage.

Probable values of the neutron lifetime

No.	Lifetime, s	Error, s	No.	Lifetime, s	Error, s	No.	Lifetime, s	Error, s
	Left wing			Average value			Right wing	
1	886.95	0.15	3	900.01	0.15	4	911.08	0.155
2	888.87	0.15				5	913.01	0.155

errors. Errors were calculated by the weighted-mean method [7] in the total number of runs, where this count rate was obtained. The entire set of count rates (in variant 1) is analyzed by the above method for the lifetime τ ranging from 884 to 916 s, which corresponds to the neutron lifetime values obtained in previous experiments. Figure 4 shows the dependence of functional (4) on the probe neutron lifetime τ determined by this method. It turns out that functional (4) has seven local minima rather than one minimum in this region. The five most reliable values are given in the table.

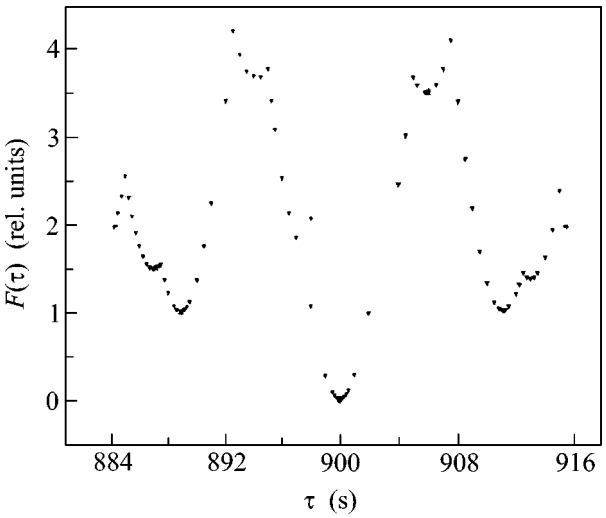

Fig. 4. Least squares method functional for the resulting set of count rates.

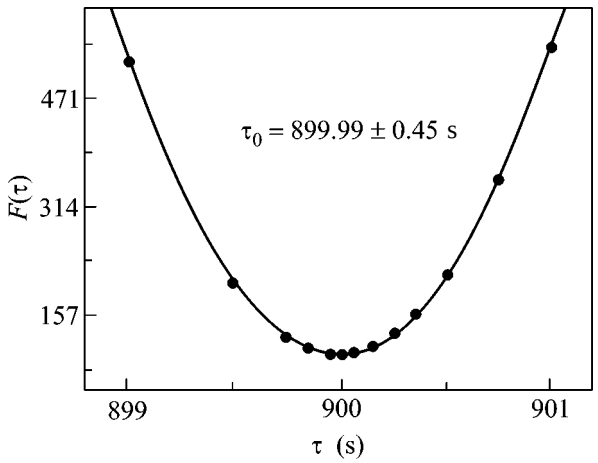

Fig. 5. Determination of the lifetime from the LSM functional for variant 2 (159 measurements of the count rate).

Results according to variant 2 provide one value $\tau_0 = 899.99 \pm 0.45$ s (see Fig. 5). Value no. 3 from the table seems to be the most reliable value. The two "left" values give 888 s in average (to the left from 900 s in the curve), and the two "right" values correspond to a mean of 912 s. These values coincide with the known results of previous measurements of the neutron lifetime with a magnetic field [8]. This result seems to be a consequence of the possible splitting of the neutron lifetime in the magnetic field, when decay electrons are detected. However, the origin of this splitting requires additional investigations, because it can be a technical sequence of the method. The most probable average value of 900.01 ± 0.15 s is determined in the framework of the method of decay scale fitting under consideration. This value is obtained by processing the entire set of measurements of the count rate (variant 1, 324 points).

5. CONCLUSIONS

It was shown that electrons from the decay of polarized neutrons from the external background inside the trap make the basic contribution to the background in the experiment with the magnetic trap. The method of the decay-scale fitting was proposed and applied to the data. Some data correspond to the lifetimes ≈888.0 and 912.0 s, which are shorter and longer than the average neutron lifetime in the nonuniform magnetic field. This fact indicates splitting of the neutron lifetime in the decay of polarized neutrons in the magnetic field. A value of 888 s is very close to the results of the most precise recent experiments [8] based on the storage of UCNs in material vessels, and a value of 912 s corresponds to experiments reported in [9]. However, this indication needs additional verification.

It was shown that the average neutron lifetime in the nonuniform magnetic field is equal to 900.01 ± 0.15 s. This result possibly provides an additional stimulus for the more precise determination of the neutron lifetime by the methods of both the storage of neutrons and detection of the products from neutron decay.

This work is based on the results obtained at the storage of UCNs in 1985 and 1986 at the ITEP reactor. I am deeply grateful to Yu.G. Abov, who drew me into work on the magnetic storage of UCNs, to V.V. Vladimirskiĭ, who initiated this work, and to I.L. Karpikhin for support at the stage of data processing. The processing stage was supported by INTAS, grant no. 00-00043.

REFERENCES

1. Yu. G. Abov, S. P. Borovlev, V. V. Vasil'ev, *et al.*, Yad. Fiz. **38**, 122 (1983) [Sov. J. Nucl. Phys. **38**, 70 (1983)].
2. Yu. G. Abov, V. V. Vasil'ev, V. V. Vladimirskiĭ, and I. B. Rozhnin, Pis'ma Zh. Éksp. Teor. Fiz. **44**, 369 (1986) [JETP Lett. **44**, 472 (1986)].
3. Yu. G. Abov, V. V. Vasil'ev, and O. V. Shvedov, Yad. Fiz. **63**, 1381 (2000) [Phys. At. Nucl. **63**, 1305 (2000)].
4. H. Abele and M. Kreuz, in *Proceedings of the ILL Millenium Symposium and European User Meeting* (2001), p. 217.
5. A. P. Babichev, I. A. Babushkina, A. M. Bratkovskaya, *et al.*, in *Physical Quantities. Handbook*, Ed. by I. S. Grigor'ev and E. Z. Mikhaĭlov (Énergoatomizdat, Moscow, 1991), p. 1169.
6. V. V. Vasil'ev, Preprint No. 39, ITÉF (Inst. of Theoretical and Experimental Physics, Moscow, 1977).
7. D. Hudson, *Statistics. Lectures on Elementary Statistics and Probability* (Geneva, 1964; Mir, Moscow, 1970).
8. Yu. V. Gaponov and Yu. A. Mostovoĭ, Yad. Fiz. **63**, 1432 (2000) [Phys. At. Nucl. **63**, 1356 (2000)].
9. C. J. Christensen, A. Nielsen, A. Bahnsen, *et al.*, Phys. Rev. D **5**, 1628 (1972).

Translated by R. Tyapaev

JETP Letters, Vol. 77, No. 5, 2003, pp. 212–216. Translated from Pis'ma v Zhurnal Éksperimental'noĭ i Teoreticheskoĭ Fiziki, Vol. 77, No. 5, 2003, pp. 254–259.

Attosecond Burst and High-Harmonic Generation in Molecular Ionization by Ultrashort Laser Pulses

M. Yu. Emelin[1], M. Yu. Ryabikin[1,] *, A. M. Sergeev[1], M. D. Chernobrovtseva[1], T. Pfeifer[2], D. Walter[2], and G. Gerber[2]

[1] *Institute of Applied Physics, Russian Academy of Sciences, ul. Ul'yanova 46, Nizhni Novgorod, 603950 Russia*

* *e-mail: mike@ufp.appl.sci-nnov.ru*

[2] *University of Würzburg, Würzburg, Germany*

Received December 5, 2002; in final form, January 14, 2003

It is shown that the efficiency of attosecond pulse and high-harmonic generation in the ionization of excited molecular structures by a powerful femtosecond optical pulse can appreciably exceed the efficiency of analogous processes in atomic systems. This is due to the presence of a delocalized electron wave-packet component in the nonequilibrium molecular states, resulting in an increase of the number of particles that are effectively involved in the bremsstrahlung generation in the course of recollisions of laser-accelerated electrons with molecular core. Calculations suggest that, by optimizing the nonlinear response of molecular systems in the ionization process, one can develop compact sources of coherent vacuum ultraviolet and X-ray radiation with luminance at a level that is presently achieved only at large-scale accelerator facilities with free-electron lasers.

PACS numbers: 42.65.Ky

High-harmonic generation in the course of atomic ionization by powerful femtosecond laser pulses is of great interest for developing compact sources of coherent vacuum-ultraviolet (VUV) and X-ray radiation. Recent experimental efforts in this field [1–3] have been devoted to the optimization of interaction conditions between femtosecond radiation and rarefied inert gases to demonstrate the possibility of fabricating "desktop" VUV sources with pulse luminance only one or two orders of magnitude inferior to the best world achievements obtained at large-scale accelerator facilities with free-electron lasers [4, 5]. Further progress in enhancing the efficiency of high-harmonic generation might be associated with the conversion of optical radiant energy into the short-wavelength radiation using molecules or clusters as particles with nonlinear response potentially stronger than in atoms. In this work, high-harmonic generation and attosecond radiation bursts in the course of ionization of the simplest molecular structures by an ultrashort laser pulse were studied to demonstrate that the nonlinear response in the VUV and soft X-ray regions can be optimized at a level that sizably exceeds the analogous atomic response.

Compared to atoms, molecules and clusters possess a diversity of sizes, shapes, orientations about the exciting laser field, i.e., new factors that can be used to optimize the nonlinear response. In recent theoretical studies, some advantages of molecular systems were formulated. Among them are the extension of short-wavelength plateau in the spectra of harmonic generation owing to the collision of a laser-accelerated electron with a "foreign" ion in the molecule [6–9]; the excitation of even harmonics with an amplitude comparable to the amplitude of traditional odd harmonics in the ionization of heteroatomic molecules [10]; and the increase in harmonic generation efficiency in an exciting field oriented transverse to the molecular axis [11]. However, regimes with a noticeable increase in the generation efficiency, as compared to inert gases, have not been observed so far in experiments with molecular gases [12–15]. As shown in this work, a plausible explanation is that the regime of optimal nonlinear response corresponds to the essentially nonequilibrium nuclear positions in a molecule, for which the internuclear separations differ from their equilibrium values corresponding to the minimum of potential energy surface of the molecule. In other words, the optical radiation can be efficiently converted into short-wavelength radiation if the molecule is either in a highly excited vibrational state or on the decaying term at the beginning of dissociation. These conditions obviously require special preparation of molecular medium in the experiment.

Numerical calculations were carried out using the widely accepted model (see, e.g., [7, 11, 16]) of the simplest molecular system, namely, a two-dimensional analogue of the X_2^+ ion with a smoothed Coulomb

potential $V(x, y)$ formed by two identical single-charged centers confining a single electron:

$$V(x, y) = -[(x - R/2)^2 + y^2 + a^2]^{-1} - [(x + R/2)^2 + y^2 + a^2]^{-1}. \quad (1)$$

Here, R is the internuclear distance and a is the smoothing parameter, which is usually chosen from the condition that the ionization energy for the ground electron term of the model ion coincides with its value for the real molecular ion. The particle ionization dynamics in the field of a laser pulse with electric field $E(t)$ linearly polarized along the y axis is described, in the dipolar approximation, by the Schrödinger equation (in atomic units):

$$i\frac{\partial\psi}{\partial t} = -\frac{1}{2}\left(\frac{\partial^2}{\partial x^2} + \frac{\partial^2}{\partial y^2}\right)\psi + V(x, y)\psi + yE(t)\psi. \quad (2)$$

In this work, molecular orientation is assumed to be fixed and perpendicular to the direction of the exciting laser field. This assumption is justified both by the experimentally proved possibility of aligning simple molecules by a long laser prepulse [15, 17–19] and by the short duration of the main powerful pulse with ensuing harmonic generation during the molecular ionization. We also ignore the collective effects caused by the radiation interaction with a large number of particles in the course of propagation in the ionized gas, such as phase and group mismatch, blue shift of the fundamental and higher harmonics, etc. The optimization of the nonlinear response of a single particle can be considered as the first step in the problem of designing a high-efficiency source of coherent VUV and X-ray radiation in a molecular gas.

The stationary electronic states in potential (1) can be obtained, e.g., by numerical imaginary-time integration of Eq. (2) with zero external field. The resulting potential energy curve $U(R)$ of molecular ion including the nuclear repulsion is shown in Fig. 1 for the smoothing parameter $a = (0.5)^{1/2}$. The equilibrium internuclear distance $R = 2.4$ corresponds to the ionization potential $I_p = 28.5$ eV, and the dissociation energy D is equal to 2.9 eV. These values are close to their experimental values for the real molecular ion H_2^+ ($R = 2$, $I_p = 29.9$ eV, $D = 2.8$ eV).

The oscillation period of nuclei with a mass of 1836 au at the potential well bottom is about 15 fs. This implies that, when studying the processes accompanying the ionization of a light molecule by a powerful femtosecond optical pulse, one must generally take into account the nuclear dynamics [10, 20] and at least supplement the set of Eqs. (1) and (2) with the equation for self-consistent evolution of the internuclear distance $R(t)$ [21]. However, our calculations show that, for heavier nuclei and/or molecular ionization during few periods of optical field, the distance R can be set fixed and corresponding to the running molecular size at the beginning of ionization, which will be assumed in what follows.

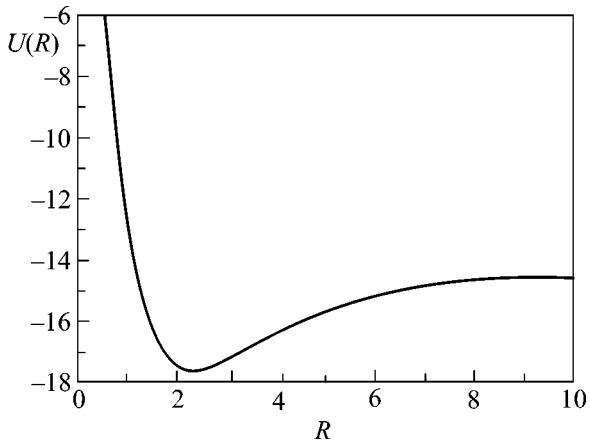

Fig. 1. Potential energy curve for the ground electronic state of a two-dimensional model of molecular ion (1) with $a = (0.5)^{1/2}$. The internuclear distance is in atomic units and energy is in electronvolts.

The mechanism underlying high-harmonic generation of optical radiation in the course of atomic ionization is well known [22, 23]. It is caused by the laser-synchronized bremsstrahlung of electrons ejected from atoms and accelerated by optical field to collide again with parent ions. The repetition of identical bremsstrahlung bursts emerging from a given physically small (compared to the radiation wavelength) volume with the half-period of ionizing field gives rise to the sharp peaks (harmonics) in the spectrum of nonlinear response of atomic system. Quite the reverse, if the ionization of almost all atoms and the recurrent electron collisions with parent ions proceed during one period of laser field, the atomic response corresponds to the excitation of an attosecond electromagnetic pulse with a broad continuum spectrum extending to the X-ray band.

Wave-packet diffusion in the course of electron acceleration outside the atom (molecule) is the main factor weakening the nonlinear response of an ionized particle in a linearly polarized optical field with nonrelativistic intensity. The acceleration time comprises a part of the optical period and far (by an order of magnitude and more) exceeds the interatomic time scale of electron wave function, as a result of which the wave packet spreads significantly by the time of recollision, and only a small fraction of accelerated electrons contribute to the bremsstrahlung generation. In classical terms, the transverse (with respect to the ionizing field) momentum component deflects the trajectory of the majority of escaped electrons far beyond the scattering center.

Evidently, the wave-packet spreading upon optically induced electron acceleration will slow down if a component characterized by a small transverse momentum

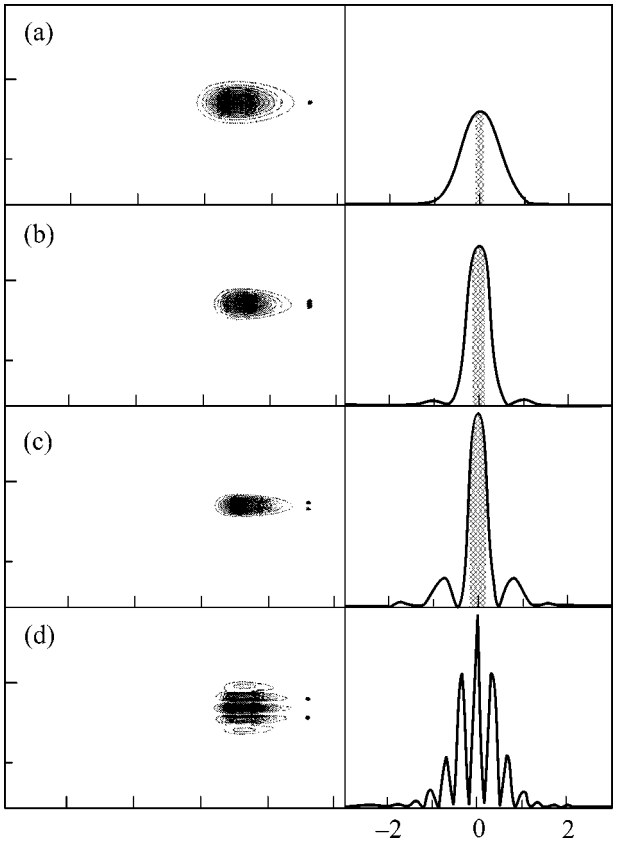

Fig. 2. Left: electronic wave packet before recollision with ion core (also shown in the figure); right: electron transverse-momentum distribution in the initial state. Results are obtained for R = (a) 2.4, (b) 5, (c) 7.2, and (d) 18.

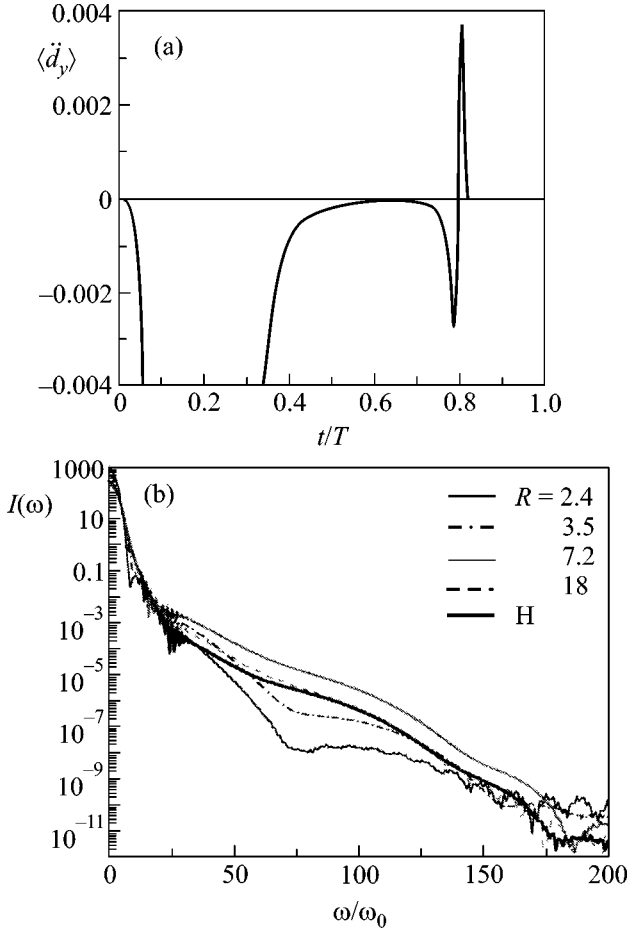

Fig. 3. Time dependence of the polarization response of a molecular ion in the laser-field direction for (a) R = 7.2, and the spectra of molecular response for (b) R = 2.4, 3.5, 7.2, and 18. Figure (b) also shows the response spectrum for H in a two-dimensional model of hydrogen atom with $V(x, y) = -(x^2 + y^2 + 0.5)^{-1/2}$.

increases in the initial ψ function. It is precisely this situation that is typical of molecular (contrary to atomic) systems, which necessarily contain a delocalized ψ-function component in the internuclear region to provide mutual attraction of nuclei.

A decrease in the wave-packet spreading upon increasing internuclear separation and, as a result, a sizable enhancement of the nonlinear response in the short-wavelength range of the spectrum is clearly seen in the regime of attosecond pulse generation upon the above-barrier ionization of a molecule during one period of a rapidly increasing laser field. The corresponding pattern is free of multiple wave-packet interference, which inevitably arises for the ionization extended over several field periods and hampers the unambiguous identification of the effect. Figure 2 shows the "snapshots" obtained by numerical integration of Schrödinger equation (2) for the electron wave packet before its recollision with the molecular core of size R = (a) 2.4, (b) 5, and (c) 7.2 in the electric field $E(t) = E_0[\exp(2\omega_0 t/\pi) - 1]\sin\omega_0 t$ (E_0 = 0.36, ω_0 = 0.114). The initial electron distribution $p(k_x) = \int_{-\infty}^{\infty} |\psi(k_x, k_y)|^2 dk_y$ in transverse momentum is also shown in Fig. 2. The cross-hatched regions correspond to the electrons displaced in the transverse direction at a distance shorter than R during free motion: $|k_x|\Delta t \le R$.

The time dependence of the second derivative $\langle \ddot{d}_y \rangle$ of the dipole moment of a molecular ion in the direction of the laser field demonstrates the excitation of a burst with a duration shorter than 200 as. This dependence and the corresponding response spectra are presented in Fig. 3 for various R values. Note that the generation efficiency of the short-wavelength quanta with frequencies $\omega > 30\omega_0$ is, at least, an order of magnitude higher for the internuclear separation R = 7.2 than for the equilibrium molecular configuration with R = 2.4.

The variation in the efficiency of frequency conversion with varying R is crucial in the comparison of the atomic and molecular responses. Evidently, the molecular ion transforms in the limit $R \longrightarrow \infty$ into a pair of noninteracting singly charged ions sharing a single electron. The recurrent bremsstrahlung directed per-

pendicular to the molecular axis is identical with the radiation of a single-electron atom. Thus, by increasing the internuclear separation in our model, we can answer the question of to what extent the molecular system is a more efficient generator of short-wavelength quanta than the analogous atomic system with the same number of radiating electrons. In Fig. 3, the heavy line corresponds to the spectrum of attosecond burst upon the ionization of an atom with the potential $V(x, y) = -(x^2 + y^2 + 0.5)^{-1/2}$. One can see that the gain for the optimal internuclear separation ($R \approx 7$) is almost an order of magnitude greater than for the atomic system over the entire short-wavelength portion of the spectrum. At the same time, the response of the atomic system is generally not small compared to the molecular system. Moreover, it exceeds, at least in our model, the molecular response in the equilibrium state ($R = 2.4$).

Note that the gradual transition from the molecular to atomic response is accompanied by the appearance of a new "cross" bremsstrahlung component at the intermediate nuclear distances. It is caused by the laser-accelerated electrons ejected from the ion and colliding with another ion. The presence of such electrons and their dominance over the delocalized electrons at $R \geq 20$ is reflected in the interference modulation of the wave-packet structure as it returns to the molecular core (Fig. 2d). At even larger internuclear distances, those wave-packet parts corresponding to the electrons that were initially localized near the attracting centers have no time to overlap in the course of acceleration and spreading, as a result of which the response becomes purely atomic.

The fact that the optimal internuclear distance for the energy conversion into the VUV and X-ray regions is larger than the equilibrium distance is confirmed by high-harmonic generation in the molecular ionization during several periods of optical field. This is illustrated by the results obtained within the framework of the same model of a molecular ion subjected to the field $E(t) = E_0 \sin^2(\omega_0 t/24)\sin\omega_0 t$ ($E_0 = 0.125$, $\omega_0 = 0.057$) corresponding to a laser pulse with a duration of 16 fs, peak intensity of 5×10^{14} W/cm^2, and a wavelength of 0.8 μm. Figure 4 shows the spectra of odd high-harmonic generation after smoothing with the averaging window equal to the excitation frequency. The maximum of integrated generation intensity in the spectral interval $5\omega_0 < \omega < 85\omega_0$ corresponds to the distance $R = 3.5$ and also exceeds (by five to seven times) the atomic response in the plateau region.

The optimization of nonlinear response, which was observed for the ionization from the ground electronic state of a molecular system, can occur at more complex initial conditions and for more complex quantum objects. It is conceivable that the presence of a greatest possible number of delocalized electrons with a small wave momentum in the direction transverse to the ionizing field is the main "indicator" in choosing the molecular structures and their states. In this respect,

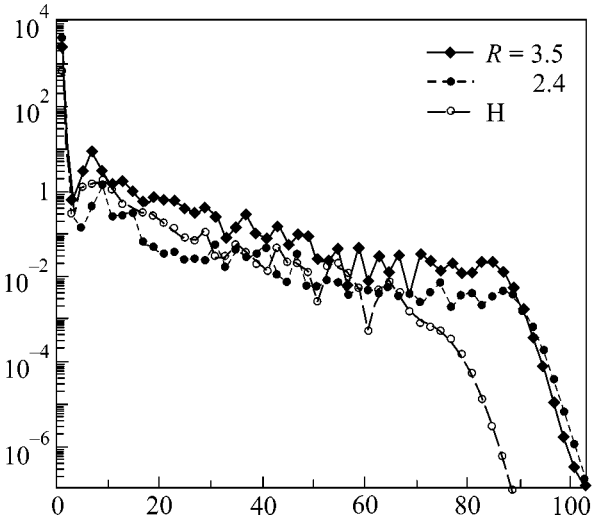

Fig. 4. Harmonic generation spectra of a molecular ion with $R = 2.4$ and 3.5 and (dashed line) of the H atom upon the action of a laser pulse with $E_0 = 0.125$ and $\omega_0 = 0.057$.

e.g., of a considerable interest are the excited electronic states of molecules (including the simplest ones), in which the spatial size of electron cloud is larger than in the ground state and, hence, is less subject to spreading upon the laser-induced acceleration. Our preliminary calculations of the model of the molecular ion H_2^+ in one of its lower lying excited initial electronic states show that the maximal efficiency of attosecond burst generation can be increased, in this case, at least by several times, as compared to the ionization from the ground electronic state.

Evidently, the optimal interaction regime between laser radiation and molecules can be attained only upon special preparation of a working gas in experiment. One such possibility consists of the preliminary orientation of molecules, their resonance excitation, or ionization by a low-intensity ultrashort laser pulse followed by the action of a powerful pulse on a gas with a time delay (relative to the ionizing pulse) that is determined by the time of optimal "expansion" of the molecule in the course of its oscillations or incipient dissociation.

In closing, let us assess the possibilities that are presented by the optimal high-harmonic generation regime in the experiments on molecular ionization. The energy conversion ratio into a high VUV harmonic achieved to date using a powerful femtosecond optical pulse under phase-matching conditions approaches 10^{-4} in inert gases [2]. An order-of-magnitude increase in this ratio upon changing to molecular gases increases the average coherent VUV-radiation power to 5 mW for a compact Ti:sapphire laser with a pulse duration of 20 fs, a repetition rate of 1 kHz, and an energy of 5 mJ. This level corresponds to the highest values that are presently

obtained only at large-scale accelerator facilities with free-electron lasers in the wavelength range $\lambda \sim 100$ nm.

This work was supported by the Russian Foundation for Basic Research (project no. 01-02-18006) and the Presidium of the Russian Academy of Sciences (programs "Femtosecond Optics" and "Quantum Macrophysics").

REFERENCES

1. R. A. Bartels, A. Paul, H. Green, *et al.*, Science **297**, 376 (2002).
2. J.-F. Hergott, M. Kovacev, H. Merdji, *et al.*, Phys. Rev. A **66**, 021801 (2002).
3. E. Takahashi, Y. Nabekawa, T. Otsuka, *et al.*, Phys. Rev. A **66**, 021802 (2002).
4. J. Andruszkow, B. Aune, V. Ayvazyan, *et al.*, Phys. Rev. Lett. **85**, 3825 (2000).
5. V. Ayvazyan, N. Baboi, I. Bohnet, *et al.*, Phys. Rev. Lett. **88**, 104802 (2002).
6. P. Moreno, L. Plaja, and L. Roso, Phys. Rev. A **55**, 1593 (1997).
7. R. Kopold, W. Becker, and M. Kleber, Phys. Rev. A **58**, 4022 (1998).
8. A. D. Bandrauk and H. Yu, Phys. Rev. A **59**, 539 (1999).
9. R. Numico, D. Giulietti, A. Giulietti, *et al.*, J. Phys. B: At. Mol. Opt. Phys. **33**, 2605 (2000).
10. T. Kreibich, M. Lein, V. Engel, and E. K. U. Gross, Phys. Rev. Lett. **87**, 103901 (2001).
11. D. G. Lappas and J. P. Marangos, J. Phys. B: At. Mol. Opt. Phys. **33**, 4679 (2000).
12. Y. Liang, S. Augst, S. L. Chin, *et al.*, J. Phys. B: At. Mol. Opt. Phys. **27**, 5119 (1994).
13. C. Lynga, A. L'Huillier, and C.-G. Wahlstrom, J. Phys. B: At. Mol. Opt. Phys. **29**, 3293 (1996).
14. N. Hay, R. de Nalda, T. Halfmann, *et al.*, Phys. Rev. A **62**, 041803 (2000).
15. R. Velotta, N. Hay, M. B. Mason, *et al.*, Phys. Rev. Lett. **87**, 183901 (2001).
16. M. Lein, N. Hay, R. Velotta, *et al.*, Phys. Rev. Lett. **88**, 183903 (2002).
17. B. Friedrich and D. Herschbach, Phys. Rev. Lett. **74**, 4623 (1995).
18. J. J. Larsen, H. Sakai, C. P. Safvan, *et al.*, J. Chem. Phys. **111**, 7774 (1999).
19. J. J. Larsen, I. Wendt-Larsen, and H. Stapelfeldt, Phys. Rev. Lett. **83**, 1123 (1999).
20. W. Qu, Z. Chen, Z. Xu, and C. H. Keitel, Phys. Rev. A **65**, 013402 (2002).
21. B. Rotenberg, R. Taieb, V. Veniard, and A. Maquet, J. Phys. B: At. Mol. Opt. Phys. **35**, L397 (2002).
22. P. B. Corkum, Phys. Rev. Lett. **71**, 1994 (1993).
23. K. C. Kulander, K. J. Schafer, and J. L. Krause, in *Super-Intense Laser-Atom Physics*, Ed. by B. Piraux, A. L'Huillier, and K. Rzazewski (Plenum, New York, 1993), p. 95, NATO ASI Ser., Ser. B **316**.

Translated by V. Sakun

JETP Letters, Vol. 77, No. 5, 2003, pp. 217–220. Translated from Pis'ma v Zhurnal Éksperimental'noĭ i Teoreticheskoĭ Fiziki, Vol. 77, No. 5, 2003, pp. 260–263.

Kinetics of Photoinduced Optical Anisotropy in Oxide Glass

M. K. Balakirev* and V. A. Smirnov

Institute of Semiconductor Physics, Siberian Division, Russian Academy of Sciences, pr. Akademika Lavrent'eva 13, Novosibirsk, 630090 Russia

** e-mail: balak@isp.nsc.ru*

Received December 5, 2002

Long-lived optical anisotropy generated in glasses by bichromatic mutually coherent radiation is associated with the accumulation of a built-in electric field. The kinetics of photoinduced anisotropy was studied within the framework of a phenomenological model taking into account the polarization- and current-induced mechanisms of field formation and the medium conductivity. The combination of the current and polarization mechanisms gives rise to new effects. The accumulation of anisotropy and its dark relaxation have a nonmonotonic character. For a sufficiently high and rapidly relaxing photoconductivity, "hidden writing" is possible, for which the anisotropy is absent during the course of bichromatic illumination, but it appears after switching off the light and relaxes slowly due to dark conduction. *© 2003 MAIK "Nauka/Interperiodica".*

PACS numbers: 78.20.Ek; 78.20.Jq

It is known [1–3] that a centrally symmetric medium becomes optically anisotropic under multichromatic coherent illumination. As a result, the refractive index changes and even-order effective polarizabilities appear in the medium. A change in polarizabilities is accompanied by a broad spectrum of observed effects: second harmonic generation [1, 2], self-diffraction [4], degenerate parametric amplification [5], etc. [6, 7]. This fact attracts the attention of researchers, because it presents new opportunities in scientific and practical applications.

The nature of anisotropy is associated with the formation of a long-lived built-in electric field in the medium. Although the detailed microscopic mechanisms of the formation of this field are highly diversified, all are based on the spatial asymmetry of the probabilities of optical transitions under the action of a multichromatic coherent light. From the phenomenological point of view, the kinetics of long-lived photoinduced anisotropy and the parameters governing the saturation time of anisotropy and its lifetime are of fundamental interest. This communication is devoted to this problem.

Let the medium be illuminated by mutually coherent light sources with the fundamental and doubled frequencies:

$$\mathbf{E}_m(\mathbf{r}, t) = \mathbf{E}_m(\mathbf{r})\exp i(\mathbf{k}_m\mathbf{r} - m\omega t + \varphi_m) + \text{c.c.},$$

$$\mathbf{E}_m(\mathbf{r}) = \mathbf{e}_m E_m(\mathbf{r}),$$

where $m = 1, 2$ refer to the fundamental and doubled frequencies, respectively; $\mathbf{k}_m$ and φ_m are, respectively, the wave vectors and phases; and $\mathbf{e}_m$ and $E_m(\mathbf{r})$ are, respectively, the polarizations and envelopes of the radiations.

In a system of localized electronic states, this radiation induces spatial asymmetry of optical electronic transitions between the localized levels. Due to geminate recombination, part of such electrons are restored to the initial state in a certain time τ. This mechanism generates long-lived polarization $\mathbf{P}_s(t, \mathbf{r})$ and the corresponding electric field $\mathbf{E}_p(t, \mathbf{r})$ in the medium. The other part of asymmetrically excited electrons transfer at large distances to produce a constant current density $\mathbf{J}_{CPG}$ in the medium. This is known as the coherent photogalvanic effect (CPGE) [8–10]. The separation of carriers by the current $\mathbf{J}_{CPG}$ gives rise to the space charge $\rho_J(t, \mathbf{r})$ and the corresponding electric field $\mathbf{E}_q(t, \mathbf{r})$. If the medium possesses nonzero conductivity σ, the fields will be screened and a compensating space charge $\rho_\sigma(t, \mathbf{r})$ will appear. Therefore, the total space charge is $\rho = \rho_\sigma(t, \mathbf{r}) + \rho_J(t, \mathbf{r})$, and the total electric field $\mathbf{E}(t, \mathbf{r})$ is the sum of polarization and space-charge fields. The accumulation and relaxation of $\mathbf{E}(t, \mathbf{r})$ depend on the partial excitation efficiencies, time τ, and medium conductivity.

Let us consider these processes in more detail. Define the total carrier flux density for the asymmetric transitions as

$$\mathbf{S} = \mathbf{j}AE_1^2E_2\cos(\Delta\mathbf{k}\mathbf{r} + \Delta\varphi),$$

where $\Delta\mathbf{k} = 2\mathbf{k}_1 - \mathbf{k}_2$; $\Delta\varphi = 2\varphi_1 - \varphi_2$; $\mathbf{j}$ is unit vector in the direction of asymmetric electron transfer:

$$\mathbf{j} = (\mathbf{e}_1(\mathbf{e}_1\mathbf{e}_2)C_1 + \mathbf{e}_2C_2)\left|(\mathbf{e}_1(\mathbf{e}_1\mathbf{e}_2)C_1 + \mathbf{e}_2C_2)\right|^{-1},$$

$C_{1,2}$ are the photogalvanic parameters; and $A = \left|(\mathbf{e}_1(\mathbf{e}_1\mathbf{e}_2)C_1 + \mathbf{e}_2C_2)\right|$ is the effective photogalvanic coefficient.

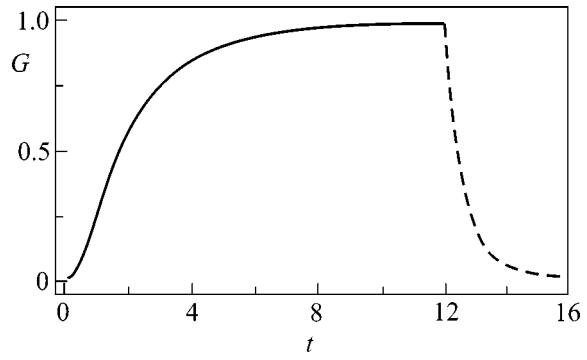

Fig. 1. Kinetics of field squared at $\xi > 1$.

We assume that the accumulation of space charge ρ and field $\mathbf{E}(t, \mathbf{r}) = E(t)\mathbf{E}(\mathbf{r})$ is described by the equations

$$\frac{d}{dt}\rho = -\mathrm{div}(\sigma\mathbf{E}(t, \mathbf{r}) + \mathbf{J}_{CPG}),$$
$$\mathrm{div}\mathbf{D} = 4\pi\rho; \quad \mathbf{J}_{CPG} = A_1\mathbf{S}. \tag{1}$$

The diffusion of charge carriers is ignored.

The constitutive equation for electric induction D is represented in the form

$$\mathbf{D} = \varepsilon\mathbf{E}(t, \mathbf{r}) + 4\pi\mathbf{P}_s(t, \mathbf{r}). \tag{2}$$

The change in $\mathbf{P}_s(t, r)$ under the action of mutually coherent radiations is described by the following model:

$$\frac{d}{dt}\mathbf{P}_s = -\frac{\mathbf{P}_s}{\tau} + \frac{A_2}{\tau}\mathbf{S}\tau. \tag{3}$$

In Eqs. (1)–(3), the constants $A_{1,2}$ characterize the relative fractions of asymmetrically photoexcited electrons for the photogalvanic effect (A_1) and polarization (A_2), so that $A_1 + A_2 = 1$.

By eliminating space charge from Eq. (1), one obtains

$$\left(\frac{d}{dt}E(t) + \frac{1}{\tau_m}E(t)\right)\mathrm{div}\mathbf{E}(r)$$
$$+\left(\frac{A_2}{\tau}\exp\left(-\frac{t}{\tau}\right) + \frac{A_1}{\tau}\right)\mathrm{div}\frac{4\pi\tau}{\varepsilon}\mathbf{S} = 0, \tag{4}$$
$$\tau_m \equiv 4\pi\sigma\varepsilon^{-1}.$$

For zero initial conditions, Eqs. (3) and (4) have the following solutions:

$$\mathbf{P}_s(t, \mathbf{r}) = A_2\left(1 - \exp\left(-\frac{t}{\tau}\right)\right)\mathbf{P}(\mathbf{r}),$$
$$\mathbf{P}(\mathbf{r}) = \mathbf{S}\tau; \tag{5}$$

$$\mathbf{E}(t, \mathbf{r}) = \frac{\tau_m}{\tau - \tau_m}\left(1 - \exp\left(-\frac{t}{\tau}\right)\right)A_2\mathbf{E}(\mathbf{r})$$
$$-\frac{\tau_m}{\tau - \tau_m}\left(1 - \exp\left(-\frac{t}{\tau_m}\right)\right)\left(1 - A_1\frac{\tau_m}{\tau}\right)\mathbf{E}(\mathbf{r}). \tag{6}$$

The spatial distribution of the field $\mathbf{E}(\mathbf{r})$ is found from the equation

$$\mathrm{div}(\varepsilon\mathbf{E}(\mathbf{r})) = 4\pi\mathrm{div}(\tau\mathbf{S})$$

and described the shape of the so-called photoinduced gratings [3].

For identical relaxation times, one has

$$\rho(t, \mathbf{r}, \tau \longrightarrow \tau_m) = (1 - \exp(-t/\tau_m))(A_2 + A_1)\rho(\mathbf{r}),$$
$$\mathbf{E}(t, \mathbf{r}, \tau \longrightarrow \tau_m) = -(1 - \exp(-t/\tau_m))A_1\mathbf{E}(\mathbf{r}).$$

Finally, the relaxation of accumulated field is described by the expression

$$\mathbf{E}(t, \mathbf{r}) = \frac{\tau_m}{\tau - \tau_m}\left(A_2\left(1 - \exp\left(-\frac{T}{\tau}\right)\right)\exp\left(-\frac{t}{\tau}\right)\right.$$
$$\left.-\left[\left(1 - \exp\left(-\frac{T}{\tau_m}\right)\right)\left(1 - A_1\frac{\tau_m}{\tau}\right)\exp\left(-\frac{t}{\tau_m}\right)\right]\mathbf{E}(\mathbf{r}),\right.$$

where time t is measured from the completion of illumination and T is the illumination time.

Let us briefly discuss this result.

1. ACCUMULATION

The electric fields of space charge and photoinduced polarization have different signs and compensate each other in part. For this reason, the resulting field may be lower than either of them. For a sufficiently prolonged illumination, the field tends asymptotically to the stationary value $\mathbf{E}_s(\mathbf{r}) = -A_1\tau_m\tau^{-1}\mathbf{E}(\mathbf{r})$. The accumulation kinetics is determined by the parameter $\xi = A_1\tau_m\tau^{-1}$.

If $\xi > 1$, the total field tends monotonically with time to its stationary value (Fig. 1; $T = 10\tau$, $\xi = 1.2$). All figures presented below show, for clearness, the relative value $G = E^2(t)E_M^{-2}$ that characterizes the efficiency of photoinduced second harmonic generation (PSHG). E_M^2 is the maximal value in the graph. Solid lines demonstrate the accumulation and dashed lines demonstrate the dark relaxation. Time is normalized to τ.

If $\xi < 1$, the total field first reaches its maximum whereupon tends to $E_s(\mathbf{r})$, which can be rather small compared to the maximal value (Fig. 2; $T = 6\tau$, $\xi = 0.03$). Such a PSHG behavior was observed recently in the TF-4 glass [11] and, earlier, in an optical fiber [12].

2. RELAXATION

The character of field relaxation depends on ξ, accumulation time T, and relative magnitudes of the accu-

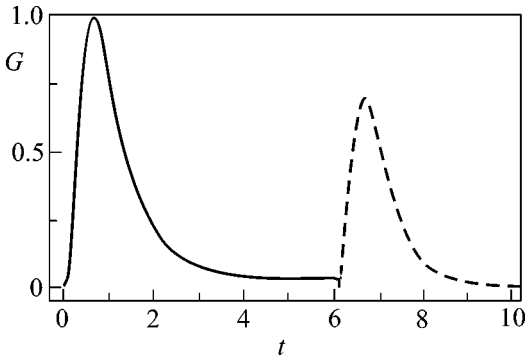

Fig. 2. Kinetics of field squared at $\xi < 1$.

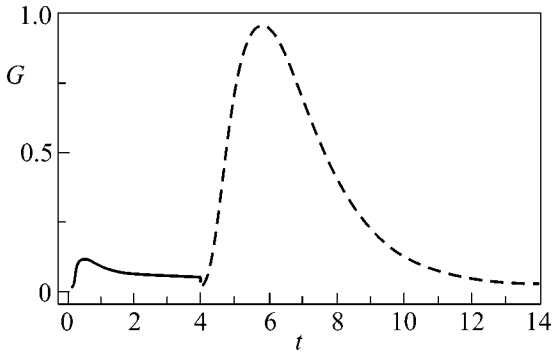

Fig. 3. Kinetics of field squared for high photoconductivity.

mulated fields. If $\xi > 1$, then the usual relaxation takes place (Fig. 1; $T = 10$, $\xi = 1.2$). If $\xi < 1$ and field magnitudes accumulated by the time $t = T$ are comparable, then the field rises in the time interval $t \sim \tau$ to a level corresponding to the accumulated charge field, after which it slowly relaxes to zero (Fig. 2; $T = 6\tau$, $\xi = 0.03$). Interestingly, the field can change sign during $t \sim \tau$ if the polarization field exceeds the charge field. This fact may substantially alter the observed PSHG dynamics. It should be emphasized that the illumination duration governs only the grating amplitude, while the grating lifetime is virtually equal to τ_m and can be rather long.

3. PHOTOCONDUCTIVITY EFFECT

Let the photoconductivity be sustained by photoexcited carriers that "instantly" recombine in time $\tau_R \ll \tau_m, \tau$. In other words, we assume that the conductivity is restored stepwise to its dark value after switching off the illumination. The maxwellian relaxation time $\tau_m(|E_1|^2, |E_2|^2) = T_m$ in the illuminated sample is assumed to be much shorter than the dark relaxation time; i.e., $T_m \ll \tau_m$.

In such a situation, the analysis of the accumulation process can be carried out using the grating write equations with the substitution $\tau_m \longrightarrow T_m$, so that the field relaxation can be described by the expression

$$E(t) = \frac{P_s}{\tau - \tau_m}\tau_m \exp\left(-\frac{t}{\tau}\right) + \left(E(T) - \frac{P_s}{\tau - \tau_m}\tau_m\right)\exp\left(-\frac{t}{\tau_m}\right),$$

where

$$E(T) = \frac{T_m}{(\tau - T_m)}A_2\left(1 - \exp\left(-\frac{T}{\tau}\right)\right) - \frac{T_m}{(\tau - T_m)}\left(1 - \exp\left(-\frac{T}{\tau_m}\right)\right)\left(A_2 + A_1 - A_1\frac{T_m}{\tau}\right),$$

$$P_s(T) = A_2\left(1 - \exp\left(-\frac{T}{\tau}\right)\right).$$

One can see that, under these writing conditions, the maximum attainable field level is considerably lower, and field tends to zero with the characteristic time T_m in the course of further writing. The behavior of dark relaxation is unusual; after switching off the light, the field reaches a maximum in a short time τ_R, whereupon relaxes to zero with the dark time τ_m (Fig. 3).

The physical nature of the phenomenon can be explained assuming, for simplicity, that the photoconductivity is large, $T_m \ll \tau$, and $\mathbf{J}_{CPG}$ is negligibly small. In this case, the polarization field is fully compensated, during writing, by the field of screening charge $\rho_\sigma(t, \mathbf{r})$. After the illumination is terminated, the polarization relaxes to zero with time τ, but the field of screening charge is retained, and it can be rather high. However, this field slowly relaxes to zero due to the low dark conductivity. Interestingly, if the photoconductivity is high, the process shows up as a "hidden writing," because there are no indications of optical anisotropy during the illumination, although it appears after switching off the light. At the same time, if τ is small, one can rapidly write the photoinduced grating, which will exist for a long time.

This phenomenon may be useful in practical applications. It is worthy of note that the photoconductivity can be produced by an outside light source and, thus, controlled independently. This not only allows one to control the process in those cases where the photoconductivity induced by bichromatic illumination is small but also provides a tool for studying the photoconductivity as such.

Note, in closing, that the physical picture may be essentially different upon inhomogeneous illumination, because, in this case, T_m also becomes spatially inhomogeneous. However, discussion of this issue is beyond the scope of this communication.

We are grateful to M.V. Éntin for helpful discussions. This work was supported by the Russian Founda-

tion for Basic Research, project nos. 99-02-39044 and 02-02-17695.

REFERENCES

1. Yu. V. Glushchenko and V. B. Smirnov, Opt. Spektrosk. **72**, 990 (1992) [Opt. Spectrosc. **72**, 538 (1992)].
2. D. S. Dianov and E. M. Starodubov, Kvantovaya Élektron. (Moscow) **22**, 419 (1995).
3. M. K. Balakirev, Phys. Vibr. **6**, 233 (1998).
4. M. K. Balakirev and V. A. Smirnov, Pis'ma Zh. Éksp. Teor. Fiz. **61**, 537 (1995) [JETP Lett. **61**, 544 (1995)]; M. K. Balakirev, L. I. Vostrikova, and V. A. Smirnov, Kvantovaya Élektron. (Moscow) **32**, 546 (2002).
5. M. K. Balakirev, L. I. Vostrikova, and V. A. Smirnov, Opt. Commun. **178**, 181 (2000).
6. M. K. Balakirev, L. I. Vostrikova, and V. A. Smirnov, Pis'ma Zh. Éksp. Teor. Fiz. **66**, 771 (1997) [JETP Lett. **66**, 809 (1997)].
7. B. P. Antonyuk and V. B. Antonyuk, Usp. Fiz. Nauk **171**, 61 (2001) [Phys. Usp. **44**, 53 (2001)].
8. É. M. Baskin and M. V. Éntin, Pis'ma Zh. Éksp. Teor. Fiz. **48**, 554 (1988) [JETP Lett. **48**, 601 (1988)].
9. V. B. Sulimov, Zh. Éksp. Teor. Fiz. **101**, 1749 (1992) [Sov. Phys. JETP **74**, 932 (1992)].
10. E. M. Baskin and M. V. Entin, in *Proceedings of International Workshop, Chicago, USA, 1998* (Kluwer Academic, London, 1998), p. 191.
11. B. P. Antonyuk, N. N. Novikova, N. V. Didenko, and O. A. Aktsipetrov, Phys. Lett. A **287**, 161 (2001).
12. B. Valk, E. M. Kim, and M. M. Salour, Appl. Phys. Lett. **51**, 722 (1987).

Translated by V. Sakun

JETP Letters, Vol. 77, No. 5, 2003, pp. 221–225. Translated from Pis'ma v Zhurnal Éksperimental'noĭ i Teoreticheskoĭ Fiziki, Vol. 77, No. 5, 2003, pp. 264–269.

On the Mechanism of the Runaway of Electrons in a Gas: The Upper Branch of the Self-Sustained Discharge Ignition Curve

A. N. Tkachev and S. I. Yakovlenko

Institute of General Physics, Russian Academy of Sciences, Moscow, 119991 Russia

Received January 23, 2003

Based on the results of simulation by the method of particles, it is shown that the Townsend mechanism of electron multiplication in a gas at a sufficiently large electrode spacing is valid at least up to such large values of E/p at which relativistic electrons are generated. On the other hand, the phenomenon of electron runaway in a gas is determined by the electrode spacing, which must be either comparable with or smaller than the characteristic electron multiplication length, rather than the local criteria accepted presently. It is shown that, for a particular gas, the critical voltage across the electrodes at which the runaway electrons comprise a significant fraction is a universal function of the product of the electrode spacing by the gas pressure. This function also determines the condition of self-sustained discharge ignition. It not only incorporates the known Paschen curve but also additionally contains the upper branch, which describes the absence of a self-sustained discharge at a high voltage sufficiently rapidly supplied across the electrodes. © *2003 MAIK "Nauka/Interperiodica"*.

PACS numbers: 51.50.+v

The phenomenon of electron runaway in a fully ionized plasma lies in the fact that, in a sufficiently strong electric field, electrons gain a higher energy in their free paths than they lose in collisions with plasma particles. The Coulomb cross sections drop quadratically with growing energy of the relative motion of colliding particles. Therefore, if an external electric field occurs in the plasma, a certain fraction of high-energy electrons will always be constantly accelerated. The electron runaway phenomenon in a plasma was predicted long ago [1]. Numerical calculations [2, 3] and an analytic consideration for weak fields [4] were also carried out long ago. This phenomenon is significant for impurity diagnostics and energy balance in tokamak plasmas [5].

The phenomenon of electron runaway is also observed in gases [6, 7]. So-called open discharges [8–11], used, in particular, for laser pumping [12, 13], were created on its basis. Below, it will be shown that, contrary to the accepted point of view, the mechanism of electron runaway in a gas-discharge plasma is totally different from that in a fully ionized plasma. Electron runaway is carried out within the framework of the Townsend ionization mechanism (see, e.g., [14] about this mechanism). In this mechanism, the energy gained in the field is compensated by the expenditure for gas excitation and ionization. In this case, the runaway electrons arise when the characteristic multiplication length (reciprocal Townsend coefficient) becomes comparable with or exceeds the electrode spacing.

ON ELECTRON MULTIPLICATION AND RUNAWAY

Townsend Multiplication Mechanism

Consider the propagation of electrons in a neutral gas between two parallel planes with a voltage U imposed across them. Electrons are generated at the cathode and move to the anode, undergoing elastic and inelastic collisions with gas atoms. Additional electrons are generated upon ionization. The situation when the arrival of electrons into a particular range of velocities due to inelastic collisions is compensated by their escape from a particular point of the space is described by the equation

$$v_x \frac{\partial}{\partial x}(N_e(x) f(x, v)) = N_e(x) N \int \sigma_{\text{i.c.}}(\mathbf{v}, \mathbf{v}') v' f(x, \mathbf{v}') d\mathbf{v}'. \quad (1)$$

Here, x is the distance to the cathode; v is the electron velocity; $N_e(x)$ is the electron density; $f(x, \mathbf{v})$ is the electron distribution function normalized to unity ($\int f(x, \mathbf{v}) dv = 1$); N is the density of neutral atoms; and the expression $N\sigma_{\text{i.c.}}(\mathbf{v}, \mathbf{v}')v'$ determines the frequency of inelastic collisions of an electron with a neutral atom at which the incident electron has a velocity in the range $(\mathbf{v}', \mathbf{v}' + d\mathbf{v}')$, and the collisions generate new electrons in the velocity range $(\mathbf{v}, \mathbf{v} + d\mathbf{v})$.

Let us assume further that the distribution function $f(x, \mathbf{v})$ does not depend on the coordinate x. Then, integrating Eq. (1) over $d\mathbf{v}$ gives the Townsend equation

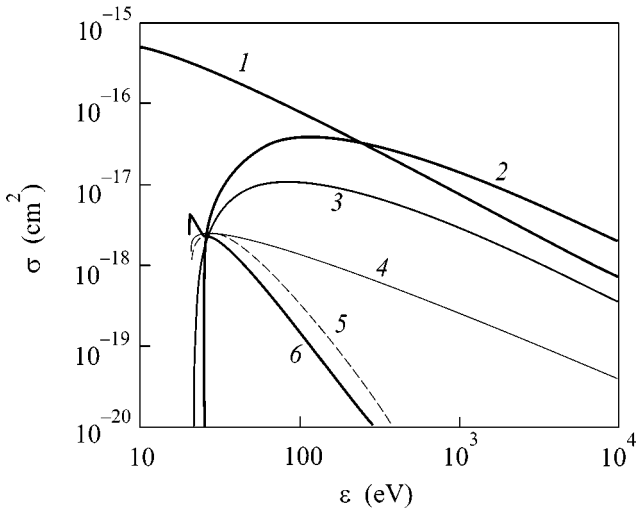

Fig. 1. Energy dependence of the cross section for an electron collision with a helium atom: (*1*) inelastic-collision cross section $\sigma_{el}(\varepsilon)$, (*2*) ionization cross section $\sigma_i(\varepsilon)$, (*3*) 2^1P excitation cross section, (*4*) 2^1S excitation cross section, (*5*) 2^3P excitation cross section, and (*6*) 2^3S excitation cross section (by the data from [16–18]).

describing the exponential growth of electrons in the avalanche

$$dN_e(x)/dx = \alpha_i N_e(x), \quad \alpha_i \equiv \nu_i/u_d,$$
$$\nu_i \equiv \int \sigma_{i.c.}(\mathbf{v}')\, v' f(\mathbf{v}')d\mathbf{v}', \quad u_d \equiv \int v_x f(\mathbf{v})d\mathbf{v}. \qquad (2)$$

Here, $\sigma_{i.c.}(v) = \int \sigma_{i.c.}(\mathbf{v}', \mathbf{v})d\mathbf{v}'$ is the total cross section for an inelastic electron–neutral collision and α_i is the known Townsend coefficient expressed through the ionization frequency ν_i and the electron drift velocity u_d.

Thus, two fundamental assumptions provide the basis for the Townsend model: (a) on the compensation of electrons arising at a given x by their drift and (b) on the independence of the form of the distribution of electrons over velocities from x.

On the Runaway Criterion

As distinct from the commonly accepted local criteria for electron runaway, we will consider that the runaway electrons arise in the case when the electrode spacing d becomes comparable with the characteristic multiplication length, that is, the reciprocal Townsend coefficient α_i^{-1}. At $\alpha_i d \ll 1$, the runaway electrons must predominate in the spectrum of electrons that reach the anode.

At a sufficiently large value of the ratio of electric field strength $E = U/d$ to gas density N (or pressure p), an electron gains a sufficiently high energy $\varepsilon \equiv m_e v^2/2 = eEl$ over the mean free path $l = 1/\sigma N$. At this energy, the overall cross section of all processes σ starts to decrease. This leads to a decrease in the Townsend coefficient (an increase in the multiplication length) and to the appearance of runaway electrons. In this case, as distinct from the currently prevailing point of view, the Townsend mechanism of electron multiplication itself remains in force for particular values E and p if the value of d is sufficiently large. Correspondingly, as the criterion for the appearance of a considerable number of runaway electrons, we take

$$\alpha_i(E_{cr}, p)d = 1. \qquad (3)$$

On the other hand, it is commonly accepted that runaway electrons arise when the value of E/p exceeds a certain critical value that does not depend on d [6, 7, 14].

RUNAWAY ELECTRONS IN HELIUM

Model Used

In order to confirm the above suggestion, the multiplication and runaway of electrons in helium were simulated based on one of the modifications of the method of particles [15]. Electrons were generated at the cathode with a randomly directed velocity, a Poisson distribution of their starting energy, and the average energy $\varepsilon_0 = 0.2$ eV. The equations of motion of all the electrons were solved at short time steps, and elastic and inelastic collisions were simulated with probabilities determined by the cross sections of elementary processes. Figure 1 presents the cross sections for various processes used in this work, based on the data from works [16–18].

Townsend Ionization Regime

Calculations reveal that the Townsend ionization regime actually takes place and runaway electrons are virtually absent at all the considered values of the reduced field strength E/p = 5–5000 V torr^{-1} cm^{-1} at sufficiently large electrode spacings $d \gg \alpha_i^{-1}$. With increasing distance from the cathode x, the acts of excitation and electron generation exponentially grow in number, and a constant average velocity and a constant average energy of electrons are attained at sufficiently large distances from the cathode (see Fig. 2). The distribution function of electrons reaching the anode attains a maximum at low energies. The slopes of the logarithms of the number of acts of ionization and the current determines the Townsend multiplication coefficient α_i. The multiplication coefficient α_i, as commonly accepted, is proportional to the gas density (pressure) and essentially depends on the reduced field strength E/p. The following approximation is known for helium [14]:

$$\alpha_i = 4.4p\exp\left(-\frac{14p}{E}\right), \qquad (4)$$

where, from here on, α_i is measured in cm^{-1}; the pressure p, in torr; and the field strength E, in V/cm.

However, calculations show (Fig. 3) that this approximation is correct only for a relatively small

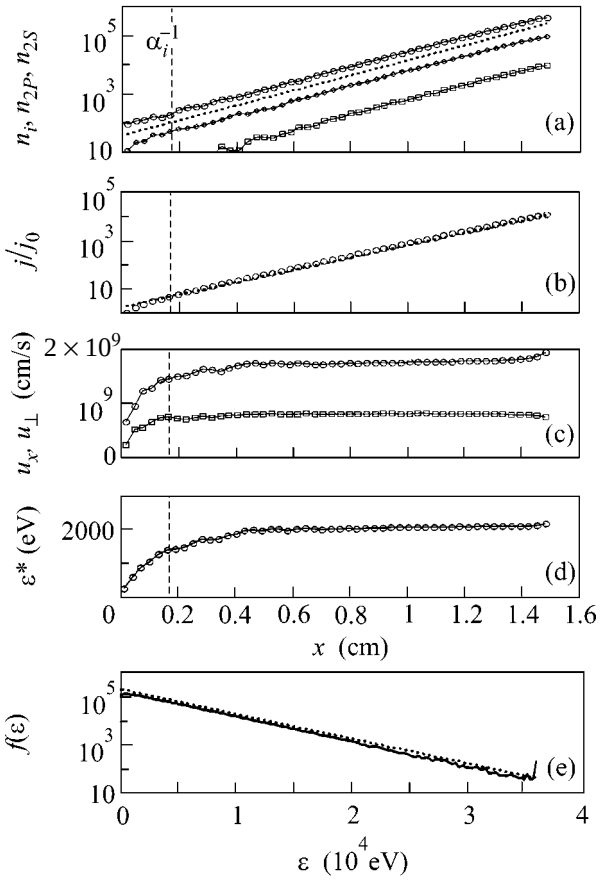

Fig. 2. Characteristics of electron multiplication in the Townsend regime as a function of the distance to the cathode x (measured in cm) at the following parameters: $N_{He} = 5.15 \times 10^{17}$ cm^{-3} (p = 16 torr), U = 36 kV, d = 15 mm, and E = 24 kV/cm (E/p = 1500). (a) The amount of the generated ions n_i (circles) and atoms excited to the 2^1P (n_{2P}, rhombuses) and 2^1S (n_{2S}, squares) states; the dotted line corresponds to the dependence $40\exp(5.9x)$. Correspondingly, $\alpha_i = 5.9$ cm^{-1}, and $\alpha_i d \approx 9$. (b) The ratio of electron flux at a particular point $j(x)$ to electron flux from the cathode j_0; the dotted line corresponds to the dependence $1.7\exp(5.9x)$. (c) The projection of the electron velocity onto the x axis directed along the electric field u_x (circles) and the magnitude of the velocity $u_\perp$ in the plane perpendicular to the x axis (squares). (d) The average electron energy. (e) The energy distribution function of electrons reaching the anode. The solid curve corresponds to the calculated results, and the dotted line corresponds to the dependence $2 \times 10^5 \exp(-\varepsilon/4200)$.

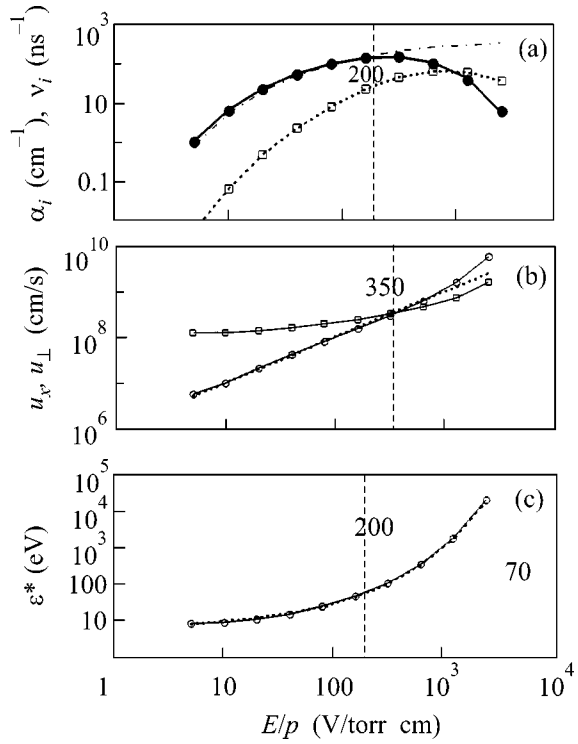

Fig. 3. Dependence of ionization and drift characteristics on the reduced field strength E/p_{He}. Points were obtained at various values of the field strength. Unless otherwise specified, $N_{He} = 3.22 \times 10^{18}$ cm^{-3} (p = 100 Torr). (a) Values of the Townsend coefficient normalized to pressure α_i/p (black circles) and ionization frequencies ν_i/p_{He} (squares) obtained by simulations at various values of the field strength. The heavy solid line corresponds to the approximation by Eq. (8), and the dot-and-dash line corresponds to the approximation by Eq. (4). The straight crosses correspond to α_i/p at p = 10 Torr, and the skew crosses correspond to α_i/p at p = 1 Torr. (b) The average projection of the electron velocity onto axis x directed along the electric field u_x (circles) and the average magnitude of the velocity $u_\perp$ in the plane perpendicular to the x axis (squares). Obtained by simulations at various values of the field strength. The dotted curve corresponds to the linear dependence by Eq. (5). (c) The average electron energy. Obtained by simulations at various values of the field strength. The dotted curve corresponds to the dependence by Eq. (6).

reduced field strength $E/p < 200$. At large values of E/p, the multiplication coefficient α_i starts to drop. The drop in α_i with increasing E/p is related to the drop in the ionization cross section at $\varepsilon > 100$ eV, and the average energy of electrons at E/p = 200 just comprises a close value ε^* = 70 eV.

The average velocity of electrons along the field u_x at small values of E/p is significantly smaller than the average magnitude of the transverse velocity $u_\perp$. The average velocities u_x and $u_\perp$ become equal only at E/p = 350. At $E/p < 350$, the directed velocity depends almost linearly on the field strength

$$u_x = 10^6 E/p. \quad (5)$$

The dependence of the average energy measured in eV on the field strength can be approximated by the equation

$$\varepsilon^* = 5.5\exp[(E/40p)^{1/2}]. \quad (6)$$

The fact that $u_x \ll u_\perp$ for small fields ($E/p \ll 350$) is explained in the following way. The velocity projection

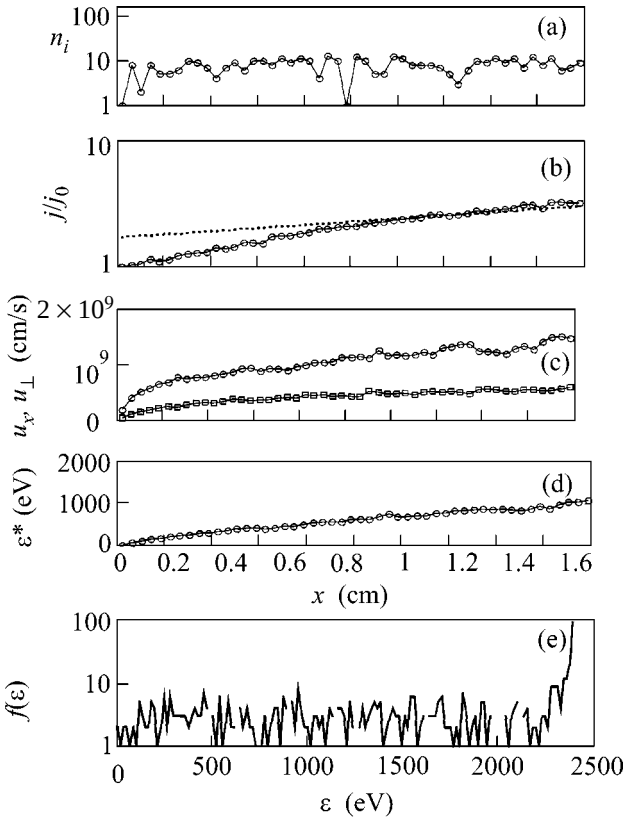

Fig. 4. Ionization by runaway electrons. The same as in Fig. 2 at the same value E/p = 1500 and p = 16 Torr, but at U = 2.4 kV and d = 1 mm. Correspondingly, $\alpha_i d \approx 0.6$. Such parameters are characteristic of open discharges.

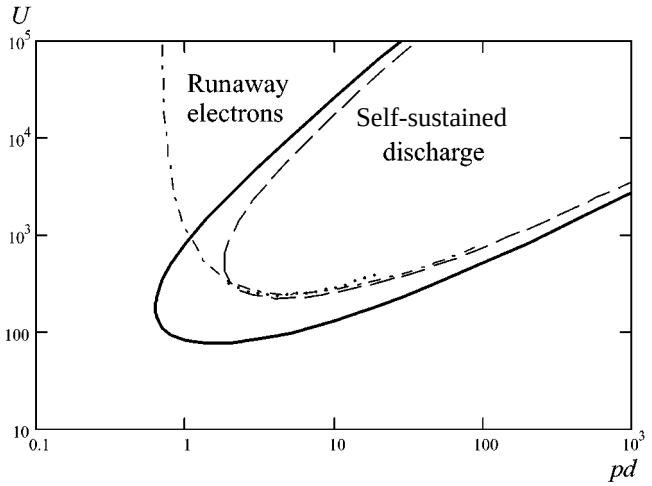

Fig. 5. Curve characterizing the criterion for electron runaway (heavy solid curve), curve (dashed) characterizing the criterion for discharge ignition ($L = \ln(1 + 1/\gamma) = 2.89$) obtained on the basis of Eq. (7), and experimental Paschen curve (dotted line) [14]. The dot-and-dash curve corresponds to the approximation given by Eq. (4). In the outer regions with respect to the heavy solid curve, electrons run away having no time to multiply. The inner region of the dashed line corresponds to a self-sustained discharge.

onto the x axis can take both positive and negative values. At the same time, the magnitude of the transverse velocity is always positive. Therefore, in weak fields, when the velocity only slightly increases during the free path of an electron from one elastic collision to another and the distribution over velocities is almost isotropic, the average value of the velocity projection u_x is considerably lower than the average value of the magnitude of the transverse velocity $u_\perp$. At high fields, when an electron gains a considerable energy during its free path, scattering becomes essentially nonisotropic, small-angle scattering prevails, and u_x becomes larger than $u_\perp$.

Runaway Electrons

The Townsend ionization regime is attained at a certain distance from the cathode $x \sim \alpha_i^{-1}$, which corresponds to the characteristic multiplication length (see Fig. 2). On the other hand, if $d < \alpha_i^{-1}$, the electron multiplication pattern changes radically (see Fig. 4). A significant part of electrons accelerate continuously: with increasing distance to the cathode x, both u_x and ε* grow. At the same time, the peak of the energy distribution function of electrons reached the anode corresponds to the maximum value of the energy $eU = eEd$ gained by an electron in its path from the cathode to anode.

The criterion for the appearance of a considerable number of runaway electrons given by Eq. (3) can be rewritten in the universal form based on the character of the dependence of α_i on E and p. Assuming that $\alpha_i(E, p) = p\xi(E/p)$, where $\xi(E/p)$ is a function characteristic of the particular gas, we obtain for the criterion given by Eq. (3)

$$pd\xi(U_{cr}/pd) = 1. \qquad (7)$$

This equation gives an implicit dependence of the critical voltage U_{cr} at which large-scale electron runaway takes place on the product of the electrode spacing by the pressure pd. Based on the results of our numerical simulations and known experimental data, the following approximations can be proposed for helium:

$$\xi(E/p) = 5.4\exp\left[-\left(\frac{14}{E/p}\right)^{1/2} - \frac{1.5\times 10^{-3}E}{p}\right], \qquad (8)$$

where function ξ is measured in Torr^{-1} cm^{-1}.

A curve $U_{cr}(pd)$ constructed based on the results of numerical calculations and Eq. (7) is presented in Fig. 5. The curve that determines the criterion for discharge ignition has a similar shape. Actually, the dis-

charge ignition potential $U_{br}(pd)$ is determined by the following condition (see, for example, [14]):

$$\alpha_i(E, p)d = \ln(1 + 1/\gamma)$$
$$\text{or } pd\xi(U_{br}/pd) = L, \quad L \equiv \ln(1 + 1/\gamma). \tag{9}$$

Here, γ is the secondary electron emission coefficient.

Comparing the equations for the criteria for discharge ignition (Eq. (9)) and the criterion for electron runaway (Eq. (7)) gives the relation $U_{br}(pd) = LU_{cr}(pd/L)$, which was used in constructing curve $U_{br}(pd)$ in Fig. 5.

The dependence $U_{br}(pd)$ obtained contains principally new information as compared to the known Paschen curve (Fig. 5). It is known that a Paschen curve is characterized by the right-hand and left-hand branches directed from the minimum of $U_{br}(pd)$ to the regions of large and small pd values. These branches are actually obtained, and the results of our calculations are in a good agreement with experimental data. However, according to our consideration, the self-sustained discharge ignition curve must additionally contain an upper branch due to the drop in α_i with increasing E/p. Finding the minimum value of pd_{min} at which self-sustained discharge ignition is still possible (for helium, $pd_{min} \approx 1.8$ Torr cm) is another important result of our consideration.

The existence of the upper curve of the self-sustained discharge ignition curve is quite understandable from the general considerations. This branch is due to the drop in inelastic cross sections with increasing electron energy. However, to date this branch has not been investigated. In order to observe this branch, the voltage across the electrodes must be built up sufficiently rapidly until the ionization wave reaches the anode and the plasma short-circuits the electrodes.

Thus, we showed that the Townsend mechanism of electron multiplication is valid for a sufficiently large electrode spacing at least up to the large values of E/p at which relativistic electrons are generated. On the other hand, the phenomenon of electron runaway in a gas is not determined, as is commonly accepted, by the predominance of the acceleration of an electron in the field over its deceleration due to collisions, which leads to a local criterion for runaway. The runaway of electrons in a gas arises when the electrode spacing turns out to be comparable with or less than the characteristic electron multiplication length. Therein lies the principal difference between the phenomena of runaway in a Coulomb plasma and a gas. This difference is due to the fact that, in a fully ionized plasma, new electrons with relatively small velocities are not generated, but the existing electrons are accelerated. In contrast, in a gas at sufficiently large electrode spacings, the number of the generated electrons is exponentially high. Some amount of fast electrons that have not participated in collisions becomes negligibly small against their background.

It is also shown that for a particular gas the critical voltage across the electrodes at which the runaway electrons comprise a significant fraction is a universal function of the product of the electrode spacing by the gas pressure. This function also determines the condition for self-sustained discharge ignition. It describes a Paschen curve but additionally contains an upper branch, which describes the absence of a self-sustained discharge at a high voltage sufficiently rapidly supplied across the electrodes. An approximation of this function for helium is given.

We are grateful to V.F. Tarasenko for stimulating discussions.

This work was supported by the International Science and Technology Center (ISTC project no. 1270).

REFERENCES

1. R. G. Giovanelly, Philos. Mag. **40**, 206 (1949).
2. H. Dreiser, Phys. Rev. **115**, 238 (1959); Phys. Rev. **117**, 329 (1960).
3. R. M. Kurlsrud, Y. C. Sun, N. K. Winson, and H. A. Fallon, Phys. Rev. Lett. **31**, 690 (1973).
4. A. V. Gurevich, Zh. Éksp. Teor. Fiz. **39**, 1296 (1960) [Sov. Phys. JETP **12**, 904 (1960)].
5. V. S. Marchenko and S. I. Yakovlenko, Fiz. Plazmy (Moscow) **5**, 590 (1979) [Sov. J. Plasma Phys. **5**, 331 (1979)].
6. L. P. Babich, T. V. Loĭko, and V. A. Tsukerman, Usp. Fiz. Nauk **160** (7), 49 (1990) [Sov. Phys. Usp. **33**, 521 (1990)].
7. Yu. D. Korolev and G. A. Mesyats, *The Physics of Pulse Breakdown* (Nauka, Moscow, 1991).
8. G. V. Kolbychev, P. D. Kolbycheva, and I. V. Ptashnik, Zh. Tekh. Fiz. **66** (2), 59 (1996) [Tech. Phys. **41**, 144 (1996)].
9. Yu. E. Kolyada, Pis'ma Zh. Tekh. Fiz. **26** (16), 52 (2000) [Tech. Phys. Lett. **26**, 721 (2000)].
10. A. R. Sorokin, Pis'ma Zh. Tekh. Fiz. **28** (9), 14 (2002) [Tech. Phys. Lett. **28**, 361 (2002)].
11. A. P. Bokhan and P. A. Bokhan, Pis'ma Zh. Tekh. Fiz. **28** (11), 21 (2002) [Tech. Phys. Lett. **28**, 454 (2002)].
12. V. I. Derzhiev, V. F. Tarasenko, S. I. Yakovlenko, and A. M. Yancharina, in *Plasma Lasers of Visual and Near Ultraviolet Ranges*, Ed. by S. I. Yakovlenko (Nauka, Moscow, 1989), p. 5, Tr. Inst. Obshch. Fiz. Akad. Nauk SSSR **21**.
13. S. I. Yakovlenko, in *An Encyclopedia of Low-Temperature Plasma*, Ed. by V. E. Fortov (Nauka/Interperiodika, Moscow, 2000), Introductory Vol. 4, p. 262.
14. Yu. P. Raĭzer, *The Physics of Gas Discharge*, 2nd ed. (Nauka, Moscow, 1992), p. 43.
15. A. N. Tkachev and S. I. Yakovlenko, Proc. SPIE **4747**, 271 (2002); Laser Phys. **12** (7), 1022 (2002).
16. E. Krishnakumar and S. K. Srivastava, J. Phys. B **21** (6), 1055 (1988).
17. D. V. Fursa and I. Bray, Phys. Rev. A **52** (2), 1279 (1995).
18. J. C. Nickel, K. Imre, D. F. Register, and S. Trajmar, J. Phys. B **18** (1), 125 (1985).

Translated by A. Bagatur'yants

JETP Letters, Vol. 77, No. 5, 2003, pp. 226–229. Translated from Pis'ma v Zhurnal Éksperimental'noĭ i Teoreticheskoĭ Fiziki, Vol. 77, No. 5, 2003, pp. 270–274.

Oscillations in the Threshold Photoemission Spectra of GaN(0001) with Submonolayer Cs Coverages

I. V. Afanas'ev, G. V. Benemanskaya, V. S. Vikhnin, G. É. Frank-Kamenetskaya, and N. M. Shmidt

Ioffe Physicotechnical Institute, Russian Academy of Sciences, St. Petersburg, 194021 Russia

Received November 18, 2002; in final form, February 6, 2003

It is found that Cs adsorption on the *n*-type GaN(0001) surface generates an unusual change in the electronic properties of the surface and the near-surface space-charge layer, which leads to the appearance of photoelectron emission upon excitation in the transparent region of GaN. It is established that the photoemission is due to the formation of quasimetallic states induced by Cs adsorption in the band-bending region near the surface. The behavior of the photoemission threshold upon excitation by *s*-polarized light is studied as a function of the Cs coverage. It is found that the minimum value of the threshold corresponds to ~1.4 eV at a concentration of Cs atoms of $\sim 4.5 \times 10^{14}$ atom/cm^2 in the submonolayer coverage. A new effect is revealed, namely, the appearance of oscillations in the spectral curves of threshold photoemission. A model is proposed for photocurrent oscillations that takes into account the formation of quasimetallic states in the near-surface layer of GaN band bending and the occurrence of interference in the GaN slab upon light irradiation in the transparent region.

PACS numbers: 73.20.-r; 79.60.Dp

Studying the electronic properties of adsorbed metallic coverages on the surface of group III nitrides is of both fundamental and applied importance, which is determined by the prospects for using these systems in creating emission and photodetector devices [1–3]. The GaN(0001) surface is of special importance for obtaining Schottky barriers and photoemitters in the near ultraviolet region. Recent studies have shown that the adsorption of Cs on epitaxial GaN(0001) layers of the *p* type [4, 5] and the *n* type [6] leads to a decrease in the work function φ, a change in the electron affinity at the surface, and a certain modification of the spectrum of intrinsic surface states lying below the valence band edge. The adsorption of Cs on the *n*-type GaN(0001) was studied by ultraviolet and x-ray photoemission spectroscopy at a temperature of 150 K [6]. It was determined that the work function for the pure surface φ ~ 4.3 eV decreases down to a value of φ ~ 1.35 eV at a certain unidentified Cs coverage. It was found that cesium is adsorbed layer by layer, and the sticking coefficient of cesium apparently decreases approximately by half in the formation of the second layer. The authors did not find the appearance of cesium-induced occupied surface states in the GaN band gap and in the vicinity of the conduction band edge.

It should be noted that a sharp decrease in the work function down to a value φ ~ 1.35 eV is observed upon Cs adsorption only on the *n*-type GaN(0001) surface, whereas the minimum value reached on the *p*-type GaN(0001) surface is φ ~ 3.5 eV [5]. In this connection, studying the photoemission properties of the *n*-type Cs/GaN(0001) system in the threshold excitation region is of special interest. The threshold photoemission spectroscopy (TPS) technique with *s*- and *p*-polarized excitation was successfully applied to studying the surface state spectrum and changing the work function and ionization energy in the case of Cs adsorption on the surface of semiconductors with a relatively small band gap, such as Si(111), Si(100), and GaAs(100) [7, 8]. The method is based on the separation of bulk and surface photoemission and on the effect of the near-threshold enhancement of photoemission from surface states. Under *s*-polarized light and the tangential component of *p*-polarized light, bulk electron states from the valence band of the substrate are excited. In this case, photoemission proceeds from the near-surface region, the size of which is determined by the escape depth of ~20 nm for low-energy electrons. This conventional quasibulk threshold photoemission takes place under the optical excitation of valence band states; hence, the photoemission threshold $h\nu_s$ for *s*-polarized light corresponds to an ionization energy equal to the position of the valence band edge at the surface with respect to the vacuum level. The normal component of *p*-polarized light excites surface states localized directly at the surface at a depth of ~0.5 nm. The occurrence of surface states leads to a significant difference in the photoemission thresholds $h\nu_s$ and $h\nu_p$ and also to a difference in the photoemission spectra $I_s(h\nu)$ and $I_p(h\nu)$ for *s*- and *p*-polarized excitation, respectively. The TPS technique is described in detail in [7–9].

This work is devoted to studying the *n*-type Cs/GaN(0001) system at various submonolayer cesium

coverages with the use of the TPS technique. It has been found that Cs adsorption on the GaN(0001) surface gives rise to a sharp decrease in the photoemission threshold $h\nu_s$, which shifts to the visible spectral region. The variation of the threshold $h\nu_s$ has been studied as a function of the Cs coverage. It has been found that the bulk photoemission threshold $h\nu_s$ in this case corresponds to the work function $\varphi = h\nu_s$ and is determined by photoemission from quasimetallic states in the conduction band when the band edge at the surface lies below the Fermi level. Thus, the formation of a degenerate electron gas layer induced by Cs adsorption has been detected in the GaN(0001) near-surface region. A new effect has been observed for photoemission, namely, the appearance of oscillations in the spectral dependences of the photoemission current. It has been found that the oscillation period in the spectrum is constant in energy and does not change for various coverages of the adsorbed Cs. The data obtained indicate that the nature of oscillations is associated with the occurrence of several factors, the main of which are, first, the existence of the near-surface layer of a degenerate electron gas and, second, the occurrence of multiple-beam interference in the GaN slab upon light irradiation in the transparent region. A model of the phenomenon observed has been proposed.

The experiment was performed *in situ* in an ultrahigh vacuum $P < 1 \times 10^{-10}$ torr at room temperature. An *n*-type sample doped with silicon (2×10^{17} cm^{-3}) 4-μm thick represented an epitaxial GaN(0001) layer grown on a sapphire substrate by MOCVD epitaxy. Data of atomic force microscopy pointed to a good quality of the surface. The sample was annealed directly in a vacuum at a temperature of ~800°C. Atomically pure cesium was evaporated on the surface from a standard source. The dose of the adsorbed Cs at a minimum of the work function was determined *in situ* by the procedure described in [8]. Photoemission was excited by monochromatic light incident on the sample at an angle of 45°. The $I_s(h\nu)$ and $I_p(h\nu)$ spectra of integral photoemission currents were studied upon excitation by *s*- and *p*-polarized light, respectively. Photoemission currents were measured in the range 10^{-8}–10^{-13} A, and the measurement error did not exceed 10%.

The variation of the photoemission threshold $h\nu_s$ is given in Fig. 1 as a function of the time of Cs evaporating on the *n*-type GaN(0001) surface. The points in the curve in Fig. 1 were obtained from an approximation of the spectral dependences of the photoemission $I_s(h\nu)$, which were measured for each Cs evaporating time. A sharp decrease in the threshold energy $h\nu_s$ down to a value of (1.40 ± 0.03) eV was found at a cesium evaporating time t_{min} ~ 700 s. It was found that the Cs dose corresponding to the time t_{min} comprises ~4.5×10^{14} atom/cm^2. This coverage corresponds to ~0.5 monolayer of Cs and, hence, lies in the submonolayer range. The surface concentration of Cs on GaN(0001)

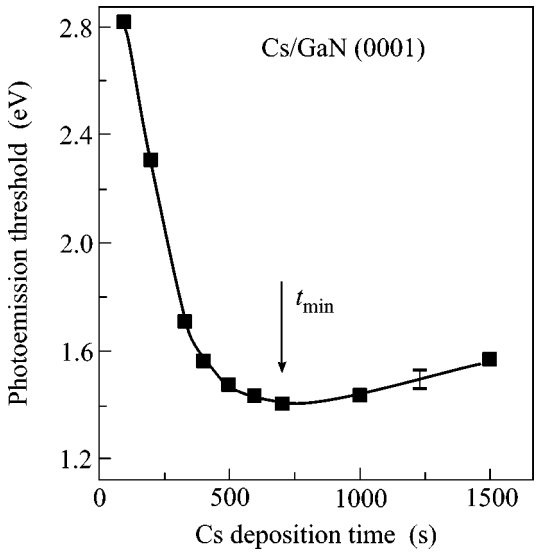

Fig. 1. Variation of the photoemission threshold $h\nu_s = \varphi$ as a function of the time of Cs evaporating onto the *n*-type GaN(0001) surface.

was determined for the first time. This result allows the cesium coverages to be calculated for the entire range with regard to the fact that the sticking coefficient of Cs remains unchanged within the monolayer [6]. Studying the $I_s(h\nu)$ and $I_p(h\nu)$ spectra showed that these spectra coincide up to optical constants. The equality of the photoemission thresholds $h\nu_s = h\nu_p$ was also found. The results obtained indicate that the energy region below the vacuum level by 1.4–3.2 eV contain no surface states. This fact corresponds to the data obtained previously [5, 6].

Studying the character of the spectral dependences $I_s(h\nu)$ in the entire studied range of cesium coverages demonstrated that the spectra in the vicinity of the threshold obey the Fowler–Nordheim law $I_p(h\nu) \sim (h\nu - h\nu_s)^2$. It is well known that this law is valid only for photoemission from the metal bulk and, in the case of semiconductors, for photoemission from the quasimetallic band of surface states positioned in the band gap at the Fermi level [8]. In our case, the Fowler–Nordheim law was fulfilled for the bulk photoemission $I_s(h\nu)$. Note that GaN is among wide-band-gap semiconductors with a band-gap width of 3.4 eV. Hence, photoemission upon excitation in the transparent region of GaN cannot be induced by the excitation of a valence-band electron. This is the principal distinction from the photoemission processes for all the known semiconductor photocathodes with a cesium coverage when valence-band states are excited.

Thus, it was found that photoemission for the *n*-type Cs/GaN(0001) system proceeds from quasimetallic bulk states; that is, the metallization of a near-surface region ~20 nm of the GaN(0001) sample is observed. Recall that no surface states were found in the band gap

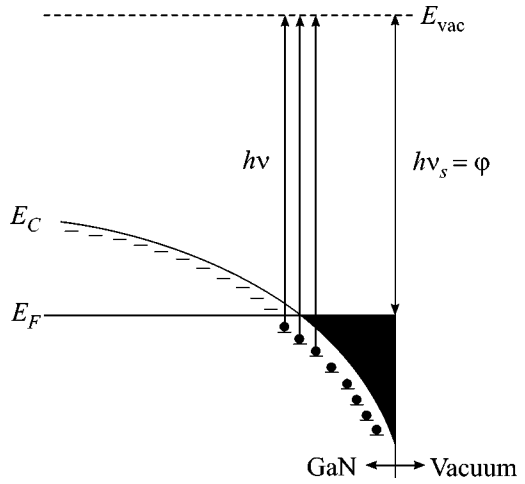

Fig. 2. Schematic diagram of the near-surface bending of the *n*-type GaN(0001) conduction band and the occurrence of a degenerate electron gas layer induced by Cs adsorption. Free and occupied polaron states are indicated. Arrows indicate optical transitions upon the excitation of photoemission.

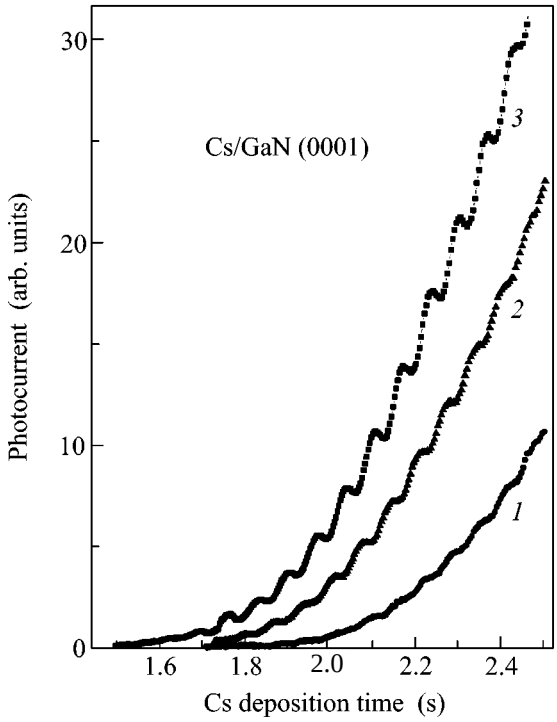

Fig. 3. Threshold photoemission spectra $I_s(h\nu)$ for various times of Cs evaporating onto the *n*-type GaN(0001) surface: (*1*) 300, (*2*) 400, and (*3*) 700 s.

for the system under study. These results as a whole can be explained by the excitation of photoemission from the conduction band in the case of the appearance of a degenerate electron gas layer when the conduction band edge at the surface lies below the Fermi level (Fig. 2). Metallization in the band-bending region provides a sharp decrease in the photoemission threshold in such a way that the excitation of electrons from the GaN conduction band by visible light from the transparent region becomes possible. In this case, the photoemission threshold corresponds to the work function $h\nu_s = \varphi$. Also note that the minimum value of the photoemission threshold obtained in this work $h\nu_s = 1.4$ eV virtually coincides with the minimum value of the work function 1.35 eV determined for *n*-type Cs/GaN(0001) at a temperature of 150 K [6]. Thus, it was stated that Cs adsorption on the *n*-type Cs/GaN(0001) surface leads to the formation of a degenerate electron gas layer in the band-bending region. For the *p*-type Cs/GaN(0001) surface, the occurrence of an analogous pattern of the modification of the electronic properties of the surface upon Cs adsorption is most apparently of little likelihood. This is evidenced by a significantly higher value of the minimum work function of ~3.5 eV for the *p*-type Cs/GaN(0001) system [5]. This fact indicates that the conventional excitation of valence-band electron states should proceed for the photoemission process in the latter case.

Figure 3 gives threshold photoemission spectra at various Cs evaporating times. The character of the spectra seems very unusual. The appearance of pronounced oscillations of the photocurrent was revealed in the spectra. It was found that the oscillation period $\Delta \sim 0.07$ eV in the spectrum is constant in energy and remains unchanged at various doses of the adsorbed cesium. It is evident that the depth of oscillations in the spectrum $I_s(h\nu)$ increases as the work function decreases. It should be emphasized that both the photoemission itself and the effect of oscillations in the photoemission spectra were observed upon excitation of the GaN sample in the transparent region. We do not know earlier facts of observing this kind of photoemission or of observing oscillations in the spectral dependences of the photoemission current.

As a possible origin of the appearance of oscillations in photoemission spectra, we will primarily consider the interference of light from the transparent region arising in the GaN slab. In this case, photoemission from the near-surface layer of a degenerate electron gas can be excited by light $h\nu \geq \varphi$, which falls both from the side of vacuum and multiply from the side of the GaN slab (Fig. 4). In this case, the observed oscillation period $\Delta \sim 0.07$ eV corresponds to an estimate made for interference in a slab 4-μm thick with regard to the refraction index $n = 2.32$ in the region of GaN excitation used in this work. However, two essential facts find no explanation in this approach. First, it was found that the photoemission currents upon light excitation in the transparent region exhibit an unexpectedly high intensity, comparable, for example, to the photoemission from Cs/GaAs(100), given the equality of the work function. Second, an abnormally high amplitude of oscillations is observed, which is comparable with

the photoemission intensity in the vicinity of the threshold. These facts require invoking an additional mechanism.

Consider the appearance of oscillations in photoemission spectra as a result of a certain resonance effect. Namely, let us suggest a combined action of classical interference in the scheme of light reflections from the plane-parallel surfaces of the sample on the one hand and Stokes Raman scattering (SRS) at such reflections, on the other (Fig. 4). We will assume the occurrence of resonance electron SRS with the absorption of light in the infrared range by well-defined electron levels with an energy gap δ close to the oscillation period $\delta \sim \Delta$. Here, the nature of levels that must lie in the near-surface band-bending region is an important factor. Note that the oscillation period $\Delta \sim 0.07$ eV turns out to be in a good correspondence with the range of vibronic frequencies. We will consider the difference between the energies of the excited and ground vibronic states of a small polaron localized in the near-surface band-bending region. In this case, it may be believed that the conduction band bending at the surface proceeds as the energy decreases for both electrons and electronic polarons. As a result of such band bending, the concentration of electronic and polaronic states in the near-surface region significantly increases because of the directed transport of Bloch current carriers and small polarons to the semiconductor surface (Fig. 2). This process leads to an enhancement of the photoemission current from the near-surface region. Moreover, polarons localized in the near-surface band-bending region will be excited upon multiple light reflections (Fig. 4) under conditions of resonance electron SRS within the framework of the Franck–Condon principle. Here, a quasiresonance (with respect to interference peaks) decrease in the light frequency occurs at each successive light reflection from the actual surface. The exciting light intensity turns out to be sufficient for the process to proceed just because of resonance electron SRS by polaron states, which has a significant probability. The SRS process itself phenomenologically corresponds to its purely vibrational analogue [10]. Delocalized excited states of the polaron band can be considered as intermediate polaron states in the SRS process. The effective matrix element of SRS in this case exhibits a very weak spectral dependence. As a result of the combined effect of multiple-beam light interference and resonance electron SRS with the excitation of well-localized polarons into the band of delocalized excited polaron states with an excitation energy $\delta \sim \Delta$, an substantial increase in the amplitude of oscillations in the photoemission spectra can be expected.

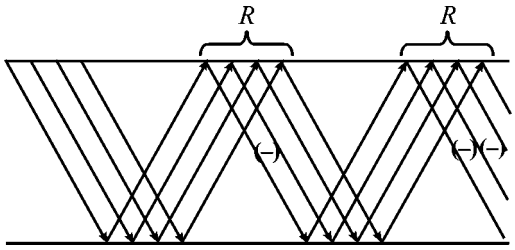

Fig. 4. Schematic diagram of light reflections in a GaN slab and Raman scattering (*R*) upon reflection from the slab surface. The sign (–) indicates single Raman scattering, the sign (–) (–) indicates double Raman scattering, etc., with the absorption of the corresponding number of polaron energy quanta.

This work was supported by the Russian Foundation for Basic Research (project no. 01-02-16802) and the program "Creation and Investigation of Atomic Structures" of the Ministry of Industry, Science, and Technology of the Russian Federation (project no. 1-1152).

REFERENCES

1. M. Razeghi and A. Rogalski, J. Appl. Phys. **79**, 7433 (1996).
2. S. J. Pearton, J. C. Zolper, R. J. Shul, *et al.*, J. Appl. Phys. **86**, 1 (1999).
3. F. Machuca, Y. Sun, Z. Liu, *et al.*, J. Vac. Sci. Technol. B **18**, 3042 (2000).
4. M. Eyckeler, W. Mönch, T. U. Kampen, *et al.*, J. Vac. Sci. Technol. B **16**, 2224 (1998).
5. C. I. Wu and A. Kahn, J. Appl. Phys. **86**, 3209 (1999); Appl. Surf. Sci. **162–163**, 250 (2000).
6. T. U. Kampen, M. Eyckeler, and W. Mönch, Appl. Surf. Sci. **123/124**, 28 (1998).
7. G. V. Benemanskaya, D. V. Daineka, and G. E. Frank-Kamenetskaya, Surf. Rev. Lett. **5**, 91 (1998).
8. G. V. Benemanskaya, D. V. Daĭneka, and G. É. Frank-Kamenetskaya, Zh. Éksp. Teor. Fiz. **119**, 342 (2001) [JETP **92**, 297 (2001)].
9. A. Liebsch, G. V. Benemanskaya, and M. N. Lapushkin, Surf. Sci. **302**, 303 (1994).
10. *Light Scattering in Solids*, Ed. by M. Cardona (Springer, Berlin, 1975; Mir, Moscow, 1979), Vol. 1.

Translated by A. Bagatur'yants

JETP Letters, Vol. 77, No. 5, 2003, pp. 230–235. Translated from Pis'ma v Zhurnal Éksperimental'noĭ i Teoreticheskoĭ Fiziki, Vol. 77, No. 5, 2003, pp. 275–280.

Magnetic Polarons, Clusters, and Their Effect on the Electric Properties of Weakly Doped Lanthanum Manganites

N. I. Solin*, V. V. Mashkautsan*, A. V. Korolev*, N. N. Loshkareva*, and L. Pinsard**

** Institute of Metal Physics, Ural Division, Russian Academy of Sciences, Russia*

e-mail: suhorukov@imp.uran.ru

*** Laboratoire de Physico-Chimie de l'Etat Solide, Universite' Paris-Sud, France*

Received January 10, 2003; in final form, February 3, 2003

The resistivity, magnetoresistance, thermopower, and magnetic susceptibility of $La_{1-x}A_xMnO_3$ (A ≡ Ca, Sr; x = 0.07–0.1) single crystals are investigated in the temperature range from 77 to 400 K. Sharp changes in the properties (the resistivity activation energy ΔE_ρ, its temperature coefficient γ, the thermopower activation energy ΔE_S, the magnetoresistance, and the appearance of spontaneous magnetization) of these crystals occur near a temperature of 275 ± 25 K, which is approximately twice as high as their Curie point T_C and approximately half of the structural transition temperature. The results are explained by the phase separation: the formation of ferromagnetic clusters. The phase separation occurs through the coalescence of small-radius unsaturated magnetic polarons, in which only two or three magnetic moments of Mn are polarized, into a large-radius ferromagnetic polaron (a cluster about 10–12 Å in size) with several charge carriers. As a result, the short-range order occurs in the cluster at a temperature of about 275 K, which is close to T_C of conducting doped manganites. The results of the experimental studies of the resistivity and the magnetoresistance as functions of temperature and magnetic field and the estimates agree well with the cluster model. *© 2003 MAIK "Nauka/Interperiodica".*

PACS numbers: 71.38.-k; 72.15.Gd; 75.47.Lx; 75.30.-m

Determination of the mechanisms of electrical conduction and the nature of magnetoresistance in lanthanum manganites is one of the most interesting problems of today's physics because of the strong interactions that occur between the electron, spin, and phonon subsystems of these substances and give rise to the complex structure of their phase diagrams [1]. The electric properties of manganites were discussed in the literature in terms of the polaron mechanism caused by the strong electron–phonon coupling [2] and in terms of the double exchange with a charge carrier localization by spin disorder [3, 4].

Recent investigations showed [5–7] that the properties of manganites can also be explained [8–10] within the framework of the phase-separation model [1]. This model assumes that, due to energy gain, an electron tends to form a conducting ferromagnetic cluster in the antiferromagnetic matrix with the size of the cluster being about several lattice constants, while in ferromagnets, clusters can exist somewhat above the Curie point [10]. For conducting ferromagnetic manganites, the qualitative relation between the presence of magnetic clusters about 12 Å in size and the magnetoresistance somewhat above the Curie point was demonstrated in [6].

The phase separation should manifest itself most clearly in the properties of weakly doped manganites. For lanthanum manganite single crystals with the composition $La_{1-x}A_xMnO_3$ (A ≡ Ca, Sr; x = 0–0.2), neutron studies revealed the presence of magnetic droplets of size ≈14–17 Å in the antiferromagnetic matrix at x = 0.05–0.1 [7, 11]. The transition from the antiferromagnetic to ferromagnetic state upon the Ca and Sr doping of manganites was explained by the changes in the exchange coupling between magnetic moments, as well as by the changes in the size, concentration, and shape of isolated clusters and by their coalescence [12, 13]. By now, the electric properties of such manganites are poorly understood, and no conclusions can be made about the effect of phase separation on the electric properties and the colossal magnetoresistance of manganites.

The determination of the mechanisms that govern the resistivity and magnetoresistance of manganites, their evolution with varying doping, and the comparison of the experimental results with the cluster model should give better insight into the effect of phase separation on the electric phenomena in these materials. For this purpose, we studied the resistivity, magnetoresistance, thermopower, and magnetic susceptibility of $La_{1-x}A_xMnO_3$ (A ≡ Ca, Sr; x = 0.07–0.1) in the temperature range within 77–400 K. We observed abrupt changes in the electric properties (the activation energies of resistivity ΔE_ρ and thermopower, the temperature coefficient of ΔE_ρ, and the magnetoresistance) and the appearance of a spontaneous magnetization near the temperature $T \approx 275$ K, which is two times as high as the Curie and Néel temperatures $T_C \approx T_N \approx$ 125–135 K

and much lower than the structural transition temperature $T_{OO'}$ = 580–450 K [12] of the samples.

The results are explained in terms of the small-scale phase separation model. It is assumed that, in weakly doped manganites, the ferromagnetic polarons of a large radius (clusters and droplets) are formed through the coalescence of small-radius polarons and contain several electrons (their number is the number of polarons in the cluster) rather than one. Therefore, the short-range order occurs in the cluster at a temperature of about 275 K, which is close to T_C of the conducting doped manganites. The results obtained by studying the resistivity and magnetoresistance as functions of temperature and magnetic field and the estimates agree well with the cluster model.

Below, we present the experimental results that for the most part refer to the $La_{0.92}Ca_{0.08}MnO_3$ single crystal grown by the floating zone method at the Laboratory of the Chemistry of Solids of the Paris-Sud University. The sample was a canted antiferromagnet with the canting angle $\theta \approx 13°$, the Curie temperature T_C = 126 K, the Néel temperature T_N = 122 K, the ferromagnetic exchange J_1 = 1 meV in a layer, and the antiferromagnetic exchange J_2 = –0.28 meV between the layers [13].

The dc resistivity measurements were performed by the standard four-probe method. The magnetic measurements were performed by an MPMS-5XL SQUID magnetometer. The e.m.f. was measured with a temperature difference of about 2 K between the sample ends.

EXPERIMENTAL RESULTS

The temperature dependence of the magnetic susceptibility χ_o of $La_{0.92}Ca_{0.08}MnO_3$ in the paramagnetic temperature region, from 300 to 350 K, is described by the Curie–Weiss law with the effective moment $\mu_{eff} \approx 5.52\mu_B$ exceeding the theoretical value $\mu_{eff} \approx 4.84\mu_B$ (μ_B is the Bohr magneton). The ferromagnetic Curie temperature determined by the peak of the initial magnetic susceptibility in zero magnetic field is $T_C = 128 \pm 1$ K, which agrees well with the results of neutron studies [13]. The differential magnetic susceptibility χ_{ac} measured at a frequency of 80 Hz does not depend on magnetic field at temperatures above 270 K, while below 270 K it drastically decreases in weak magnetic fields $H_0 \approx 100$ Oe and remains almost constant in stronger fields (Fig. 1). Such a behavior of χ_{ac} testifies to the appearance of a spontaneous magnetization and, as a rule, is observed when magnetic particles are introduced into a paramagnetic medium [14].

A higher value of μ_{eff} was obtained for a $La_{0.93}Sr_{0.07}MnO_3$ single crystal in the paramagnetic region in our previous experiment [15]. For a $La_{0.93}Sr_{0.07}MnO_3$ sample, we observed dependences $\chi_{ac}(H)$ similar to those shown in Fig. 1 along with the appearance of a spontaneous magnetization below 290–300 K.

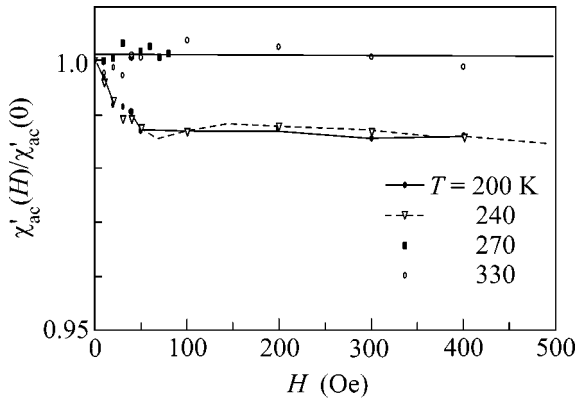

Fig. 1. Dependence of the relative low-frequency magnetic susceptibility $\chi_{ac}(H)\chi_{ac}(H = 0)$ of a $La_{0.92}Ca_{0.08}MnO_3$ single crystal on the magnetic field strength for T = 200, 240, 270, and 330 K; the frequency is 80 Hz.

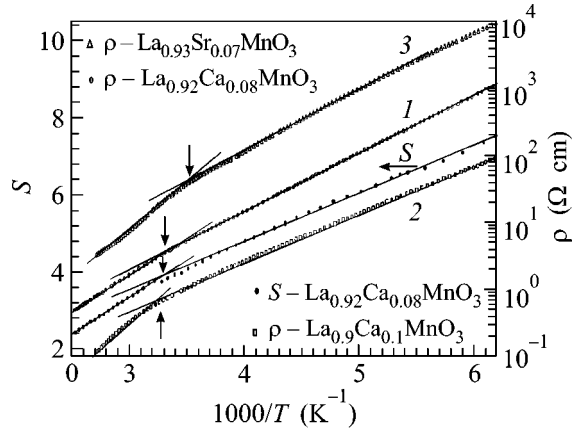

Fig. 2. Temperature dependences of the thermopower (S in k/e units) of a $La_{0.92}Ca_{0.08}MnO_3$ single crystal and the resistivity of (*1*) $La_{0.92}Ca_{0.08}MnO_3$, (*2*) $La_{0.9}Ca_{0.1}MnO_3$, and (*3*) $La_{0.93}Sr_{0.07}MnO_3$ single crystals. For clarity, the resistivity values for $La_{0.93}Sr_{0.07}MnO_3$ are increased by a factor of ten (curve *3*).

According to the measurements of the thermopower, the $La_{0.92}Ca_{0.08}MnO_3$ single crystal is a *p*-type semiconductor. The temperature dependence of the thermopower (curve *S* in Fig. 2) can be described by the activation formula characteristic of semiconductors [16]:

$$S = k/e(\Delta E_S/kT + S_0), \quad (1)$$

where e is the electron charge and k is the Boltzmann constant. Near $T \approx 280$–300 K, below which the spontaneous magnetization appears (Fig. 1), the thermopower activation energy ΔE_S and the coefficient S_0, which usually characterizes the charge carrier scatter-

Activation energies of the resistivity ΔE_ρ, thermopower ΔE_S, and hopping W_1, the temperature coefficient of the conductivity activation energy γ, and the values of the minimal metallic conductivity σ^0 and σ_{min} for a $La_{0.92}Ca_{0.08}MnO_3$ single crystal

T, K	ΔE_ρ, meV	ΔE_S, meV	W_1, meV	γ, meV/K	σ^0, Ω^{-1} cm^{-1}	σ_{min}, Ω^{-1} cm^{-1}
$400 > T > 300$	223	162	61	0.30	1350	45
$270 > T > 165$	170	113	57	0.12	200	50
$130 > T > 90$	167	–	–	–	180	–

ing, exhibit jumps: ΔE_S jumps from 162 to 113 meV, and S_0, from –2.4 to –0.4. Note that negative values $S_0 \approx -0.5$, which are noncharacteristic of semiconductors, were also observed for lanthanum manganites by other researchers [17].

The temperature dependence of the resistivity ρ of the $La_{0.92}Ca_{0.08}MnO_3$ single crystal exhibits an activation behavior and, in a wide range of variation of the quantity ρ over more than seven orders of magnitude (part of the results is shown on curve *1* in Fig. 2), is adequately described by the expression

$$\rho(T) = (1/\sigma^0)\exp(\Delta E_\rho/kT) = (1/\sigma^0)\exp[(\Delta E_S + W_1)/kT], \quad (2)$$

where W_1 is the hopping activation energy. As the temperature decreases, in the same temperature region T = 270–300 K (the inflection points of ρ and S are shown in Fig. 2 by vertical arrows), the resistivity activation energy ΔE_ρ and the pre-exponential value of the conductivity σ^0 extrapolated to $1/T \longrightarrow 0$ exhibit jumps: ΔE_ρ jumps from 223 to 170 meV, and σ^0, from 1350 to 200 Ω^{-1} cm^{-1}. At the same time, the hopping activation energy varies insignificantly (see table). Below T_N = 122 K, the values of ΔE_ρ and σ^0 vary only slightly. A small resistivity dip is observed in the exponential dependence $\rho(1/T)$ in the region $T = T_C \pm 5$ K. Below $T \approx 270$ K, the values of ΔE_ρ decrease steeply also for the $La_{0.9}Ca_{0.1}MnO_3$ and $La_{0.93}Sr_{0.07}MnO_3$ single crystals (curves *2* and *3* in Fig. 2).

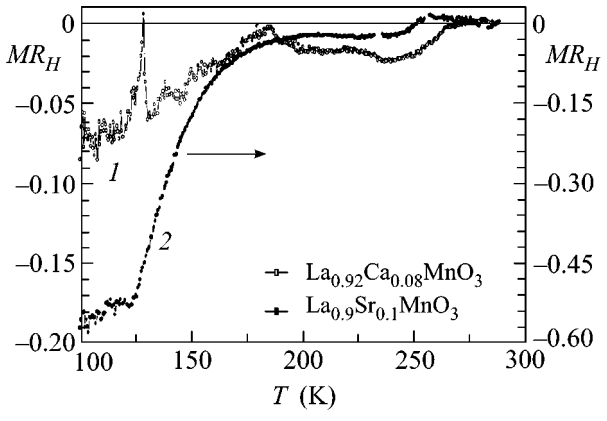

Fig. 3. Temperature dependences of the magnetoresistance of (*1*, left scale) $La_{0.92}Ca_{0.08}MnO_3$ and (*2*, right scale) $La_{0.93}Sr_{0.07}MnO_3$ single crystals.

The dc magnetoresistance of the $La_{0.92}Ca_{0.08}MnO_3$ single crystal, $MR_H \equiv [\rho(H) - \rho(H = 0)]/\rho(H)$ (curve *1* in Fig. 3), is small at room temperature: $MR_H = -0.12\%$ at H = 1.7 kOe and $MR_H \sim H^2$. It sharply increases below $T \approx 270$ K to the values $MR_H \approx -(2.0 \pm 0.5)\%$ in the temperature range 250–170 K. Below 170 K, $|MR_H|$ increases up to $MR_H \approx -10\%$ near 100 K and has a sharp dip in a narrow temperature interval of ± 5 K with a minimum at $T \approx 128$ K = T_C. A similar temperature dependence of magnetoresistance with *MR* increasing below 260 K but without a dip near T_C is observed for the $La_{0.93}Sr_{0.07}MnO_3$ single crystal (curve *2* in Fig. 3) [18].

DISCUSSION

The small conductivity of the samples observed for the acceptor concentrations below the percolation threshold $x < x_c \approx 0.16$ can be explained by the fact that the charge carriers are either captured by the localized states on the tails of the valence band or localized by a Mn^{+4} ion with the resulting polaron formation. Both mechanisms may cause an activation behavior of the resistivity and the thermopower in some temperature region, so that this behavior will be described by Eqs. (1) and (2) with different values of the activation energy [16].

The negative value of S_0 observed for the activation behavior of the resistivity and thermopower as functions of temperature shows that the activation energy $\Delta E_S = E_F - E_V$ is a linear function of temperature [16] (e.g., owing to a change in the lattice constant [19]):

$$\Delta E_S(T) = E_F - E_V = \Delta E_S - \gamma T, \quad (3)$$

where E_F and E_V are the Fermi energy and the valence band bottom energy, and γ is the temperature coefficient of the conductivity activation energy. As a result, the experimental values of the minimal metallic conductivity σ_{min} prove to be overestimated by the value of $\exp(\gamma/k)$, while the values of S_0 ($S_0 \approx 1$ for a disordered medium [16]) are underestimated: $S_0 = -\gamma/k + 1$. From the table, one can see that the quantity γ exhibits a jump near 270 K, and the value of $\sigma_{min} = \sigma^0/\exp(\gamma/k)$ remains almost constant. One can expect that the jump in γ cor-

responds to a change in the coefficient of thermal expansion near $T \approx 270$ K.

For the conduction mechanism on the valence band tails, the value of W_1 usually decreases with decreasing temperature, and the typical values of the minimal conductivity are $\sigma_{min} \leq 10\ \Omega^{-1}\ cm^{-1}$ [16]. Thus, the independence of W_1 and σ_{min} of temperature, the values $\sigma_{min} \approx 50\ \Omega^{-1}\ cm^{-1}$, and the activation behavior of the resistivity and the thermopower testify to a hopping polaron conduction in $La_{0.92}Ca_{0.08}MnO_3$ single crystals in the temperature range from 400 to 150 K.

In manganites, in the paramagnetic region, polarons can be formed owing to the strong electron–phonon coupling caused by the Jahn–Teller lattice distortion [2]. The interaction of a charge carrier with magnetic moments reduces the energy in the case of the parallel orientation of their moments, which gives rise to the formation of a "ferromagnetic" region around the charge carrier, i.e., to the formation of a magnetic polaron. Such autolocalized states may be formed in both antiferromagnetic [20] and paramagnetic [10, 21–23] states. As a result, the effective moment of paramagnetic susceptibility becomes greater than the corresponding moments of the Mn^{3+} and Mn^{4+} ions [3]:

$$S_{eff}^2 = x(S_1 + PS_2)(S_1 + PS_2 + 1) + (1 - x - Px)S_2(S_2 + 1), \quad (4)$$

where x is the concentration of spins with the moment S_1 and P is the number of polarized spins with the moment S_2.

The higher value $\mu_{eff} = 5.52\mu_B$ means that, at $T \approx$ 300–350 K, one electron per Mn^{4+} polarizes approximately two Mn^{3+} ions ($P = 2.13$) out of the six Mn^{3+} ions in its nearest environment. Since all Mn^{3+} ions are equivalent, the polarized state is evidently spread between them, thus forming a molecule with a moment of ≈ 10–$12\mu_B$ and with the polaron radius $R_{pol} = R_{Mn-Mn} = 1a \approx 4$ Å (a is the lattice constant). The estimates [3] for manganites also yield the polarization of two or three Mn^{3+} ions at room temperature. The increase in the size of "thermal" ferrons with decreasing temperature because of the weak temperature dependence $R_{pol} \sim T^{-1/5}$ [10, 22, 23] cannot account for the appearance of ferromagnetic clusters near 270 K (Fig. 1).

However, these estimates did not take into account the Jahn–Teller character of Mn^{3+} ions and the strong interaction of the electron and lattice subsystems in manganites. The appearance of magnetic polarons is known to cause considerable elastic stresses in the lattice. This is evidenced by the abrupt changes in the volumetric [6] and linear expansion coefficients of manganites [24] at the transition from ferromagnetic to magnetic polaron states. We believe that, in the case of a weak doping ($x < x_c = 1/3$), these stresses can be reduced at the temperature $T \approx$ 250–300 K, which is approximately equal to T_C of conducting manganites with $x \approx 0.2$–0.3, as a result of the coalescence of small magnetic polarons into greater conducting clusters with a ferromagnetic ordering in them. This process should be accompanied by a change in the linear expansion coefficient. The change in the lattice constant gives rise to a change in the conductivity activation energy ΔE_S and its temperature coefficient γ (see table).

Changes in the cluster size are evident from the values of ΔE_S. The hole concentration in a sample with small polarons is determined by the well-known expressions for weakly compensated impurity semiconductors containing both acceptors and donors [25]:

$$p \sim T^{3/2} \exp(-\Delta E_S/kT), \quad \Delta E_S = E_{pol}. \quad (5)$$

The polaron ionization energy E_{pol} consists of the Coulomb polarization energy [16, 25]

$$W_p \approx e^2/2\varepsilon_p' R_{pol} \quad (6)$$

and the magnetic part of the potential barrier between a ferromagnetic droplet and the paramagnetic matrix of the manganite. The estimates $W_p \approx 200$ meV obtained with the effective dielectric constant [16, 25] $\varepsilon_p' = 10$ and the polaron radius $R_{pol} = 4$ Å agree well with the experimental value of ΔE_S. The coalescence of polarons into a ferromagnetic cluster leads to an increase in the magnetic part and a decrease in the Coulomb part of the ionization energy. A decrease by a factor of ≈1.5 in the activation energy ΔE_S below 270 K (see table) corresponds to an increase in R_{pol} to $1.5a$ and to the coalescence (in the spherical model) of no less than $n_{pol}^{kl} = 4\pi/3(1.5)^3 \approx 12$–$14$ polarons into one cluster ≈10–12 Å in diameter. The inclusion of the magnetic contribution E_{pol} can only increase the number of polarons in a cluster.

The hopping activation energy W_1, which characterizes the mobility of charge carriers $\mu \sim 1/T\exp(-W_1/kT)$, is determined by the Coulomb energy [10, 16, 25] and should be expected to decrease with the cluster formation. However, it varies with temperature only slightly (see table). According to [16, 25], this energy is expressed as $W_1 = 1/2W_p(1 - R_{pol}/R_{hop})$ and depends on the hopping distance between polarons R_{hop} because of the overlapping of the wave functions of the wells. In the temperature region $T > 270$ K, we have $R_{hop} = a(x)^{-1/3} \approx 2.3a$ for $x = 0.08$ and $W_1 \approx W_p/3$. The transformation of polarons into clusters leads to their repulsion, to an increase in the distance between them, and to a change in W_1 up to $W_p/2$. These processes can explain the weak variation of W_1 below 250 K in the course of the transformation of polarons into clusters in a $La_{0.92}Ca_{0.08}MnO_3$ single crystal. From the table, one can see that, in this case, we have $W_1 \approx \Delta E_S/2$.

The studies of magnetoresistance also testify to the magnetic cluster mechanism of the electrical resistance of these samples. In manganites with the phase separation, the source of magnetoresistance is the variation of R_{pol} and the corresponding variation of the Coulomb energy W in magnetic field [10]. At the temperatures $T > 270$ K, the magnetization of polarons occurs at the expense of the turns of the magnetic moments of Mn^{3+}, and, up to very high magnetic fields, the polaron size will be independent of magnetic field: $R_{pol}(H) = 1a$ and $MR_{pol} = 0$. The magnetoresistance $MR \sim H^2 \approx 10^{-3}$ observed at 297 K is associated with the decrease in the scattering from magnetic inhomogeneities.

To estimate the magnetoresistance of clusters, we use the results of calculations for $R_{pol}(H)$ and $MR_H = 1 - \exp(W_p bH/2kT)$ [10, 23]. In the antiferromagnetic state, we have $b \equiv b^{AF} = gS\mu_B/5I_{ff}Sz$ [23]. In the paramagnetic state for $T > T_N$, from [22, 23] we obtain $b \equiv b^{PM} = gS\mu_B/5kT\ln(2S + 1)$. Here, $g = 2$ is the giromagnetic ratio, I_{ff} is the antiferromagnetic exchange between the local spins at neighboring sites, and z is the number of nearest neighbors. Then, for the antiferromagnetic and paramagnetic regions, the magnetoresistance (for small MR) is expressed as

$$MR_H^{AF} = 1 - \exp(W_p b^{AF} H/2kT) \sim H/T, \quad (7)$$

$$MR_H^{PM} = 1 - \exp(W_p b^{PM} H/2kT) \sim H/T^2. \quad (8)$$

The analysis of the results obtained by studying $MR(H)$ for a $La_{0.93}Sr_{0.07}MnO_3$ single crystal [18] shows that we have $MR_H \sim H$ in the temperature range $T < T_C = 128$ K and $MR_H \sim H^2$ near T_C. In our model, the mobility and concentration of holes are determined by the Coulomb energy. This agrees well with the conclusion [18] that, in $La_{0.93}Sr_{0.07}MnO_3$, the magnetoresistance is determined by the changes in both mobility and concentration of holes. Hence, in estimating MR_H by Eqs. (7) and (8), the value of $W_p/2$ should be replaced by the experimental value of ΔE_ρ. The estimates for $La_{0.92}Ca_{0.08}MnO_3$ and $La_{0.93}Sr_{0.07}MnO_3$ yield $MR_H^{PM} \approx$ 2–3% and $MR_H^{AF} \approx 15$ and 35% when $I_{ff} \approx I_2 = -0.3$ meV [12, 13].

The clusters may also account for the absence of magnetoresistance (the sharp dip in MR) at T_C in $La_{0.92}Ca_{0.08}MnO_3$ (Fig. 3). For this sample, the Curie point is $T_C = 128$ K $> T_N = 122$ K [13]. In the corresponding narrow temperature interval where the ferromagnetic state exists, the magnetic part of the potential barrier between the cluster and the matrix vanishes, and the resistivity slightly decreases at $T \approx T_C$ while the cluster radius R_{cl} does not depend on magnetic field, and, hence, $MR \approx 0$.

Thus, the nuclei of conducting ferromagnetic manganites exist near room temperatures in weakly doped manganites and are the source of magnetoresistance of these materials. The behavior of the resistivity and magnetoresistance of weakly doped manganites as functions of temperature and magnetic field and the estimates agree well with the phase separation model [1].

In closing, we note that the model adequately explains such results of neutron studies as the low concentration of magnetic droplets, which is 25 times smaller than the acceptor concentration [11], and the increase in the cluster size in magnetic field with a simultaneous decrease in the number of clusters [6]. In the model under discussion, the concentration of clusters $N_{cl} = N_{pol}/n_{pol}^{cl}$ is smaller than the number of polarons $N_{pol} = xa^{-3}$, where $n_{pol}^{cl} = 4\pi/3(R_{pol}/a)^3$ is the number of polarons in a cluster. From the relation $R_{pol} \approx 2a$ for $La_{1-x}Ca_xMnO_3$ [7] or the volume of 2D clusters in $La_{0.94}Sr_{0.06}MnO_3$ [11], it follows that $n_{pol}^{cl} \approx 30$, and the concentration of clusters proves to be 30 times smaller than the acceptor concentration.

We are grateful to M. Hennion for fruitful cooperation. The work was supported by the Russian Foundation for Basic Research (project nos. 02-02-16429 and 01-02-96403) and by the Ministry of Science and Technology (contract no. 40.012.1.1.1153).

REFERENCES

1. É. L. Nagaev, Usp. Fiz. Nauk **166**, 833 (1996) [Phys. Usp. **39**, 781 (1996)].
2. A. J. Millis, P. B. Littlewood, and B. I. Shraiman, Phys. Rev. Lett. **74**, 5144 (1995).
3. C. M. Varma, Phys. Rev. B **54**, 7328 (1996).
4. L. Sheng, D. Y. Xing, D. N. Sheng, and C. S. Ting, Phys. Rev. Lett. **79**, 1710 (1997); Phys. Rev. B **56**, R7053 (1997).
5. R. M. Kusters, J. Singleton, D. A. Keen, *et al.*, Physica B (Amsterdam) **155**, 362 (1989).
6. J. M. De Teresa, M. R. Ibarra, P. A. Algarabel, *et al.*, Nature **386**, 256 (1997).
7. M. Hennion, F. Mussa, G. Biotteau, *et al.*, Phys. Rev. Lett. **81**, 1957 (1998).
8. A. Moreo, S. Yunoki, and E. Dagotto, Science **283**, 2034 (1999).
9. Yu. A. Izyumov and Yu. I. Skryabin, Usp. Fiz. Nauk **171**, 121 (2001) [Phys. Usp. **44**, 109 (2001)].
10. M. Yu. Kagan and K. I. Kugel', Usp. Fiz. Nauk **171**, 577 (2001) [Phys. Usp. **44**, 553 (2001)].
11. M. Hennion, F. Mussa, G. Biotteau, *et al.*, Phys. Rev. B **61**, 9513 (2000).
12. G. Biotteau, M. Hennion, F. Mussa, *et al.*, Phys. Rev. B **64**, 104421 (2001).
13. F. Mussa, M. Hennion, G. Biotteau, *et al.*, Phys. Rev. B **60**, 12299 (1999).
14. C. P. Bean and J. D. Divingston, J. Appl. Phys. **30S**, 120 (1959).

15. N. N. Loshkareva, A. V. Korolev, T. I. Arbuzova, *et al.*, Fiz. Tverd. Tela (St. Petersburg) **44**, 1827 (2002) [Phys. Solid State **44**, 1916 (2002)].
16. N. F. Mott and E. A. Davis, *Electronic Processes in Non-Crystalline Materials*, 2nd ed. (Clarendon Press, Oxford, 1979; Mir, Moscow, 1982).
17. M. Jaime, M. B. Salamon, K. Pettit, *et al.*, Appl. Phys. Lett. **68**, 1576 (1996); Guo-meng Zhao, Y. S. Wang, D. J. Kang, *et al.*, Phys. Rev. B **62**, R11949 (2000).
18. N. I. Solin and S. V. Naumov, Fiz. Tverd. Tela (St. Petersburg) **45**, 460 (2003) [Phys. Solid State **45**, 486 (2003)].
19. H. Y. Fan, Phys. Rev. **78**, 808 (1950).
20. É. L. Nagaev, Pis'ma Zh. Éksp. Teor. Fiz. **6**, 484 (1967) [JETP Lett. **6**, 18 (1967)].
21. M. A. Krivoglaz, Usp. Fiz. Nauk **111**, 617 (1973) [Sov. Phys. Usp. **16**, 856 (1973)].
22. T. Kasuya and A. Yanase, Solid State Commun. **8**, 1543 (1970).
23. A. O. Sboĭchakov, A. L. Rakhmanov, K. I. Kugel', *et al.*, Zh. Éksp. Teor. Fiz. **122**, 869 (2002) [JETP **95**, 753 (2002)].
24. L. I. Koroleva, R. V. Demin, and A. M. Balbashov, Pis'ma Zh. Éksp. Teor. Fiz. **65**, 449 (1997) [JETP Lett. **65**, 474 (1997)].
25. I. G. Austin and N. F. Mott, Adv. Phys. **18**, 41 (1969).

Translated by E. Golyamina

JETP Letters, Vol. 77, No. 5, 2003, pp. 236–239. Translated from Pis'ma v Zhurnal Éksperimental'noĭ i Teoreticheskoĭ Fiziki, Vol. 77, No. 5, 2003, pp. 281–284.

Photoconductivity of 2D Electron Systems in Magnetic Field

V. Shikin

Institute of Solid State Physics, Russian Academy of Sciences, Chernogolovka, Moscow region, 142432 Russia

Received January 24, 2003

According to recent photoconductivity measurements in 2D electron semiconductor systems in magnetic fields normal to the 2D plane, the photoconductivity as a function of magnetic field exhibits oscillations in the region of fields much weaker than those necessary for the observation of the Shubnikov–de Haas effect. In this paper, the aforementioned oscillations are interpreted as a two-dimensional analogue of magnetophoton (phonon) oscillations studied in detail by different authors on 3D samples. © *2003 MAIK "Nauka/Interperiodica".*

PACS numbers: 72.40.+w

The problem of the photoconductivity $\tilde{\sigma}$ of a 2D electron system in a normal magnetic field under high-frequency pumping was considered in the literature as early as in the 1970s [1]. Somewhat later, independently of the theory, photoconductivity was studied experimentally on inversion layers in silicon [2, 3]. These experiments revealed no extraordinary effects except for the expected photoconductivity burst in the resonance region $\Omega = \omega_c$ (Ω and ω_c are the external and cyclotron frequencies). It is only recently that some progress was achieved in studying this interesting problem.

First of all, one should note the experiments with 2D electrons over helium [4, 5]. Among other results, it was found that the positions of the peaks of the cyclotron resonance (CR) absorption and the photoconductivity stimulated by it on the magnetic field axis are not always coincident. Even more interesting results were obtained from the detailed experimental studies of the photoconductivity of 2D electron systems formed on the basis of GaAs [6–8]. In weak magnetic fields satisfying the condition $\Omega \geq \omega_c$, these experiments revealed oscillations of the conductivity $\tilde{\sigma}_{xx}(H)$ with a period governed by the parameter γ, which had nothing in common with the quantities responsible for the Shubnikov–de Haas (SdH) oscillations:

$$\gamma = \Omega/\omega_c. \tag{1}$$

Extrema of $\tilde{\sigma}_{xx}$ occur near the points

$$\gamma_j = 1, 2, 3, \ldots, j. \tag{2}$$

At the same time, the Hall conductivity exhibits a classical behavior

$$\sigma_{xy} \propto H^{-1},$$

while the SdH oscillations become visible only in relatively high magnetic fields corresponding to $\gamma < 1$.

In the first of the cited publications [6–8], the authors mention a scenario that leads to the dependence

$$\tilde{\sigma}_{xx} \propto \cos(2\pi\Omega/\omega_c)\exp(-2\pi/\Omega_c\tau). \tag{3}$$

However, in more recent publications [7, 8], this interpretation was not discussed. Thus, the unusual oscillatory behavior of $\tilde{\sigma}_{xx}(H)$ reported in [6–8] remained unidentified.

This paper refers to the publication by Ryzhiĭ [1], which offers a qualitative explanation for the new oscillations of $\tilde{\sigma}_{xx}(H)$ observed in the experiments [6–8]. It relates the oscillations to the inelastic processes that accompany the electromagnetic irradiation of the samples. As a result of these processes, the resonance absorption of the photon energy $\hbar\Omega$ becomes possible not only at the cyclotron frequency $\Omega = \omega_c$ but also at its multiple frequencies $\Omega = j\omega_c$ (j = 2, 3, …), which coincides with the experimental observations.

1. The publication by Ryzhiĭ [1] appeared on the background of intensive studies of magnetophonon oscillations. Initially, the object under discussion was the behavior of the magnetoconductivity of 3D samples in the presence of an inelastic interaction between electrons and optical phonons [9–11]. The period of these oscillations on the magnetic field axis is determined by the parameter

$$\gamma_o = \omega_o/\omega_c \tag{4}$$

with logarithmic extrema of σ_{xx} at the points

$$\gamma_o^j = 1, 2, 3, \ldots, j.$$

Here, ω_o is the optical phonon frequency. In addition to the original (as compared to the SdH case) distribution

0021-3640/03/7705-0236$24.00

along the magnetic axis, these oscillations are insensitive to the degree of degeneracy of the 3D system, they have another (as compared to SdH) temperature dependence, etc.

The magnetophonon studies are represented by several areas of research: the behavior of highly nonequilibrium electron systems in magnetic field (beginning with the papers by Elesin and Manykin [12] and Elesin [13], in which the notion of totally negative conductivity is introduced, and the first successful experiments [14], which confirm its existence), magnetic impurity resonances in the electron transport of semiconductors (see the review by Gantmakher and Zverev [15]), and the extension of the theory to the 2D case [1, 16].

The cited paper [1] considers the two-dimensionality of the electron system with taking into account photons. The role of an optical phonon plays the high-frequency pumping field, and its frequency Ω appears in place of the quantity ω_o in Eq. (4). In the case of the scattering from optical phonons, the change in the energy and "momentum" of an electron in crossed magnetic and drift electric fields is compensated by a phonon. In the photon version of the problem, when an electron is scattered from a photon Ω and a phonon (impurity), the necessary compensation occurs separately: the change in energy occurs through the photon, and the change in the momentum, through the phonon (impurity). Such a combined scattering leads to the final expression for the current that contains the contributions from multiple cyclotron transitions, which correspond to the relation

$$j\omega_c = \Omega, \quad j = 1, 2, 3, \ldots .$$

Evidently, this condition coincides with the experimental observation described by Eqs. (1) and (2).

As for the physical reason for the oscillations of the current with the period determined by Eqs. (1) and (2), the oscillating conductivity component changes its sign in the vicinity of these points [1]; i.e., as in the 3D case, portions with a totally negative conductivity appear in the current–voltage characteristic:

$$j_{xx}(\Omega) = \frac{e^2 N(\Omega) n_s}{\Omega \epsilon(\Omega)|E|\tau} \times \sum_{j=1}^{\infty} A_j(\Omega, H, l_H^2 q_j^2) q_j \exp(-l_H^2 q_j^2/2), \tag{5}$$

$$q_j = \frac{\hbar(j\omega_c - \Omega)}{eEl_H^2}, \quad eEl_H > \hbar/\tau . \tag{6}$$

Here, E is the driving electric field, $N(\Omega)$ is the effective number of photons ($N(\Omega)$ is proportional to E_{HF}^2), n_s is the average density of 2D electrons, τ is the relaxation time due to impurities, $\epsilon(\Omega)$ is the real part of the dielectric constant, l_H is the magnetic length, and $A_n(\Omega, H, l_H^2 q_j^2)$ is a slowly varying function. The relative width of conductivity peaks of different sign and the distance between two such "neighbors" is $\sim eEl_H/\hbar\omega_c$ [1].

2. In discussing the results of the cited publication [1], it is necessary to note that its most significant statement concerning the presence of the negative conductivity portions of the current–voltage characteristic needs some refinement. The smooth component of the current–voltage characteristic, on the background of which oscillations (5) take place, is not investigated. The behavior of the current–voltage characteristic at $E \longrightarrow 0$ also remains poorly understood.

The situation with $E \longrightarrow 0$ is partially elucidated below. A 2D electron system in magnetic field selectively absorbs high-frequency energy (with a period determined by Eqs. (1) and (2)) in the absence of the field E as well. This means that photoconductivity oscillations of type (1), (2) are also possible without anomalous behavior (5), (6) of the current–voltage characteristic (the absorption changes the symmetric component of the electron distribution function and, hence, the electron mobility; this scenario of the photoconductivity formation is most probable and conventional, and the first photoconductivity experiments [2, 3] were interpreted in precisely this way).

To demonstrate the properties of the photoabsorption of a 2D system in magnetic field, it is convenient to follow [11], where the 3D version of this problem was considered with reference to similar procedures used in solving other problems [17–19].

In the 2D problem, the absorption coefficient $K_2(\Omega)$ should be determined as

$$K_2 = 1 - (|R|^2 + |1 + T|^2), \quad R = T, \quad R = \sigma/(1 - \sigma), \quad \sigma = 2\pi\sigma_{xx}/c, \tag{7}$$

where σ_{xx} is the diagonal component of the 2D conductivity in magnetic field; c is the velocity of light; and R and $(1 + T)$ are the coefficients of reflection and transmission, respectively, of a plane electromagnetic wave for a 2D electron system in magnetic field. The essential part of the absorption coefficient is determined by the expression [11]

$$K_2 \propto A \nu_i \sum_f |\langle i|\tilde{H}|f\rangle|^2 \delta(E_i - E_f), \tag{8}$$

where

$$\langle i|\tilde{H}|f\rangle = \sum_\nu \frac{\langle i|H_L|\nu\rangle\langle\nu|H_R|f\rangle}{E_i - E_\nu} + \sum_\nu \frac{\langle i|H_R|\nu\rangle\langle\nu|H_L|f\rangle}{E_i - E_\nu}. \tag{9}$$

Here, H_R and H_L are the energies of the electron interaction with the high-frequency field and the lattice, respectively; the wave function $|i\rangle$ with the components

$$|i\rangle = |\alpha\ldots, n(q)\ldots, N(k)\ldots\rangle \equiv |\alpha, 0, 0\rangle$$

is a certain initial state with the characteristics α of an electron in magnetic field and with the phonon and photon occupation numbers $n(q)$ and $N(k)$; and q and k are the wave numbers of phonons and photons. Correspondingly,

$$|f\rangle = |\alpha'\ldots, N(q) \pm 1\ldots, N(k) - 1\ldots\rangle \equiv |\alpha', \pm q, -k\rangle$$

is the final state, in which the electron state changes and emission or adsorption of a phonon takes place.

In the first sum of Eq. (9), the transitions occur through the virtual states $|\nu\rangle = |\alpha'', \pm q, 0\rangle$; i.e., the number of phonons changes first, and then the number of photons. In the second sum, we have $|\nu\rangle = |\alpha'', 0, -k\rangle$, and the number of photons is the first to change, while the number of phonons is the second.

The summation over the final states in Eq. (8) means the summation with respect to α' and $\pm q$. The averaging (if required) over the initial states is denoted by $A\nu_i$ and implies thermal averaging with respect to α and $n(q)$. As a result, following [11], we obtain

$$K_2(\Omega) = K_2^+(\Omega) + K_2^-(\Omega), \tag{10}$$

where $K_2^+(\Omega)$ and $K_2^-(\Omega)$ are the contributions due to the phonon emission and adsorption to the photon absorption. These contributions are expressed as

$$K_2^{-\pm}(\Omega) = \sum_{l, l' = 0} K_{l, l'}^{\pm}(\Omega), \tag{11}$$

where

$$K_{l, l'}^{\pm}(\Omega) = A(\Omega) w_l \int_{-\infty}^{+\infty} dq q^3 \left[n_T(q) + \frac{1}{2} \pm \frac{1}{2} \right] \times B(q) |Q_{ll'}(q l_H)|^2 \delta[(l - l')\omega_c + \Omega \pm \omega(q)]; \tag{12}$$

$$A(\Omega) = \frac{1}{4}(2\pi)^3 n_s \alpha_R \frac{1}{m^2 \Omega} \left[\frac{1}{(\Omega + \omega_c)^2} + \frac{1}{(\Omega - \omega_c)^2} \right],$$

$$\alpha_R = e^2/c\sqrt{\epsilon(\Omega)},$$

$$w_l = 2\sinh(\omega_c/T)\exp[-\omega_c(l + 1/2)/T], \tag{13}$$

$$Q_{ll'}(x) = (-1)^{l - l'}(l'!/l1)^{1/2} x^{l - l'} L_{l'}^{l - l'}(x^2)\exp(-x^2/2).$$

Here, the factor $B(q)$ in Eq. (12) characterizes the electron–phonon interaction and is a smooth function of q, α_R is the electron–photon coupling constant, and T is the temperature.

The integral in Eq. (12) is taken using the delta function, which, for acoustic phonons with the dispersion law $\omega(q) \simeq Sq$ (where S is the velocity of sound along the 2D metal film), selects the necessary phonon $q = q^*$ in the integral of Eq. (12):

$$q^* = \pm[(l - l')\omega_c + \Omega]/S. \tag{14}$$

Then, the factor $Q_{ll'}$ given by Eq. (13) comes into play. For this factor (and, hence, the absorption coefficient as a whole) not to be exponentially small, the quantity q^* must be close to zero. More precisely, the following inequality must be satisfied:

$$q^* l_H < 1. \tag{15}$$

The optimal value of q^* corresponding to the maximal $Q_{ll'}$ is zero, which is equivalent to conditions (1), (2) with the only possible exception of the point $j = 1$, where, additionally, the function $A(\Omega)$ has a pole. As a result, at $j = 1$, the absorption becomes classical, i.e., takes the cyclotron character.

The sharpness of the multiple cyclotron resonances is mainly determined by the requirement imposed on the energy of the initial photon. According to expressions (14) and (15), for the appearance of such resonances with the participation of phonons, it is desirable that the following condition is satisfied:

$$\Omega \gg S/l_H. \tag{16}$$

This is achievable not only for the classical cyclotron resonance but also for the appearance of multiple cyclotron harmonics.

SUMMARY

The existing theory of magnetophoton phenomena for 2D electrons in magnetic field allows one to qualitatively explain the appearance of multiple cyclotron photoconductivity peaks determined by Eqs. (1) and (2) as a result of the inelastic processes that accompany the absorption of a photon with an energy $\Omega \gg \omega_c$ in a medium containing a 2D electron system, conditions (14) and (15) being optimal for the manifestation of these processes. The presence of the aforementioned peaks is easily determined in terms of the theory developed in [1, 9–11]. It is also possible to mention the subsequent publications [20] that point to the presence of multiple cyclotron resonances in photoabsorption. As for the amplitude of the oscillations under discussion, a systematic study aimed at the development of the 2D formalism of magnetophoton phenomena by analogy with the 3D case is necessary. An additional specific feature of the 2D situation is that the dimensionless parameter σ from Eq. (7) approaches unity for high-quality samples [6–8]. In these conditions, the oscillations of photoabsorption may considerably increase for "impedance" reasons. For illustration, one can refer to the publication [21] reporting on the observation of weakly pronounced multiple cyclotron peaks on the wings of the CR peak. However, the quality of the samples studied in [21] was considerably lower than that in

[6–8], so that the case $\sigma \ll 1$ took place and no impedance amplification was present.

I am grateful to V. Gantmakher and S. Iordanskiĭ for discussing the results of this study and for useful comments. The work was supported in part by the Russian Foundation for Basic Research, project no. 03-02-16121.

REFERENCES

1. V. Ryzhiĭ, Fiz. Tverd. Tela (Leningrad) **11**, 2577 (1969) [Sov. Phys. Solid State **11**, 2078 (1970)].
2. H. Bluyssen, J. Mann, L. Ruyven, *et al.*, Solid State Commun. **25**, 895 (1978).
3. J. Mann, T. Englert, D. Tsui, and A. Gossard, Appl. Phys. Lett. **40**, 609 (1982).
4. F. Penning, O. Tress, H. Bluyssen, and P. Wyder, J. Low Temp. Phys. **110**, 185 (1998).
5. F. Penning, O. Tress, H. Bluyssen, *et al.*, Phys. Rev. B **61**, 4530 (2000).
6. M. Zudov, R. Du, J. Simmons, and J. Reno, cond-mat/9711149 (1997).
7. M. Zudov, R. Du, J. Simmons, and J. Reno, Phys. Rev. B **64**, 201311-1 (2001).
8. M. Zudov, R. Du, L. Pfeifer, and K. West, cond-mat/0210034 v1 (2002).
9. V. Gurevich and Yu. Firsov, Zh. Éksp. Teor. Fiz. **40**, 199 (1961) [Sov. Phys. JETP **13**, 137 (1961)].
10. A. Éfros, Fiz. Tverd. Tela (Leningrad) **3**, 2848 (1961) [Sov. Phys. Solid State **3**, 2079 (1961)].
11. F. Bass and I. Levinson, Zh. Éksp. Teor. Fiz. **49**, 914 (1965) [Sov. Phys. JETP **22**, 635 (1965)].
12. V. Elesin and É. Manykin, Pis'ma Zh. Éksp. Teor. Fiz. **3**, 26 (1966) [JETP Lett. **3**, 15 (1966)].
13. V. Elesin, Pis'ma Zh. Éksp. Teor. Fiz. **7**, 229 (1968) [JETP Lett. **7**, 176 (1968)].
14. A. Aleksandrov, Yu. Bykovskiĭ, V. Elesin, *et al.*, Zh. Éksp. Teor. Fiz. **64**, 231 (1973) [Sov. Phys. JETP **37**, 120 (1973)]; Pis'ma Zh. Éksp. Teor. Fiz. **12**, 57 (1970) [JETP Lett. **12**, 41 (1970)].
15. V. Gantmakher and V. Zverev, in *Landau Level Spectroscopy*, Ed. by G. Landwehr and E. Rashba (North-Holland, Amsterdam, 1991), Chap. 19, p. 1137.
16. A. Gladun and V. Ryzhiĭ, Zh. Éksp. Teor. Fiz. **57**, 978 (1969) [Sov. Phys. JETP **30**, 534 (1970)].
17. H. Frolich, Adv. Phys. **3**, 325 (1964).
18. H. Meyer, Phys. Rev. **112**, 298 (1958).
19. R. Rosenberg and M. Lax, Phys. Rev. **112**, 843 (1958).
20. T. Audo, J. Phys. Soc. Jpn. **38**, 989 (1975).
21. J. Kotthaus, G. Abstreiter, and J. Koch, Solid State Commun. **15**, 517 (1974).

Translated by E. Golyamina

JETP Letters, Vol. 77, No. 5, 2003, pp. 240–242. Translated from Pis'ma v Zhurnal Éksperimental'noĭ i Teoreticheskoĭ Fiziki, Vol. 77, No. 5, 2003, pp. 285–287.

Order Parameter of *A*-like ^{3}He Phase in Aerogel

I. A. Fomin

Kapitza Institute for Physical Problems, Russian Academy of Sciences, ul. Kosygina 2, Moscow, 117334 Russia

Received January 30, 2003

In the framework of a phenomenological description of superfluid ^{3}He in aerogel, a criterion of choosing the form of the order parameter close to the transition is obtained. Besides the BW phase, the order parameter of the axiplanar phase with specially chosen free parameters also satisfies this criterion. Such an order parameter is proposed as limiting at $T \longrightarrow T_c$ for an *A*-like phase observed for ^{3}He in aerogel. © *2003 MAIK "Nauka/Interperiodica".*

PACS numbers: 67.57.-z

1. Two superfluid phases, *A*-like and *B*-like, are observed in liquid ^{3}He filling the free space between the filaments of aerogel. The names of the phases show the connection with superfluid *A* and *B* phases of impurity-free (pure) ^{3}He and present the existing indefiniteness in their identification. Pulsed NMR experiments [1] indicate that the order parameter in the *B*-like phase after averaging over small-scale fluctuations has a form the same as or close to that in pure ^{3}He-*B*. There is no unambiguous indication to a possible form of the order parameter in the *A*-like phase. It is known that the static magnetic susceptibility in this phase is the same as in the normal phase and the *A* phase of pure ^{3}He [2]. Therefore, pairing particles in the *A*-like phase have equal spins (ESP, equal-spin pairing); i.e., there are no Cooper pairs with zero spin projection onto the direction of magnetic field (*z* axis). In this case, the order parameter (matrix $A_{\mu j}$) can be represented in the form

$$A_{\mu j} = \hat{x}_\mu a_j + \hat{y}_\mu b_j, \quad (1)$$

where $\hat{x}_\mu$ and $\hat{y}_\mu$ are the orts of the corresponding axes in the spin space and a_j and b_j are the complex vectors in the momentum space. The *A* phase (axial) of pure ^{3}He is a particular case, and its order parameter has the form

$$A_{\mu j} = \Delta\frac{1}{\sqrt{2}}\hat{d}_\mu(\hat{m}_j + i\hat{n}_j), \quad (2)$$

i.e., involves only one spin vector $\hat{d}_\mu$ and "orbital" vectors $\hat{m}_j$ and $\hat{n}_j$ are real, normalized, and perpendicular to each other. Volovik demonstrated that matrix (2) cannot describe a phase transition in aerogel to a state with long-range order [3]. The vector $\hat{\mathbf{l}} = \hat{\mathbf{m}} + \hat{\mathbf{n}}$ randomly changes its direction. Therefore, the average $A_{\mu j}$ value is equal to zero. A transition to a superfluid-glass state [4], where the mean values of quadruples of the creation and annihilation operators for quasiparticles play the role of the order parameter, is possible. However, as will be demonstrated below, the existence of the superfluid phase with the magnetic susceptibility of normal ^{3}He can be explained with the Cooper pairing and long-range orientational order.

2. The interaction of aerogel with superfluid ^{3}He near T_c can be described phenomenologically [5] by introducing the energy density

$$f_\eta = g_\eta \eta_{jl}(\mathbf{r}) A_{\mu j} A^*_{\mu l}, \quad (3)$$

to the Ginzburg–Landau functional. Here, $\eta_{jl}(\mathbf{r})$ is the random symmetric tensor and g_η is the coupling constant. Addition (3) takes into account fluctuations in the positions of the filaments of aerogel. The functional takes the form

$$F_{\mathrm{GL}} = \int d^3r\{\alpha(T - T_c)A_{\mu j}A^*_{\mu j} + f_\eta + f_\nabla + f_4\}, \quad (4)$$

where f_∇ and f_4 are, respectively, the gradient energy and the fourth-order terms. The isotropic part of the tensor $\eta_0(\mathbf{r})\delta_{jl}$ can be included into the transition temperature T_c. After that, η_{jj}; i.e., the trace is equal to zero. Aerogel is assumed to be isotropic on average; i.e., $\langle\eta_{jl}(\mathbf{r})\rangle = 0$. The tensor $\eta_{jl}(\mathbf{r})$ physically describes splitting in T_c due to the local breaking of the spherical symmetry. The temperature T_c in pure ^{3}He is the same for all spherical harmonics with $l = 1$. For volumes exceeding ξ_0 in aerogel, the "local temperature of the transition" can generally be different for the different projections of the angular momentum. The added energy f_η is of the second order in $A_{\mu j}$ and makes the basic contribution to functional (4), when $\langle A_{\mu j}\rangle \neq 0$ in some region near T_c. The choice of $\langle A_{\mu j}\rangle$ in this region is expected to be determined by perturbation f_η. Of special interest are those combinations of the projections of the angular

0021-3640/03/7705-0240$24.00

momentum and spin that are not split by the tensor field $\eta_{jl}(\mathbf{r})$, i.e., satisfy the condition

$$\eta_{jl}A_{\mu j}A^*_{\mu l} = 0. \quad (5)$$

In this case, the energy f_η does not dominate, and those terms in functional (4) that are responsible for the phase transition become substantial. If $A_{\mu j}$ is an extremum of functional (4) and satisfies condition (5), $\partial F_{GL}/\partial g_\eta = 0$ and the change in interaction with aerogel does not affect energy. The order parameter of the B phase $A_{\mu j} = \Delta e^{i\varphi}R_{\mu j}$, where $R_{\mu j}$ is the orthogonal matrix, has this property. Indeed, the substitution of this expression into Eq. (2) yields

$$\eta_{jl}R_{\mu j}R_{\mu l} = \eta_{jl}\delta_{jl} = \eta_{jj} = 0. \quad (6)$$

Similar substitution for the axial phase provides the nonzero result $f_\eta \sim -\eta_{jn}l_jl_n$ that is responsible for the appearance of the orientational disordering. Let us seek those ESP phases [of form (1)] that, similarly to the B phase, are not split by the tensor field $\eta_{jl}(\mathbf{r})$, i.e., satisfy condition (5). We decompose the vectors **a** and **b** in definition (1) into real and imaginary parts: $\mathbf{a} = \mathbf{m} + i\mathbf{n}$, $\mathbf{b} = \mathbf{l} + i\mathbf{p}$, where **m**, **n**, **l**, and **p** are real vectors. Substituting Eq. (1) into Eq. (5), we obtain an equation whose imaginary part is identically zero due to the symmetry of η_{jl}. The real part is zero, if

$$m_jm_l + n_jn_l + l_jl_l + p_jp_l = \delta_{jl}\text{const}. \quad (7)$$

The constant on the right-hand side can be taken equal to unity. Quadruples of vectors, one of which is zero, e.g., $\mathbf{p} = 0$, and the three remaining vectors form an orthonormal triple, satisfy Eqs. (7). The corresponding desired order parameter has the form

$$A_{\mu j} = \Delta\frac{1}{\sqrt{3}}[\hat{d}_\mu(\hat{m}_j + i\hat{n}_j) + \hat{e}_\mu\hat{l}_j]. \quad (8)$$

Substitution shows that matrix (8) satisfies condition (5); i.e., "isotropic" ESP phase with this order parameter does not lose the orientational order under the action of aerogel. A matrix found from condition (5) need not coincide with one of the extrema of the free energy of pure ^{3}He [6]. Nevertheless, the isotropic ESP phase is a particular case of the axiplanar phase [7, 8] whose order parameter is proportional to

$$\begin{aligned}&(\hat{\mathbf{d}} + i\hat{\mathbf{e}})[\hat{\mathbf{m}}v_x + i(\hat{\mathbf{n}}v_y + \hat{\mathbf{l}}v_z)]\\ &+ (\hat{\mathbf{d}} - i\hat{\mathbf{e}})[\hat{\mathbf{m}}v_x + i(\hat{\mathbf{n}}v_y - \hat{\mathbf{l}}v_z)].\end{aligned} \quad (9)$$

The parameters of the axiplanar phase are a triple of real numbers v_x, v_y, and v_z related as $v_x^2 + v_y^2 + v_z^2 = 1$. The isotropic ESP phase (8) corresponds to $v_x^2 = v_y^2 = v_z^2 = 1/3$, and axial phase (2), to $v_x^2 = v_y^2 = u$ and $v_z = 0$. Both limiting cases belong to the one-parameter family $v_x = v_y = 1/2 \equiv u$, $v_z \equiv w$, and $2u^2 + w^2 = 1$ with the order parameter proportional to

$$u\hat{\mathbf{d}}(\hat{\mathbf{m}} + i\hat{\mathbf{n}}) - w\hat{\mathbf{e}}\hat{\mathbf{l}}. \quad (10)$$

For $w \neq 0$, this expression corresponds to a nonunitary phase differing from the axial phase in symmetry. In particular, the nonunitary phase does not exhibit the combined symmetry about the gauge transformation and rotation of $\hat{\mathbf{m}}$ and $\hat{\mathbf{n}}$ about $\hat{\mathbf{l}}$. For this reason, continuous vortices are absent in the axiplanar phase.

3. In the scheme proposed above, the transition at $T = T_c$ must lead either immediately to the B phase or to the symmetric ESP phase (8). In a magnetic field, phase (8) is favorable due to its larger magnetic susceptibility. As temperature decreases, the coefficients u and w in Eq. (10) can deviate from the value $u = w = 1/\sqrt{3}$. Deviations become significant at temperatures that can be estimated by considering fluctuation corrections to average $A_{\mu j}$ for temperatures far from T_c, where they can be considered as small, and by extrapolating them to the region where they become on the order of unity. For ordinary superconductors [9], this occurs at $(T_c - T)/T_c \sim (\lambda_{\text{corr}}^3/l_{\text{tr}}^2\xi_0)^2$, where λ_{corr} is the correlation length of the random field $\eta_{jl}(\mathbf{r})$, l_{tr} is the transport free path of fermion excitations, and ξ_0 is the coherence length in superfluid ^{3}He. For values $\lambda_{\text{corr}} \sim 500$ Å, $l_{\text{tr}} \sim 2000$ Å, and $\xi_0 \sim 200$ Å, we obtain $(T_c - T)/T_c \sim 1/30$. This estimate is depreciated, because it involves the sixth power of the poorly known quantity λ_{corr}. A more reliable estimate can be obtained from the observed smearing of the heat-capacity jump [10]. According to these data, $(T_c - T)/T_c \sim 1/25$. Within this temperature range near T_c, the order parameter must be close to that for the symmetric ESP phase. This range can be wider if the symmetric ESP phase is close to the minimum of functional (4) at $f_\eta = 0$ and for the f_4 form realizing in fact. There is no cause for the destruction of the long-range orientational order in the symmetric ESP phase. For $u \neq w$, energy $(w^2 - u^2)\eta_{jl}l_jl_l$ tends to destroy this order. For $|w^2 - u^2| \ll 1$, the length where the order must be destroyed according to [3] is certainly larger than the dipole length. In this case, the directions of **l** and **m** are fixed by the directions of **d** and **e**, respectively. Without comprehensive quantitative analysis, it is difficult to estimate whether a decrease in temperature leads to further disordering. An additional transition was not observed in experiments.

Possible methods of experimental observation of difference between the axiplanar and axial phases in pure ^{3}He were discussed in publications and used in [8]. All these methods are, principally, applicable to aerogel. Measurement of the orbital properties, e.g., the anisotropy of the superfluid-density tensor is a more direct method. This tensor must be isotropic in phase (8). The negative shift observed in experiments [2] for

the frequency of the transverse NMR does not exclude the suggested identification of the *A*-like phase, because a negative addition to the spin precession frequency with deviations of **d** from **l** can arise due either to longitudinal oscillations [11] or to the orientating effect of walls [12].

I am grateful to V.V. Dmitriev, V.I. Marchenko, and T.E. Panov for stimulating discussions and to the referee of the paper for useful remarks. This work was supported in part by the U.S. Civilian Research and Development Foundation for the Independent States of the Former Soviet Union (grant no. RP1-2089) and the Russian Foundation for Basic Research (project no. 01-02-16714).

REFERENCES

1. V. V. Dmitriev, V. V. Zav'yalov, D. E. Zmeev, *et al.*, Pis'ma Zh. Éksp. Teor. Fiz. **76**, 371 (2002) [JETP Lett. **76**, 312 (2002)].
2. B. I. Barker, Y. Lee, L. Polukhina, *et al.*, Phys. Rev. Lett. **85**, 2148 (2000).
3. G. E. Volovik, Pis'ma Zh. Éksp. Teor. Fiz. **63**, 281 (1996) [JETP Lett. **63**, 301 (1996)].
4. G. E. Volovik and D. E. Khmel'nitskiĭ, Pis'ma Zh. Éksp. Teor. Fiz. **40**, 469 (1984) [JETP Lett. **40**, 1299 (1984)].
5. I. A. Fomin, Pis'ma Zh. Éksp. Teor. Fiz. **75**, 220 (2002) [JETP Lett. **75**, 187 (2002)].
6. V. I. Marchenko, Zh. Éksp. Teor. Fiz. **93**, 141 (1987) [Sov. Phys. JETP **66**, 79 (1987)].
7. N. D. Mermin and G. Stare, *Materials Science Center* (Cornell Univ., 1974), Report No. 2186.
8. T. R. Mullins, V. V. Dmitriev, A. J. Armstrong, *et al.*, Phys. Rev. Lett. **72**, 4117 (1994).
9. A. I. Larkin and Yu. N. Ovchinnikov, Zh. Éksp. Teor. Fiz. **61**, 1221 (1971) [Sov. Phys. JETP **34**, 651 (1972)].
10. J. He, A. D. Corwin, J. M. Parpia, *et al.*, Phys. Rev. Lett. **89**, 115301 (2002).
11. I. A. Fomin, J. Low Temp. Phys. **31**, 509 (1978).
12. A. D. Gongadze, G. E. Gurgenishvili, and G. A. Kharadze, Zh. Éksp. Teor. Fiz. **78**, 615 (1980) [Sov. Phys. JETP **51**, 310 (1980)].

Translated by R. Tyapaev

JETP Letters, Vol. 77, No. 5, 2003, pp. 243–246. Translated from Pis'ma v Zhurnal Éksperimental'noĭ i Teoreticheskoĭ Fiziki, Vol. 77, No. 5, 2003, pp. 288–291.

Formation and Growth of the Anomalous State of ^{4}He Crystal Below 0.45 K

V. L. Tsymbalenko

Institute of Superconductivity and Solid-State Physics, Russian Research Centre Kurchatov Institute, pl. Kurchatova 1, Moscow, 123182 Russia

e-mail: VLT@isssph.kiae.ru

Received February 4, 2003

The diagram of the anomalous state of ^{4}He crystals was determined in the range 0.2–0.45 K. Agreement was obtained with the diagram of "bursteike" growth of a dislocation-free facet. This confirms previous assumption about the common nature of these phenomena. The requirements to the theoretical model of the phenomenon are formulated. The growth rate of the facets in the anomalous state was measured up to supersaturations of ~20 mbar. It was found that the growth rate becomes constant and equal to ~3.5 m/s above ~8 mbar. © *2003 MAIK "Nauka/Interperiodica"*.

PACS numbers: 67.80.-s; 81.10.-h

The anomalous state of ^{4}He crystals with an exceedingly high growth rate is formed below 0.78 K at supersaturations $Dp \sim 15$ mbar and has been studied down to a temperature of ~0.45 K [1, 2]. This temperature range lies below the first ($T_{R1} = 1.28$ K) and the second ($T_{R2} = 0.9$ K) but above the third ($T_{R3} = 0.35$ K) roughening transition [3]. Temperature lowering provides a unique possibility of revealing whether the roughening transition has an effect on the formation of the anomalous state or not. It is known from experiment [4] that the appearance of the anomalous state leads to a simultaneous increase in the growth rate of both basal and lateral facets, which are equilibrium in this temperature range, i.e., to the simultaneous transition of facets into the state with a high growth kinetics. It is unjustified to assert that this is also valid for the third roughening transition. The Miller indices of the facets formed upon this transition are $(10\bar{1}1)$. If the growth rate of these facets below T_{R3} is slow and typical of crystals in the normal state, then growth time of the crystal will increase by two to three orders of magnitude.

Earlier [5], I have suggested that the effects of the anomalous state and "bursteike" growth of a dislocation-free facet [6] have a common physical origin. This assumption was based both on the common features of the phenomena and on the similarity of the Dp^*–T diagrams of the anomalous and bursteike growths. However, there is a gap between the lowest point of my measurements (~0.45 K) and the upper point (~0.25 K) obtained in [6]. Measurements below 0.4 K will be helpful in checking the agreement between these phase diagrams.

Measurements in this temperature range provide additional information on the growth kinetics of a crystal in the anomalous state. Previously, it was found that the growth rate increased on cooling. However, the measurement interval was too small to determine the temperature dependence of surface mobility. Moreover, the growth rate decreased upon approaching the boundary of the anomalous region. This fact was supposedly associated with the state-formation kinetics rather than with the dissipative mechanisms governing the growth kinetics in the anomalous state. It is thus necessary to measure the growth rate deep inside the anomalous zone and, desirably, in the region where the critical supersaturation Dp^* of state appearance weakly depends on temperature, i.e., in the region below 0.4 K.

MEASUREMENT RESULTS

Phase diagram. The measuring technique and the container design were described in detail in [2, 5]. For this reason, only the main details of the experiment will be outlined here. A helium crystal was nucleated by a pulse of electrostatic field in the center of a cylindrical container with a volume of 1.8 cm^3. This technique allows the initial supersaturation Dp to be set in the interval from zero (phase equilibrium pressure) to the maximal value determined by the spontaneous nucleation at the inner wall of the container. The change in pressure during the growth process was measured by a capacitive transducer with a time resolution of 35 μs. A temperature of 0.48 K was achieved by evacuation of ^{3}He vapor and served as a starting point for the magnetic cooling by paramagnetic salt (chrome potash alum). Temperature was measured by a Matsushita thermometer placed inside the container in contact with superfluid helium.

0021-3640/03/7705-0243$24.00

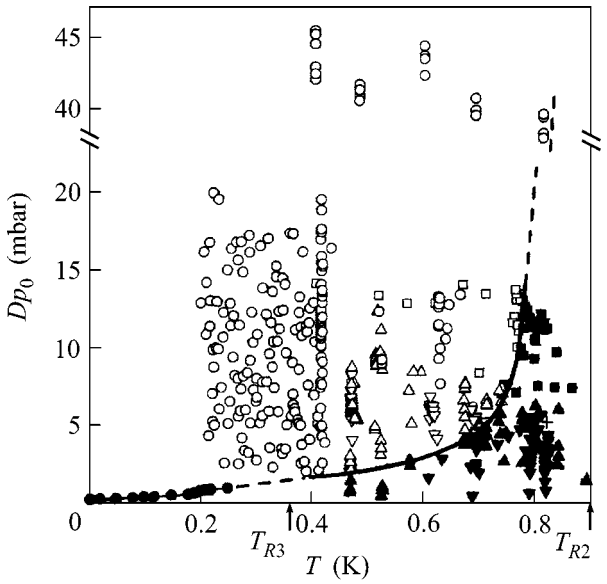

Fig. 1. Diagram of anomalous state. Light circles correspond to the fast growth and black circles are for the normal slow crystal growth. Arrows indicate the temperatures of the second and third roughening transitions.

Figure 1 presents the results of measuring the phase diagram [2], together with the additional data extended to 0.2 K. The spontaneous-nucleation threshold at the container wall was about 20 mbar, although it achieved 45 mbar in some experiments (Fig. 1). This allowed the phase diagram to be extended into the range of higher temperatures (dashed line). Unfortunately, supersaturations as high as those were not reproduced in a repeat experiment, which did not allow the phase boundary to be located more precisely, so that the dashed line in the high-saturation region represents the lower boundary of the transition.

The second result of these measurements was that no special features were observed in the phase diagram and growth kinetics at the point of third roughening transition. Therefore, the transition to the anomalous state imparts a high growth rate to the $(10\bar{1}1)$ facets.

The third conclusion is that the anomalous and bursteike growth diagrams are in agreement with each other. One can see from the graph that all the crystals formed above the line connecting these two regions demonstrate the growth with a high rate. It also should be taken into account that, as was observed experimentally in [7], the anomalous state is formed in a finite time, which decreases with increasing the initial supersaturation. In the bursteike growth experiments, this is manifested by the statistical character of state appearance [6]. In our experiments, the growth time of normal-state crystals was ≤10 ms, so that, to observe the fast-growth effect, it is necessary that the crystal undergo transition to the anomalous state within this time. In the bursteike growth experiments, the time during which the crystal facet stays under the action of an excess pressure is several orders of magnitude longer and comprises ~10 s. Hence, it follows that our experiments yield values of boundary supersaturation corresponding to the formation time 0.1–10 ms, which must be longer than the times obtained in the experiments with the slow buildup of pressure over the facet [6] (formation time ~1–10 s). With regard to this remark, both phase diagrams agree well with each other. This confirms the assumption that was made in [5] about the common nature of these phenomena. Such an identification makes the range of possible mechanisms accounting for this phenomenon even narrower. Evidently, the effects associated with the topological defects at the surface structure (assessed in [7]) should then be excluded from consideration, because the bursteike growth was observed just for the facet that was free of such defects. Likewise, the mechanisms associated with the vortices in superfluid helium [7] should also be ruled out, because the facet in experiments [6] was almost immobile before the fast-growth onset; i.e., there were no fluid flows.

One more argument in favor of the commonness of the phenomena observed in [2] and [6] is that impurities affect the phase diagram. The boundary supersaturation for the bursteike growth increases upon adding 10–50 ppm of ^{3}He impurity; i.e., the fast-growth region shifts upward [6]. Although our experiments with 180 ppm of impurities are at the initial stage, one nevertheless can state that the addition of ^{3}He in the temperature range 0.64–0.78 K also shifts the critical supersaturation Dp^* upward.

The main features of the formation of anomalous state with a high growth rate can be summarized as follows:

(i) The state arises in a finite time that decreases with a rise in supersaturation.

(ii) The formation time increases with temperature.

(iii) The critical supersaturation Dp^*, measured at a fixed formation time, increases monotonically with temperature.

(iv) The process has a statistical character.

(v) The transition brings about simultaneous change in the growth kinetics of all facets, as it was experimentally demonstrated for all three roughening transitions.

(vi) The appearance of the anomalous state is related neither to the surface topological defects nor to the vortices in fluid.

None of the existing hypotheses satisfies all these requirements.

Growth rate. Crystal growth with a high rate induces radial oscillations of a fluid in the container and leads to the oscillatory character of the growth. In [8], it was suggested that the ratio between the amplitude of the first pressure minimum and the initial supersaturation can be used for determining the average growth

kinetic coefficient K in the first 100 μs; it is defined by the expression

$$V = K\frac{\Delta\rho}{\rho\rho'}Dp,$$

where V is the growth rate of crystal surface; ρ and ρ' are the densities of liquid and solid helium, respectively; $\Delta\rho = \rho' - \rho$; and Dp is the supersaturation. It is essential that K in this method is assumed constant; i.e., the growth rate is linear in supersaturation. If this condition is not fulfilled, this technique can be used to semiquantitatively estimate the growth rate through determining the average crystal growth rate at the first half-wave, where the pressure drops from its initial value Dp_0 to zero as

$$\langle V\rangle = \langle K\rangle\frac{\Delta\rho}{\rho\rho'}\frac{Dp_0}{2}.$$

The results of the corresponding processing are given in Fig. 2. The upper panel shows the dependence of the average growth rate on supersaturation, as constructed by combining the measurement results obtained in [7] and in this work. One can see that the growth rate reaches its saturation value of ~3.5 m/s above ~8 mbar. The lower panel presents the temperature dependences of the average growth rate for two supersaturations, as obtained by the optical methods and derived from the pressure decay rate during the growth. Within the measurement accuracy, the rate becomes constant below 0.35 K and equal to 3–3.5 m/s for both saturations. The absence of a sharp temperature dependence of the growth rate, typical of atomically rough surfaces [9] and facets in the normal state [10], is noteworthy. The maximal growth rate is an order of magnitude lower than the critical rate in superfluid helium (46 m/s at 25 atm [11]). Note that the velocities of helium flowing to the crystal are even one order of magnitude lower (~0.3 m/s). Thus, the maximal surface growth rate bear no relation to the critical rates in liquid helium.

The spiral growth model, developed in [6], makes allowance for the associated mass, renormalization of linear energy of the moving step, localization of step kinks at high supersaturations, and the Cherenkov phonon radiation. For the step mobility caused at high supersaturations by the localization of bends, the theory [6] predicts that the facet growth rate will tend to a constant. The supersaturation Dp_{sat} is estimated as (parameters are given in the CGS system of units)

$$Dp_{sat} \approx \frac{\rho}{\Delta\rho}\frac{1}{a\sqrt{\eta\mu_0}}, \quad \eta = (430\text{–}960),$$

$$\mu_0 \sim 3\times 10^7\frac{1}{T^3},$$

and the limiting spiral growth rate is

$$V_{max} = \frac{\Lambda}{2\pi(\beta/a)\eta}, \quad \frac{\beta}{a} = 0.011,$$

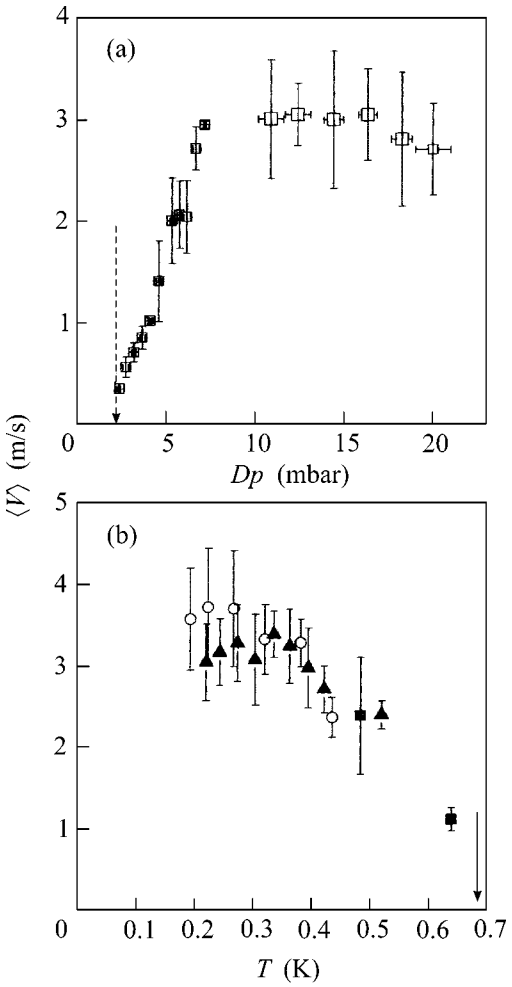

Fig. 2. (a) Dependence of the average growth rate on the supersaturation at $T = 0.45$ K. Arrow indicates the threshold supersaturation at this temperature. (b) Temperature dependence of rates for two fixed supersaturations of (triangles and squares) 6.5 and (circles) 20 mbar. Squares are for the optical method of determining the growth rate, and circles and triangles are for the determination from pressure oscillations. Arrow indicates the transition temperature for $Dp_0 = 6.5$ mbar.

where a is the lattice parameter. Numerical estimates show (parameters are taken from [6]) that, at 0.45 K, the rate in this model becomes constant at ~0.8 mbar, while the maximal facet velocity is ~0.01 cm/s. These values are substantially smaller than those experimentally observed in this work, so that the spiral growth is not responsible for the facet growth rate above 8 mbar.

Measurements of the helium crystal-surface growth for supersaturations of 0.15–0.4 bar and temperatures of 0.1, 0.6, and 0.85 K were carried out by Graf and Maris in [12] using the supersonic method. Unfortunately, our data cannot be directly compared with the results of that work for a number of reasons. Measurements in [12] were made at the atomically rough surfaces rather than at facets, as in our case, while their minimal supersaturation was an order of magnitude

higher than our maximal value. It should also be noted that the surface growth rates in [12] achieved 5–10 m/s, and the growth kinetic coefficients at large amplitudes lay in the range 2–20 s/m; i.e., they are comparable to our values.

The main result of this work is that two qualitatively close phenomena are combined together, and the requirements for the physical mechanism explaining the anomalously fast crystal growth are formulated. Nevertheless, the mechanism of efficient deceleration of crystal facets upon achieving growing rates of ~4 m/s still remains to be understood.

I am grateful to A.Ya. Parshin for discussion of results. This work was supported by the Russian Foundation for Basic Research, project no. 02-02-16772.

REFERENCES

1. V. L. Tsymbalenko, Phys. Lett. A **211**, 177 (1996).
2. V. L. Tsymbalenko, J. Low Temp. Phys. **121**, 53 (2000).
3. S. Balibar, F. Gallet, and P. E. Wolf, Phys. Rev. Lett. **51**, 1366 (1983).
4. V. L. Tsymbalenko, Phys. Lett. A **248**, 267 (1998).
5. V. L. Tsymbalenko, Phys. Lett. A **257**, 209 (1999).
6. A. V. Babkin, P. J. Hakonen, A. Ya. Parshin, *et al.*, J. Low Temp. Phys. **112**, 117 (1998).
7. V. L. Tsymbalenko, Zh. Éksp. Teor. Fiz. **119**, 1182 (2001) [JETP **92**, 1024 (2001)].
8. V. L. Tsymbalenko, Phys. Lett. A **274**, 223 (2000).
9. K. O. Keshishev, A. Ya. Parshin, and A. V. Babkin, Zh. Éksp. Teor. Fiz. **80**, 716 (1981) [Sov. Phys. JETP **53**, 362 (1981)].
10. S. Balibar, F. Gallet, P. Nozieres, *et al.*, J. Phys. (Paris) **46**, 1987 (1985).
11. O. W. Dietrich, E. H. Graf, C. H. Huang, and L. Passel, Phys. Rev. A **5**, 1377 (1972).
12. M. J. Graf and H. J. Maris, Phys. Rev. B **35**, 3142 (1987).

Translated by V. Sakun

JETP Letters, Vol. 77, No. 5, 2003, pp. 247–250. Translated from Pis'ma v Zhurnal Éksperimental'noĭ i Teoreticheskoĭ Fiziki, Vol. 77, No. 5, 2003, pp. 292–295.

Fractional Quantum Hall Effect, Jain's Rule, and Topological Textures

S. V. Iordanski

Landau Institute for Theoretical Physics, Russian Academy of Sciences, Moscow, 117334 Russia

Received February 6, 2003

It is demonstrated that Jain's rule for determining fractions in the quantum Hall effect can be obtained without recourse to the phenomenological concept of composite fermions. The possibility of existence is considered for topologically nontrivial many-electron wave functions, whose group classification gives an indication of special values of electron density in the ground states separated by a gap from excited energies. © *2003 MAIK "Nauka/Interperiodica".*

PACS numbers: 73.43.Cd

Despite the fact that more than twenty years have elapsed since the experimental discovery of the quantum Hall effect (QHE), the theory of this phenomenon is far from being complete (see reviews [1, 2]). This is primarily true for the fractional quantum Hall effect (FQHE), which necessitates the electron–electron interaction and can by no means be explained by the one-particle theory, in contrast to the integer QHE. The most successful variational many-electron wave function for explaining the 1/3 fraction was constructed by Laughlin [3, 4]. In those works, the approximation of extremely high magnetic field was used, in which one can restrict oneself to the states of the lowest Landau level. However, this does not conform to the experimental situation, where the cyclotron energy is on the order of the mean energy of electron–electron interaction. Moreover, this approach encounters difficulties in generalizing to the other fractions. Computer simulations give a rather crude approximation for the realistic multiparticle functions, because the number of particles in the corresponding calculations on modern computers does not exceed several tens.

The most successful phenomenological description is given by Jain's model of "composite" fermions [5, 6], which predicts the majority of observed fractions. According to this model, electrons are dressed with magnetic-flux quanta, whose magnetic field is concentrated in an infinitely narrow region around each electron. It is assumed that the even number of flux quanta provides the Fermi character for these particles. The inclusion of this additional magnetic field in the formalized theory leads to the so-called Chern–Simons Hamiltonian. This approach is described in detail in [7]. However, practical calculations use the mean-field approximation, in which the effective magnetic field is assumed to be equal to the sum of an external magnetic field and an additional constant magnetic field that provides the total number of additional magnetic-flux quanta for all composite electrons. It is just this fact that leads to Jain's rule for fractional electron densities $\rho_e = (H/\phi_0)(l/(1 + 2l))$ corresponding to the complete filling of Landau levels in the effective magnetic field, when it is assumed that there are (–2) flux quanta ϕ_0 per composite electron, if the external-field flux is taken to be positive and l is a positive integer. According to this model, one can assert that, as $l \longrightarrow \infty$ and $\rho_e \longrightarrow H/2\phi_0$, the effective magnetic field turns to zero and the composite fermions should behave as an ordinary 2D Fermi liquid in the absence of magnetic field. This statement qualitatively explains the experimentally observed phenomena for the half-filled Landau level. Attempts at extending the calculations beyond the mean-field approximation for the Chern–Simons Hamiltonian revealed numerous intrinsic difficulties of this theory and did not aid in calculating the assumed Fermi liquid parameters for half-filled Landau levels. A review of works on this subject can be found in the B. Halperin's article published in [2].

The introduction of an infinitely narrow region around each electron, which, nevertheless, provides a finite flux for the internal magnetic field, seems to be quite artificial. When accepted on the microscopic level, this electron property cardinally changes our notion of the electron and, in fact, bears no relation to two-dimensionality or to the presence of an external magnetic field.

However, the theory of FQHE can likely be developed on a different physical basis that is associated with the existence of topological textures stable to nonzero deformations. The topological classification of multiparticle wave functions is a rather complicated mathematical problem, and, to my knowledge, no simple and, simultaneously, effective definition of topological classes is presently known. The classification of topological excitations is well elaborated for a ferromagnetic 2D electron gas in a strong magnetic field with

filling $\nu = 1$ (skyrmions [8, 9]). When developing the theory, one can apply the canonical transformation to electron spinors $\psi(\mathbf{r})$ at each point by introducing new spinors $\chi(\mathbf{r})$, according to the equation

$$\psi(\mathbf{r}) = U(\mathbf{r})\chi(\mathbf{r}), \quad \psi^+(\mathbf{r}) = \chi^+ U^+(\mathbf{r}), \tag{1}$$

where U is the rotation matrix depending on the three Euler angles; e.g., $U = U_z(\alpha)U_y(\beta)U_z(\gamma)$ (indices denote the rotation angles). After the canonical transformation, the Lagrangian of interacting electrons takes the form (in the system of units where $l_H = 1$, $H = 1$, and $\hbar = 1/2$)

$$L = \int\left\{ i\chi^+\frac{\partial\chi}{\partial t} - \frac{1}{2m}\chi^+(-i\nabla + \mathbf{A}_0 + \hat{\Omega})^2\chi\right\}d^2r + \frac{1}{2}\int V(\mathbf{r}-\mathbf{r}')\chi^+(\mathbf{r})\chi^+(\mathbf{r}')\chi(\mathbf{r}')\chi(\mathbf{r})d^2r d^2r', \tag{2}$$

where

$$\hat{\Omega} = -i\hat{U}^+\nabla U = \mathbf{\Omega}^l\sigma_l,$$

σ_l are Pauli matrices,

$$\Omega^z = \frac{1}{2}(1+\cos\beta)\nabla\alpha,$$

$$\mathbf{\Omega}^x = \frac{1}{2}(\sin\beta\cos\alpha\nabla\alpha - \sin\alpha\nabla\beta),$$

$$\mathbf{\Omega}^y = \frac{1}{2}(\sin\beta\sin\alpha\nabla\alpha + \cos\alpha\nabla\beta),$$

and $V(\mathbf{r}-\mathbf{r}')$ is the Coulomb interaction. It is assumed that $\gamma = \alpha$, because the angle γ plays an auxiliary role, although it eliminates singularities of the matrix U. The spinors ψ and ψ^+ are the electron-field operators obeying the Fermi commutation rules. One can readily verify that χ^+ and χ satisfy the same commutation rules. The new Lagrangian is formally equivalent to the initial one with $\Omega \equiv 0$. Hence, this Lagrangian gives electronic states corresponding to $\Omega \equiv 0$, because one can always perform the inverse transformation. However, one may attempt to seek any other states that are characteristic of the Lagrangian with $\Omega \neq 0$. This program can be successfully implemented in the case where U changes only slightly at a distance on the order of the magnetic length $l_H^2 = \frac{eH}{\hbar c}$ (H is the external magnetic field) and all $\mathbf{\Omega}^l$ are small. At large distances, $\beta = 0$, so that the matrix U only rotates spinors about the z axis, which aligns with the spin orientation in a homogeneous ferromagnet and endows them with a nontrivial phase. The desired electronic state with operators χ and χ^+ can be obtained perturbatively for small Ω from a uniform ferromagnetic state of operators χ. The existence of a topological number

$$K = \frac{1}{2\pi}\int \mathrm{curl}\,\mathbf{\Omega}^z d^2r,$$

which is determined by the vortical number of revolutions through the angle $\alpha(\mathbf{r})$ upon going around an infinite contour, is a nontrivial topological requirement. This circumstance ($K \neq 0$) is precisely that which defines the wave-function topological class and renders wave-function deformation into the trivial ferromagnetic state with identical directions of all ψ spinors impossible. Thus, $\hat{\Omega}$ with different K characterize topologically different classes of multiparticle wave functions. The condition $\beta = \pi$ at the point of $\alpha(\mathbf{r})$ singularity (of the polar-angle type) guarantees the absence of singularities for $\hat{\Omega}$. This approach was suggested in [10]; various physical quantities were calculated in [11, 12] in the leading order of perturbation theory. The results coincided with those obtained by other methods (see [7, 8]). The quantity curl $\mathbf{\Omega}^z$ plays the role of an additional effective magnetic field, this field being the collective property of the multiparticle wave function rather than the attribute of an individual electron. The calculations of electron density, energy, and spin density can, in principle, be carried out up to any order in the gradient of matrix U.

This example demonstrates the method of determining isolated topological excitations. However, this approach can be extended to the analysis of the texture and a multiparticle wave function corresponding to the finite density of in-plane topological number K. The analysis of arbitrary textures of this type for $\hat{\Omega}$ involves great methodological difficulties and, likely, bears no direct relation to the ground-state classification. We therefore assume that these textures are near-periodic, so that the mean-spin field is periodic. Let us consider a unit cell. We assume that the mean-spin vector at the unit-cell boundary has a constant value and is aligned with the z axis in the spin space. Thus, the angle β is assumed to be a periodic function in plane, with $\beta = 0$ at the unit-cell boundaries. The angle α is assumed to possess vortex singularity at some point inside each unit cell, for which we assume that $\beta = \pi$ in order to eliminate the singularities of $\hat{\Omega}(r)$. One can set, for example, $\alpha = \sum\alpha_i(r)$, where the summation goes over all unit cells and $\alpha_i(r)$ is the polar angle centered inside the ith unit cell. Therefore, each cell is characterized by the same topological number

$$K = \frac{1}{2\pi}\int_\sigma \mathrm{curl}\,\Omega^z d^2r,$$

which specifies the integer number of quanta for the additional effective magnetic field with the average value $H_{\text{eff}} = \frac{K}{\sigma}$ over the sample area, where σ is the unit-cell area. Taking ferromagnetic χ and χ^+ as the main approximation, the average spin $\mathbf{n}(r)$ will give the K-fold mapping onto the direction sphere for any unit cell. Although the sum $\alpha = \sum \alpha_i$ over all cells is, formally, a periodic function, it diverges. Since only $\sin\alpha$ and $\cos\alpha$ enter the expression for $\hat{\Omega}$, the modulo 2π convergence is sufficient. I will assume, without proof, that either this convergence holds or $\Omega^{x,y}$ can be regularized in a periodic manner.

The suggested construction of finite-energy vortices without core singularity (regular $\mathbf{\Omega}^l$) is not unique. For example, in the absence of free spins (large g factor), one can consider two size-quantization levels (for motion perpendicular to the 2D plane) and introduce the corresponding isospin, after which an analogous construction, though with different constants, can be obtained for the isospin.

It is not my intention to calculate electron energy in such textures. This is a rather complicated problem for unit-cell sizes on the order of magnetic length, for which the gradient expansion in Ω is impossible. My goal is to classify the electronic states with the aim of determining certain special density values that correspond to the ground states separated by a gap from the excited states. The problem of numerical calculation of the gap can be posed after the classification of ground states.

We have, in fact, a system of interacting electrons in a periodic effective magnetic field (the sum of the external magnetic field and a periodic vortex magnetic field in unit cells) with nonzero mean. The corresponding transformation group consists of the magnetic translations and is the projective representation of the conventional translation group. According to the well-known analysis (Brown, Zak; see, e.g., [13]) for noninteracting electrons, the band spectrum is regular only for a rational number of flux quanta. The irrational number of quanta or a rational number $\frac{p}{q}\phi_0$ with large noncancelable numerator and denominator brings about a highly irregular structure with the allowed and forbidden bands thickened in a certain energy region. One can assume, in the spirit of the Fermi liquid theory, that the interaction does not affect these spectral features. Restricting oneself to the simplest fractions, for which the effective-field flux through the unit cell is $(H\sigma + K\phi_0) = \phi_0/l$, where l is an integer, one obtains $\sigma = (1 - Kl)\phi_0/lH$ for the unit-cell area.

The total number of states per unit area, with one electron per unit cell, determines the electron density $\rho = Hl/\phi_0(l - Kl)$ and must correspond to the filled set of bands obtained from S/σ states in the absence of magnetic field, though in a periodic potential with the period specified by the unit cell. Here, S is the sample area. Simple analysis suggests [13] that this initial band is split into l subbands, each being (odd l) l-fold or (even l) $l/2$-fold degenerate, and with the fraction of the number of states in each subband being (odd l) $1/l^2$ or (even l) $2/l^2$. However, the total number of states in all subbands is S/σ. One can assume that, even in the presence of interaction, these states are separated from the higher energy states by the greatest gap. The structure of inner forbidden bands is irrelevant, because all lower-lying states are filled. Note that the evenness of the K number is immaterial, because, in contrast to the composite-fermion model, the Fermi commutation rules for the operators χ and χ^+ are fulfilled automatically and have no relation to the topological number K. The occurrence of any specific numbers of vortex-field flux quanta is dictated by the ground-state energy. Assuming that $K = -2$ is energetically most favorable and corresponds to the largest gaps, one arrives at Jain's rule $\rho = Hl/\phi_0(1 + 2l)$, with the Landau level half-filling $\rho = H/2\phi_0$ in an external field corresponding to vanishingly small effective magnetic field (zero number of flux quanta per unit cell).

Thus, I have reproduced the key statement of the theory of composite fermions. Of course, these results are quite crude and, to some extent, hypothetical. The energy gap, the properties of elementary charge excitations, and the conductivity calculations, as well as the analysis of different K and l values, are still open questions, and the approach to these problems is as yet unclear. However, the fact that these results are obtained within the standard physical approach, without invoking the cardinal hypotheses about electron properties, is quite intriguing.

I am grateful to V.G. Dolgopolov, V.F. Gantmakher, V.B. Timofeev, and M.V. Feĭgel'man for helpful discussions. This work was supported by the Russian Foundation for Basic Research (project no. 01-02-17520), the Program for Supporting Scientific Schools, and State Contract 40.020.1.1.1165 of the Ministry of Science of the Russian Federation.

REFERENCES

1. *The Quantum Hall Effect*, Ed. by R. Prange and S. M. Girvin (Springer, New York, 1987; Mir, Moscow, 1989).
2. *New Perspectives in Quantum Hall Effects*, Ed. by S. Das Sarma and A. Pinozuk (Wiley, 1997).
3. R. B. Laughlin, Phys. Rev. B **23**, 5632 (1981).
4. R. B. Laughlin, Phys. Rev. Lett. **50**, 1395 (1983).
5. J. K. Jain, Phys. Rev. Lett. **63**, 199 (1989).

6. J. K. Jain, Phys. Rev. B **41**, 7653 (1990).
7. B. I. Halperin, P. A. Lee, and N. Read, Phys. Rev. B **47**, 7312 (1993).
8. S. Sondhi, A. Kahlrede, S. Kivelson, and E. Rezayi, Phys. Rev. B **47**, 16419 (1993).
9. K. Moon, N. Mori, Kun Yung, *et al.*, Phys. Rev. B **51**, 5138 (1995).
10. S. V. Iordanskiĭ and S. G. Plyasunov, Pis'ma Zh. Éksp. Teor. Fiz. **65**, 248 (1997) [JETP Lett. **65**, 259 (1997)].
11. S. V. Iordanskiĭ, S. G. Plyasunov, and I. V. Fal'ko, Zh. Éksp. Teor. Fiz. **115**, 716 (1999) [JETP **88**, 392 (1999)].
12. S. V. Iordanskiĭ and A. B. Kashuba, cond-mat/0211214; Phys. Rev. B (2003) (in press).
13. E. M. Lifshitz and L. P. Pitaevskiĭ, *Course of Theoretical Physics*, Vol. 5: *Statistical Physics* (Nauka, Moscow, 1978; Pergamon, New York, 1980), Part 2.

Translated by V. Sakun